Efficient Acquisition and Reconstruction for Magnetic Resonance Spectroscopic Imaging

by

Wenting Deng

A dissertation submitted to the Graduate Faculty of
Auburn University
in partial fulfillment of the
requirements for the Degree of
Doctor of Philosophy

Auburn, Alabama
May 5th 2013

Keywords: Magnetic Resonance Spectroscopic Imaging, Sequential Data Selection, Nonlinear Reconstruction

Approved by

Stanley Reeves, Chair, Professor of Electrical and Computer Engineering
Thomas Denney, Professor of Electrical and Computer Engineering
Bogdan Wilamowski, Professor of Electrical and Computer Engineering

Abstract

Magnetic resonance spectroscopic imaging (MRSI), combining both magnetic resonance spectroscopy (MRS) and magnetic resonance imaging (MRI) techniques, has proven to be a powerful approach to reveal information about metabolite distributions and discriminate multiple resonant frequencies in the spectrum. Due to its nondestructive nature and sensitivity to the molecular environment of individual atoms [1], MRSI is widely applied in the clinical community. The typical applications include mapping abnormal tissues in the brain [2, 3, 4], in the prostate [3, 5], in the breast [6, 7], as well as pathologic analysis after resection operations [8]. All of these clinical studies require satisfactory resolution in both spatial and spectral dimensions, which in conventional MRSI demands a great deal of acquisition time. Unfortunately, patient discomfort, motion artifacts and cost will significantly increase when the acquisition time lengthens. To overcome these problems, we propose to implement an imaging protocol that only acquires an optimal subset of data to accelerate the collection process without sacrificing spatial and spectral accuracy in reconstruction.

In most MRSI applications, the spectral domain has great sparsity, which raises the possibility of reconstructing spectral information with limited time series data [9]. Therefore, an efficient sequential backward selection (SBS) [10] technique is proposed to select a limited set of but the most informative echo-time values, which are then applied to echo-planar imaging (EPI) acquisition [11]. By exploiting multi-echo EPI, multiple k-space frames can be acquired within one excitation to further reduce the acquisition time. To achieve this purpose, we modify the selection method to a more efficient approach. Instead of selecting echo-time value one by one, the modified algorithm selects multiple echo-time values simultaneously, which would then be used in one excitation acquisition.

For the EPI technique, a k-space frame cannot be collected instantly. In other words, every k-space sample will have a different time delay even in the same k-space frame. Consequently, selecting one echo-time value for a whole k-space frame might not be accurate enough. We then extend the data selection method to both k-space and time domains. In addition, an advanced EPI strategy is introduced. On the other hand, if SBS algorithm is the only restriction for k-t data selection, the acquisition efficiency might be reduced, which leads to longer observation procedure. Considering this, sequential k-t selection with constraint will be studied for a better selection result in a more efficient way.

Due to the selection method and the EPI acquisition technique, the collected data are normally nonuniform and time varying. Therefore, fast Fourier Transforms (FFTs) are not capable reconstructing the spatial and spectral information directly. Besides, an FFT cannot separate spatial information of different metabolite resonances. On the other side, conventional optimization methods [12], such as conjugate gradients (CG), require very high computational effort and large memory storage to find the matching parameters of the images. A fast reconstruction method combining polynomial approximation with FFTs is investigated, which can greatly accelerate the reconstruction process without sacrificing reconstruction quality.

During the reconstruction procedure, the finite data set raises a practical problem: frequency local minima, which means convergence to the global minimum is not guaranteed. In order to overcome this problem, we study the origin of the local minima, and propose an easily implemented method: varying estimated decays during the optimization. However, this method has its own limitations, especially in reconstruction efficiency and accuracy. Therefore, another advanced technique, applying weighted scalars to the cost function model, is presented. The results show that the second method can efficiently attenuate frequency local minima effect, while avoiding the reconstruction speed and accuracy problems.

Acknowledgments

It has been a great pleasure to be a Ph.D student working closely with Dr. Stanley J. Reeves. I would like to give my heartfelt thanks for his guidance and encouragement over the years. He led me into the medical imaging world and supported me throughout my research process with his patience and knowledge. This work would never have existed without him.

I would like to thank my advisory committee members, Dr. Thomas Denney and Dr. Bogdan Wilamowski for their generous comments and suggestions on this dissertation. I also thank Dr. Tin-Yau Tam for serving as the outsider reader.

I would like to thank Dr. Donald B. Twieg from the University of Alabama at Birmingham, Dr. Nouha Salibi from Seimens for their kindness help of subjects preparation and data acquisition.

In addition, my appreciation goes to all the previous and present group members and collaborators, especially Weidong Tang, Tao Ma, Kevin Perry, Chun G. Shiros, Wei Zha, Bharath Ambale Venkatesh and Ningzhi Li, for their help and friendship throughout the course of this research.

Finally, I want to thank my beloved family for their unconditional support to me in every possible way. Their trust and confidence in me is my forward power. My wonderful husband, Dayu Yang, makes me become a better person. Without his endless love, care and patience, I would not be who I am now. My beloved parents, Yucheng Deng and Lizhong Yang, give their hearts to me. They do everything good for me and everything they can to support me in every step in my life. I would like to dedicate this dissertation to my dearest family.

Table of Contents

List of Figures

List of Tables

Chapter 1

Introduction

Magnetic resonance spectroscopic imaging, which is a combination of magnetic resonance spectroscopy (MRS) and magnetic resonance imaging (MRI), is an important application of the phenomenon of nuclear magnetic resonance (NMR). It can produce metabolite distributions and spatially localized spectra inside subjects. Because of its relative safety, MRSI is widely used to diagnose health conditions of human and animals. ^{1}H, ^{13}C, ^{31}P MRSI studies have many applications in clinical practice. They can indicate information about cellular activities in a variety of diseases including brain tumors [2], breast tumors [6], prostate tumors [5], epilepsy [13], as well as abnormalities in various pathologies [14, 15].

Despite its attractive potential, MRSI has remained largely in the realm of health care research because long acquisition time is required in a standard acquisition scheme. Factors like patient comfort, motion artifacts and expense limit the time available to obtain good image resolutions in MRSI. To accelerate the data acquisition and keep the quality of the reconstructed image, we are pursuing strategies where the imaging procedure is optimized so that only an optimal subset of data is collected and used for reconstruction. On the other hand, these acquired data are normally laid out nonuniformly. Fast reconstruction methods, like the Fourier transform, are not applicable anymore. Therefore, we propose to develop a new optimization method to find the best matching parameters of the images.

1.1 Organization of the Proposal

In this chapter, we briefly review the physics of nuclear magnetic resonance and basic principles of magnetic resonance spectroscopic imaging.

In Chapter 2, a new efficient acquisition technique is presented. We propose a sequential selection method to choose limited but optimal echo-time values which are then used in echo-planar imaging acquisition. ^1H phantom experiments demonstrate that our approach achieves similar results to standard MRSI while using much less acquired data.

In Chapter 3, we address limitations of echo-time selection in data acquisition. We propose two alternative data selection strategies: one is k-t selection, which extends the sequential selection technique in both k-space and time domains; another one is overlapped echo-time selection, which makes the acquisition time for each k-space frame shorter and may lead to a fast reconstruction process.

In Chapter 4, we summarize the standard reconstruction method used for MRSI. Then a new iterative reconstruction method based on a polynomial model is detailed discussed. This technique decomposes the exponential time function and utilizes fast Fourier transform to speed up the optimization procedure.

In Chapter 5, a practical problem of parameter fitting in reconstruction is described: local minima. Two methods, varying estimated decays / applying weighted scalars to the cost function model during the optimization, are prsented to solve the local minima problem. Experiments and comparisons indicate their efficiency and simplicity of implementation.

Finally, conclusions are given in Chapter 6. The innovative ideas are summarized, and possible future work is discussed.

1.2 Physical Bases of Nuclear Magnetic Resonance

Nuclear magnetic resonance (NMR) is a phenomenon when the nuclei [16] of certain atoms are immersed in a magnetic field, absorbing and re-emitting electromagnetic (EM) energy. This energy owns a specific resonant frequency that depends on the strength of the external magnetic field and the chemical environment of the nuclei. Many scientific techniques exploit NMR phenomena to probe molecule structures as well as detailed internal forms of the observed subjects.

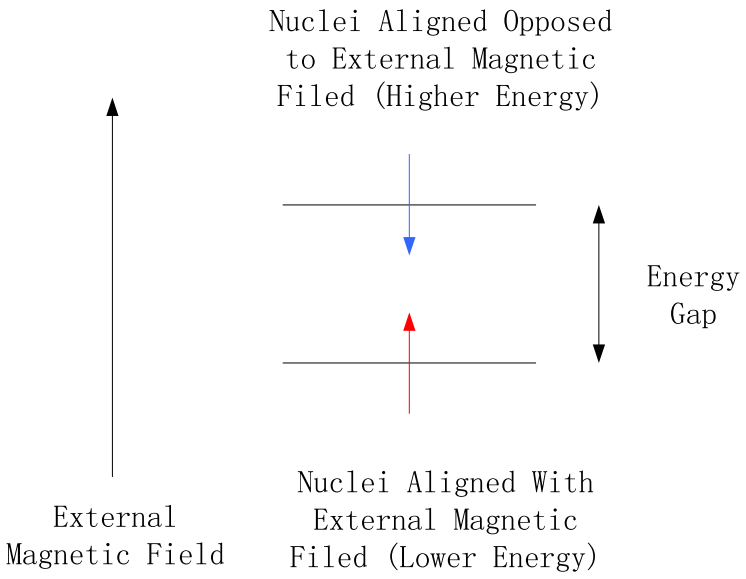

Figure 1.1: Stationary states of nuclear spins in a static magnetic field

In the absence of an external magnetic field, the nuclei have random orientations. The vector sum of these orientations will be zero. When an external magnetic field is applied, randomly oriented nuclei experience an external force that aligns the nuclei either in a parallel or an anti-parallel direction in reference to the applied magnetic field. The lower-energy state with the nuclei aligned with the field is called the α-spin state; the higher-energy state with the nuclei aligned against the field is called the β-spin state. This situation is depicted in Figure 1.1. In fact, the energy difference between two states is proportional to the strength of the external magnetic field.

$$\Delta E = \frac{rh}{2\pi} \times B_0 \tag{1.1}$$

where ΔE is the energy difference between α and β states; h is Planck's constant; B_0 is the strength of the external magnetic field and r is the gyromagnetic ratio ($26.753 sec^{-1} Gauss^{-1}$for a proton). Due to Boltzmann's law, the lower-energy state always has a larger population of

spins than the higher-energy state. However, when a nucleus is irradiated with an extra EM radiation with energy $\Delta E = rhB_0/2\pi$, the nucleus can flip from the lower-energy state to the higher-energy state. This energy is usually supplied by application of an rf pulse signal to the system. After the rf signal, the excited nuclei tend to return to their low-energy state by emitting a well-defined resonant frequency (the same frequency as the applied rf). This emission of rf signals is then detected by rf coils placed close to the excited object. This is the origin of NMR and the emitted signal is called a free induction decay (FID). Besides (1.1), nuclear energy can also be represented as

$$E = hv \tag{1.2}$$

where h is Planck's constant and v is the frequency of the EM wave. When (1.1) combines with (1.2)

$$\Delta E = \frac{rh}{2\pi} \times B_0 = hv \tag{1.3}$$

The resonant frequency v is proportional to the applied field B_0

$$v = \frac{r}{2\pi} \times B_0 = \frac{26,753 sec^{-1} Gauss^{-1}}{2\pi} \times B_0 = 4257.8 sec^{-1} Gauss^{-1} \times B_0 \tag{1.4}$$

For the fields of currently available magnets, the resonant frequencies occur in the radio-frequency range of the spectrum. Because hydrogen is a major component of organic compounds and historically NMR was first used to study protons, we limit our discussion of NMR to proton magnetic resonance.

1.2.1 Chemical Shift

In nature, protons do not exist independently. Instead, they are surrounded by electrons. In the presence of an external magnetic field, the electrons will partially shield the proton

from the external field. Their negative charges generate an opposite magnetic field to the externally applied field. As a result, the actual field strength is weaker than the external field strength. This is known as chemical shielding.

$$B_{actual} = B_{external} - B_{shielding} \tag{1.5}$$

$$v_{actual} = 4257.8 sec^{-1} Gauss^{-1} \times B_{actual} \tag{1.6}$$

In different molecular environments, protons are shielded by different amounts of electrons. Therefore, the resonant frequencies of individual protons vary with the chemical surroundings. For example, in methanol, the hydroxyl proton is not shielded as much as the methyl proton, so the actual field strength applied to the hydroxyl proton is stronger. Consequently the hydroxyl proton has a higher resonant frequency than the methyl proton.

Generally speaking, chemical shielding is very small compared to the external field. Therefore, it is not accurate enough to utilize absolute differences of resonant frequencies to distinguish individual protons. A more reasonable way to express resonant frequency differences is in parts per million (ppm), which defines frequency differences between a reference frequency and the observed resonant frequency relative to a reference frequency.

$$\delta = \frac{(v_{signal} - v_{ref}) \times 10^6}{v_{ref}} \tag{1.7}$$

The relative frequency differences expressed in (1.7) are known as chemical shifts. For a given proton, the chemical shift in ppm is the same regardless of the external field, which makes the chemical shift values easier to interpret.

1.2.2 NMR Signals

As we mentioned above, different chemical environments lead to different chemical shielding of protons. Thus, the number of NMR signals of a molecule corresponds to the number of different types of protons present in the molecule. For instance, ethanol, as shown

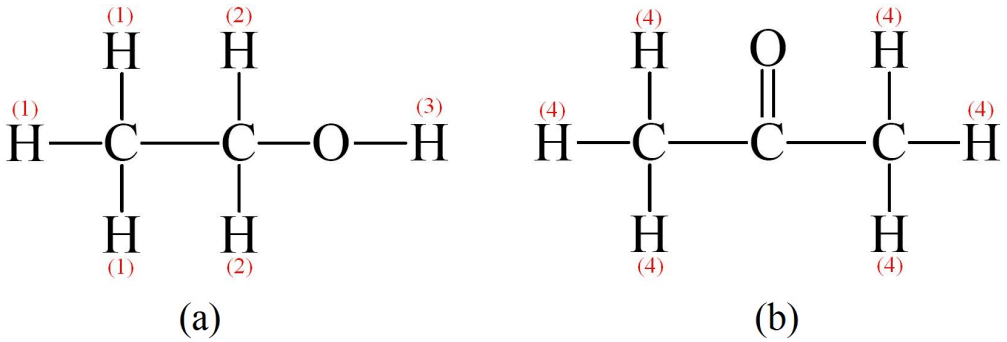

Figure 1.2: Molecular structure of (a) ethanol (b) acetone

in Figure 1.2a, has one methyl group (1), one ethyl group (2) and one hydroxyl group (3). The protons from different groups have their own chemical shifts. Consequently, three NMR signals can be observed from ethanol. Acetone, as shown in Figure 1.2b, for another instance, has two identical methyl groups (4), where all protons from these two groups have the same chemical shift and are said to be chemically equivalent.

In practice, however, there may be fewer signals in the NMR spectrum than the number of types of protons in a molecule, especially a large molecule. The reason is that large molecules may have similar functional groups, which lead to similar resonant frequencies. Association of chemical shifts with different types of protons must be done carefully.

Unlike the number of resonant peaks, the strength of resonant peaks represented by the area under each peak is only determined by the number of protons contributing to that peak. For example, butanone, as shown in Figure 1.3, has two different methyl groups (1)(3). These two groups create two NMR peaks with different resonant frequencies; but these two signals have the same area under the peaks. One thing we need to mention here: the number of protons is only proportional to the area under the peak, not the peak height. Therefore, when we reconstruct the magnitudes of resonances, the number of protons cannot be used for accurate proportional estimation of magnitudes, may only be used for the start estimation.

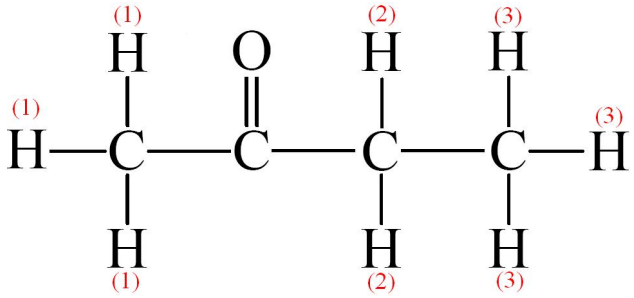

Figure 1.3: Molecular structure of butanone

1.3 MRSI Basics

MR imaging and MR spectroscopy are two important applications of NMR, which make use of the property of NMR to get spatial and spectral information inside the subjects. The combination of these two techniques is called magnetic resonance spectroscopic imaging (MRSI).

For MR spectroscopy, spectral information is only presented at one spatial location, which makes MRS unable to visualize the detailed internal form of subjects. On the other hand, in conventional MR imaging, spatial information is non-time-varying, which makes MRI unable to separate different resonant frequencies. Thus, MRI can only map the proton distribution of water. MRSI, instead, gives results that are readily interpretable. At a given resonant frequency, there is a detailed spatial map; while at a given spatial location, a spectral plot is available (examples are shown in experiment section of Chapter 2). MRSI allows collection of spectroscopic data from multiple regions simultaneously.

1.3.1 Imaging Model

The basic 2-D form of MRI can be expressed as:

$$s(k_x, k_y) = \int\int \rho(x, y) \exp[-j2\pi(k_x x + k_y y)]dxdy \tag{1.8}$$

where

$$k_x = \frac{\gamma}{2\pi}\int_0^T G_x(\tau)d\tau$$
$$k_y = \frac{\gamma}{2\pi}\int_0^T G_y(\tau)d\tau$$

$G_x(\tau)$, $G_y(\tau)$ are the time-dependent field gradients along x and y axes, which are applied to the system to distinguish the spatial distribution of spins by Fourier encodings [1]. $\rho(x, y)$ represents the spatial distribution. Notice that the observed $s(k_x, k_y)$ is in effect a Fourier transform domain representation of the spatially distributed spin density of $\rho(x, y)$ at the spatial-frequency coordinate (k_x, k_y).

The difference between MRI and MR spectroscopic imaging is the inclusion of the time domain (or equivalently the spectral domain) to the spatial MR data in MRSI. Therefore, in order to extend the 2-D MRI model to 3-D MRSI model, the original spatial distribution $\rho(x, y)$ needs to include an extra time coordinate becoming a time-varing spatial distribution $\tilde{\rho}(x, y, t)$ (t is later used for spectral reconstruction). In consequence, the observations of MRSI can be expressed as

$$s(k_x, k_y, t) = \int\int \tilde{\rho}(x, y, t)\exp[-j2\pi(k_x x + k_y y)]dxdy \tag{1.9}$$

As we mentioned in our previous NMR physical section, after the extra rf signal is turned off, the spin system returns to the low-energy state with the emission of NMR signals. Two relaxation mechanisms are associated with this process: longitudinal(T_1) relaxation, which realigns the spins along the original external B_0 field direction; another called transverse or T_2 relaxtion, which is a decay process of the FID. In practice, because of magnetic field inhomogeneity, the observed FID decays even more rapidly than the inherent T_2. The effective relaxation time T_2^* is given as

$$\frac{1}{T_2^*} = \frac{1}{T_2} + \frac{\gamma\Delta B}{2} \tag{1.10}$$

where ΔB represents the field inhomogeneity [17]. Because the readout time is very short in conventional MR imaging, it is not necessary to include these relaxation effects in imaging model. However, MRSI requires relatively long readout time to get the spectroscopic information. In this case, relaxation times can not be ignored. Beacuse the FID signal is the major interest of this research work, in our study, we only consider the effect of transverse relaxation. Now the time-varing spatial distribution $\tilde{\rho}(x, y, t)$ in MRSI model can be represented as

$$\tilde{\rho}(x, y, t) = \rho(x, y) e^{-\frac{1}{T_2^*(x,y)} t} \tag{1.11}$$

Normally, in MRSI, we want to observe more than one type of proton. Since the relaxations and their respective relaxation times are quite sensitive to the chemical enviroments surrounding the nuclei, each type of proton has its own T_2^*. In addition to the decay of the FID, each type of proton has its own resonant frequency (in this research work, we treat water proton having $0Hz$ resonant frequency). Hence, for multiple resonance MRSI, (1.11) is updated as

$$\tilde{\rho}(x, y, t) = \sum_i \rho_i(x, y) e^{-\frac{1}{T_{2i}^*(x,y)} t} e^{-j\omega_i(x,y)t} \tag{1.12}$$

where i represents different resonant peaks and ω_i is the frequency offset from water peak. Now, the observed MRSI signal can be rewritten as

$$s(k_x, k_y, t) = \int\int \sum_i \rho_i(x, y) e^{-\frac{1}{T_{2i}^*(x,y)} t} e^{-j\omega_i(x,y)t} e^{-j2\pi[k_x x + k_y y]} dx dy \tag{1.13}$$

1.3.2 Echo-Planar Imaging

The standard MRSI protocol is to acquire a set of k-t samples on uniform grids and perform Fourier transforms on the acquired data to obtain the spatial distributions and the resonant spectra. A large number of coding steps are required for spectroscopic imaging,

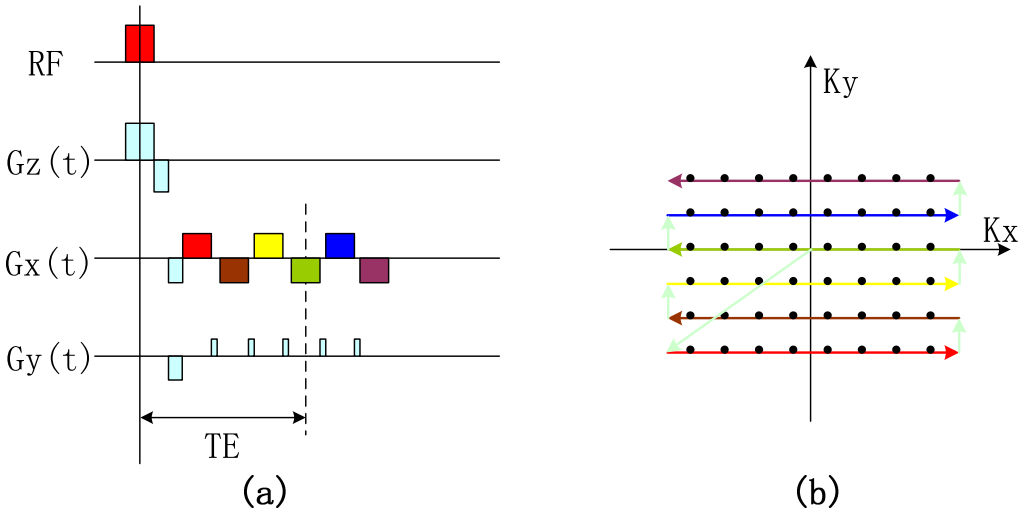

Figure 1.4: (a) EPI pulse sequence (b) EPI trajectory

and they are often too time-consuming for in-vivo imaging. Therefore, "high-speed imaging" has been introduced to the MRSI field [17]. Due to developments in gradient hardware and processing methods, an imaging technique called echo-planar imaging (EPI) has become popular in MRSI [18, 19]. In this technique, one rf excitation is followed by a series of gradient reversals, thereby collecting a complete data set of one k-space image. Figure 1.4 shows a standard EPI trajectory and pulse sequence.

Echo-planar imaging can be further divided into single-echo EPI and multi-echo EPI. In single-echo EPI, only one complete data set of a k-space image is observed in one excitation, while in multi-echo EPI, several k-space frames can be observed in one excitation, which will accelerate the imaging procedure further.

As shown in Figure 1.4a, there is an echo-time (TE) parameter defined as the time between the start of the rf pulse and the center of k-space. By changing the echo-time value, we will get a set of k-space images with different time offsets and therefore the 3-D (k_x, k_y, t) MRSI data. Figure 1.5 shows 21 k-space frames with different echo-time shifts. For instance,

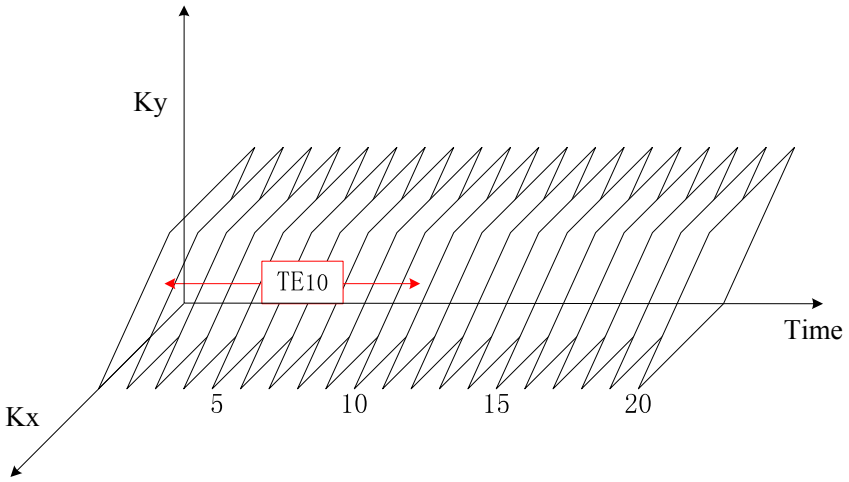

Figure 1.5: EPI images with different echo-time values

TE_{10} is the echo-time value describing the time between the start of the rf pulse and the center of 10^{th} k-space image and the observed data at TE_{10} is represented as

$$s(TE_{10}) = \int \int \tilde{\rho}(x, y, TE_{10}) \exp\{-j2\pi[k_x x + k_y y]\}\, dxdy \tag{1.14}$$

In practice, a k-space image cannot be collected instantly in EPI. In other words, k-space images acquired in EPI are evolving images, not static images as in conventional MRI methodology. Each k-space sample is time dependent, so imaging model (1.13) can be to be updated for EPI with only one varible:

$$s(t) = \int \int \tilde{\rho}(x, y, t) \exp\{-j2\pi[k_x(t)x + k_y(t)y]\}\, dxdy \tag{1.15}$$

Besides of its high speed, EPI is able to capture specified echo-time values and k-space trajectory during the acquisition process. Thus, in our study, we choose to work with variations of echo-planar imaging in MRSI acquisition.

Chapter 2

Efficient Data Acquisition with Echo-Time Selection

Long acquisition time is one of the major challenges of magnetic resonance spectroscopic imaging. Standard MRSI collects data of both k-space and time domains to obtain spatial and spectral information of subjects. In order to maintain satisfactory spatial and spectral accuracy while reducing the acquisition time, several selection techniques have been developed to choose the best possible data subset to guarantee the reconstruction quality.

Gao and Reeves [20, 21] and Plevritis and Macovski [22] investigated the optimal subset of k-space samples. The authors proposed to collect a limited number of k-space samples rather than all k-space data to reconstruct the image with a limited region of support, while keeping full data information in the time series. Conventional phase encoding imaging [17] is used in these methods, which requires one excitation to record an individual sample in k-space through the time domain. In this way, if accurate spatial details are needed, the acquisition time is still relatively long. Alternatively, within a comfortable acquisition time, only a limited number of k-space samples can be gathered for the subject, and the reconstructed images will have relatively poor spatial resolution.

In some clinical applications, especially in locating abnormal biochemistry in specific tissues, spatial details may be more useful than spectal information to indicate disease states. Therefore, other researchers emphasize the spatial distribution of key metabolites, acquiring high-resolution k-space coverage with limited chemical-shift encoding echo-time values. S. B. Reeder et al. [23] discussed optimization of echo-time spacing for maximum noise performance. However, their proposed method was only applied to a relatively small image assuming the spectral peaks are ideal at known locations; no $T2/T2*$ [17] effects are present; and each chemical metabolite only has one resonant frequency. These assumptions are not

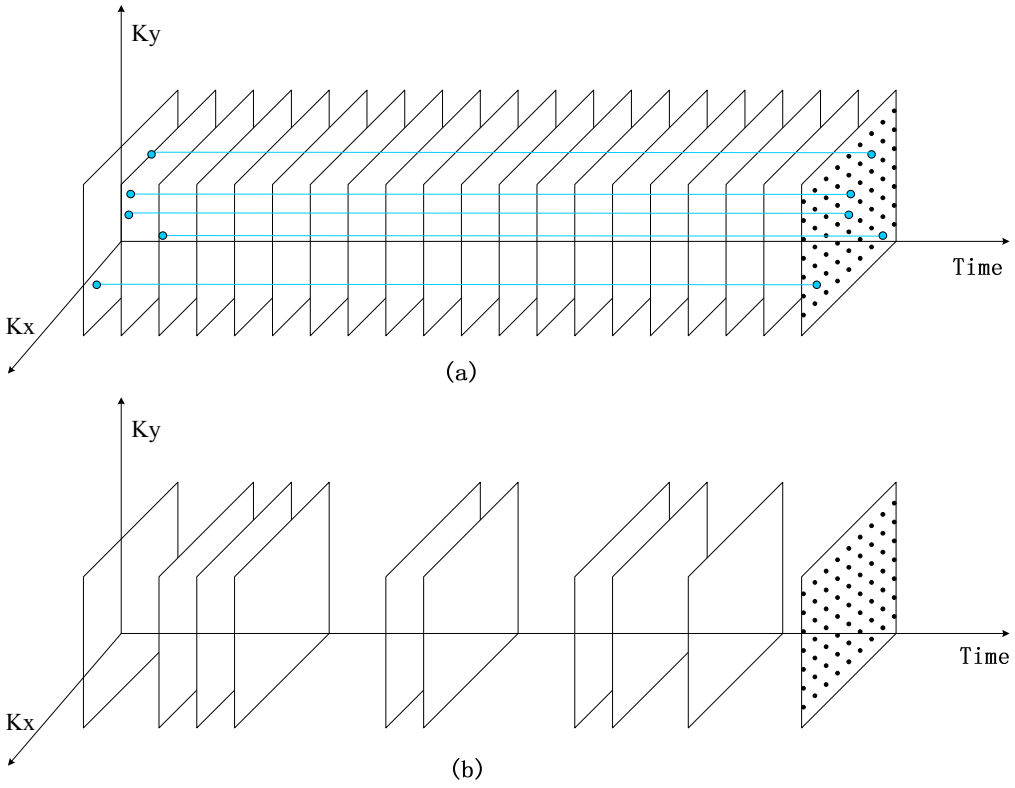

Figure 2.1: (a) k-space sample selection, (b) echo-time sample selection

always realistic for in vivo imaging. Figure 2.1 shows two types of selection methods described above: in the upper plot, data on each blue line is collected in one excitation, so the total acquisition time is proportional to the number of k-space sample locations; in the lower plot, data on each k-space is collected in one excitation, so the total acquisition time is proportional to the number of echo-time values.

In MRSI, the spectral domain normally has greater sparsity than the spatial domain. Thus, we can reconstruct spectra with limited time series data more easily than reconstructing the spatial domain with limited k-space data. In addition, as we mentioned in Chapter 1, EPI can easily capture specified echo-time values during the acquisition procedure. Therefore, in this chapter we focus on an efficient selection technique to choose the best echo-time values, which are then applied in EPI acquisition.

2.1 Echo-Time Selection Theory

2.1.1 Observation Model

To understand the method for selecting echo-time values, consider a linear observation model in matrix notation:

$$\rho = Aq + e \tag{2.1}$$

where ρ is a set of observations, q is the unknown vector of interest, A is a matrix that describes the transformation between the unknown q and the observations ρ, and e represents zero-mean white Gaussian noise. The least-squares solution of q is:

$$\hat{q} = (A^H A)^{-1} A^H \rho \tag{2.2}$$

where the superscript H represents Hermitian transpose. Since e is independently and identically distributed, the mean squared error (MSE) in the reconstruction is proportional to

$$E\left\{\|\hat{q} - q\|\right\} = \mathrm{tr}\left\{(A^H A)^{-1}\right\} \tag{2.3}$$

where tr{} means the trace of the inside matrix. This error criterion only depends on the transformation matrix A. Once we determine the A matrix, the MSE is fixed and consequently the reconstruction quality of q is determined.

For most types of MRSI, a desired time-varying image $\rho(x, y, t)$ can be described as

$$\rho(x, y, t) = \sum_{i=1}^{M} a_i(x, y) \exp\left\{[-d_i(x, y) + j\omega_i(x, y)]t\right\} \tag{2.4}$$

where M is the maximum number of metabolite resonances contained in a voxel. The complex weight a_i is proportional to the contribution from different resonances. The parameter

ω_i is the resonant frequency and d_i is the rate of damping of each resonance. After sampling, we can rewrite the basic image model at a given (x, y) location as

$$\rho(t_n) = \sum_{i=1}^{M} a_i \exp\{[-d_i + j\omega_i]t_n\} + e(t_n) \tag{2.5}$$

where $e(t_n)$ is zero-mean, independent, identically distributed Gaussian noise, and t_n is the echo time used to encode the nth EPI frame. The primary difference of (2.5) from (2.1) is that the equations are nonlinear in the parameters of interest. To utilize the error criteria shown in (2.3), we propose to linearize (2.5) and use the linearized model to develop the error criterion. Note that the linearized model is only used in the selection procedure; during reconstruction, parameters of interest are still estimated using the more accurate nonlinear model. The linearized model is given by:

$$\begin{aligned}
\rho(t_n) &= \sum_{i=1}^{M} a_{0i} \exp\left[(-d_{0i} + j\omega_{0i})t_n\right] + (a_i - a_{0i}) \exp\left[(-d_{0i} + j\omega_{0i})t_n\right] \\
&+ \left[(-d_i + j\omega_i) - (-d_{0i} + j\omega_{0i})\right] t_n a_{0i} \exp\left[(-d_{0i} + j\omega_{0i})t_n\right] + e(t_n) \\
&= \sum_{i=1}^{M} a_i \exp\left[(-d_{0i} + j\omega_{0i})t_n\right] + (-d_i + j\omega_i) t_n a_{0i} \exp\left[(-d_{0i} + j\omega_{0i})t_n\right] \\
&- (-d_{0i} + j\omega_{0i}) t_n a_{0i} \exp\left[(-d_{0i} + j\omega_{0i})t_n\right] + e(t_n) \\
&= \sum_{i=1}^{M} a_i \exp\left[(-d_{0i} + j\omega_{0i})t_n\right] + (-d_i + j\omega_i) t_n a_{0i} \exp\left[(-d_{0i} + j\omega_{0i})t_n\right] + e^*(t_n)
\end{aligned} \tag{2.6}$$

Experiments show that the the linearized model is adequate enough for the selection process (more details in Section 2.3). Here a_i, d_i, ω_i are unknown signal parameters, while a_{0i}, d_{0i}, ω_{0i} are known from prior information. Equation (2.6) can be rewritten in matrix format like (2.1) with $b_i = -d_i + j\omega_i$ and $b_{0i} = -d_{0i} + j\omega_{0i}$, as the unknown parameters $q =$

$[a_1, a_2, \ldots, a_M, b_1, b_2, \ldots, b_M]^T$. The transformation matrix is then given by

$$A = \begin{pmatrix} e^{b_{01}t_1} & \cdots & e^{b_{0M}t_1} & a_{01}t_1e^{b_{01}t_1} & \cdots & a_{0M}t_1e^{b_{0M}t_1} \\ \vdots & \vdots & \vdots & \vdots & \vdots & \vdots \\ e^{b_{01}t_n} & \cdots & e^{b_{0M}t_n} & a_{01}t_ne^{b_{01}t_n} & \cdots & a_{0M}t_ne^{b_{0M}t_n} \end{pmatrix} \tag{2.7}$$

At this point, A has only one set of variables, the choice of echo-time values t_n ($a_{0i}, d_{0i}, \omega_{0i}$ are fixed values from prior knowledge). Each row of the A matrix corresponds to a specific t_n. Hence, when we optimize the combination of rows in the A matrix, we are selecting the optimal combination of echo-time values that determines the reconstructed image quality. The MSE value is not merely a function of the number of rows removed from A. The specific choice of echo-time values is more important than the number of echo times that are selected. In some cases fewer acquired echo times may result in better reconstruction.

2.1.2 Selection Algorithm

Careful selection of the echo-time values to be applied in EPI acquisition, represented by rows of A, is required to minimize the MSE and hence optimize the reconstruction performance. Unfortunately, exhaustive search for the optimal row combination is prohibitive for a large matrix. A suboptimal sequential backward selection algorithm (SBS) is therefore used to optimize echo-time selection. We begin with all possible echo-time values and evaluate all possible choices of eliminating a single row from the current A, which corresponds to a specific echo-time value. Let r_i represent row i of A. If r_i is eliminated from A, using the Sherman-Morrison matrix inversion formula [10], the modified $(A^HA)^{-1}$ is given by:

$$(\tilde{A}^H\tilde{A})^{-1} = (A^HA)^{-1} + \frac{(A^HA)^{-1}r_i^Hr_i(A^HA)^{-1}}{1 - r_i(A^HA)^{-1}r_i^H} \tag{2.8}$$

Taking the trace of both sides and using the property that $\mathrm{tr}\{AB\} = \mathrm{tr}\{BA\}$, we can formulate an updated error criterion as

$$\mathrm{tr}\{(\tilde{A}^H\tilde{A})^{-1}\} = \mathrm{tr}\{(A^HA)^{-1}\} + \frac{r_i(A^HA)^{-2}r_i^H}{1 - r_i(A^HA)^{-1}r_i^H} \tag{2.9}$$

The first term in (2.9) is the same for every choice of an eliminated row. The error criterion will yield the smallest increase by eliminating the row that minimizes the second term of (2.9). Then the least important row will be removed and A updated to $\tilde{A}$. This process is repeated until the desired number of echo-time values remains. This approach can achieve a satisfactory selection result in an efficient manner. Moreover, SBS has other attractive advantages for echo-time selection:

- The actual values of the parameters of interest do not enter into the linear criterion. Therefore, the optimization process can be accomplished before MRSI acquisition.
- The a_{0i} values are scalars in the criterion and have only a small effect on the optimization process. Therefore, even if the prior amplitude information is not accurate, the inaccuracy will only have a small effect on the optimality of the echo-time selection.
- If the differences among resonant frequencies are fixed, a global frequency shift due to field inhomogeneity will not affect the optimality of the selected samples.

The global frequency shift we mention here is not spatially global. It means that at a given (x, y) spatial location, due to field inhomogeneity, the same frequency shift occurs for all resonant peaks. Compared to the global shifts, in general, the local variation for each resonance is small enough to ignore. Figure 2.2 shows the global shifts $\Delta\omega$ and local variations $\Delta\omega_1, \Delta\omega_2, \Delta\omega_3$ at one spatial location. At different locations, the values of global shifts can vary.

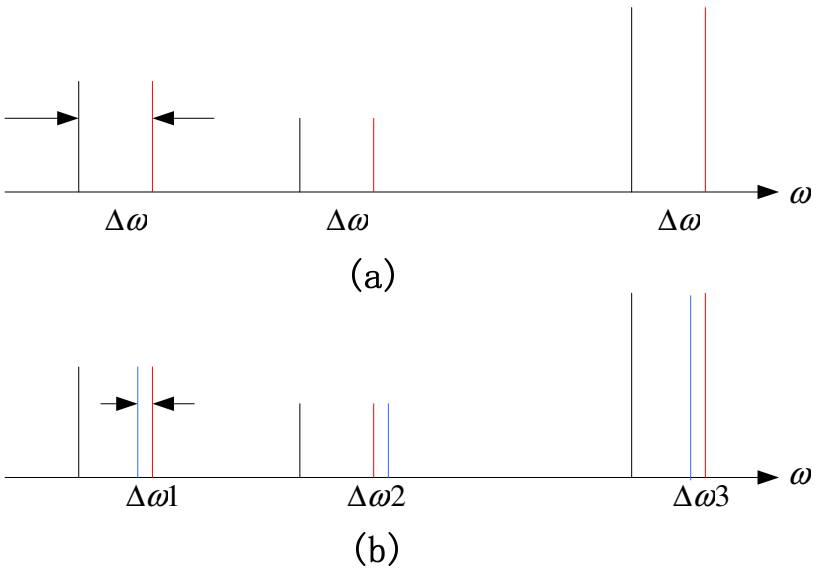

Figure 2.2: (a) Global frequency shift (b) local variations

Recall (2.7), if a global shift $\Delta\omega$ exists, the A matrix will update as

$$\bar{A} = \begin{pmatrix} e^{b_{01}t_1}e^{j\Delta\omega t_1} & \cdots & e^{b_{0M}t_1}e^{j\Delta\omega t_1} & a_{01}t_1e^{b_{01}t_1}e^{j\Delta\omega t_1} & \cdots & a_{0M}t_1e^{b_{0M}t_1}e^{j\Delta\omega t_1} \\ \vdots & \vdots & \vdots & \vdots & \vdots & \vdots \\ e^{b_{01}t_n}e^{j\Delta\omega t_n} & \cdots & e^{b_{0M}t_n}e^{j\Delta\omega t_n} & a_{01}t_ne^{b_{01}t_n}e^{j\Delta\omega t_n} & \cdots & a_{0M}t_ne^{b_{0M}t_n}e^{j\Delta\omega t_n} \end{pmatrix} \quad (2.10)$$

let

$$D = \begin{pmatrix} e^{j\Delta\omega t_1} & 0 & 0 & 0 & \cdots\cdots & 0 \\ 0 & e^{j\Delta\omega t_2} & 0 & 0 & \cdots\cdots & 0 \\ \vdots & \vdots & \vdots & \vdots & \vdots & \vdots \\ 0 & 0 & 0 & 0 & \cdots\cdots & e^{j\Delta\omega t_n} \end{pmatrix}$$

then

$$\bar{A} = A \times D \quad (2.11)$$

Notice that the updated $\bar{A}$ can be represented as the original A multiplying by a diagonal matrix with terms $e^{j\Delta\omega t_i}$. When we apply the updated $\bar{A}$ in (2.9),

$$\begin{aligned} \mathrm{tr}\left\{(\bar{A}^H\bar{A})^{-1}\right\} &= \mathrm{tr}\left\{(D^HA^HAD)^{-1}\right\} \\ &= \mathrm{tr}\left\{(ADD^HA^H)^{-1}\right\} \\ &= \mathrm{tr}\left\{(A^HA)^{-1}\right\} \end{aligned} \tag{2.12}$$

These two diagonal matrices multiplied together are identity. Therefore, the mean squared error will not change with a global shift $\Delta\omega$ and so does selection result. Thus in MRSI, the echo-time selection is minimally affected by global frequency shifts due to field inhomogeneity.

Sometimes, the number of remaining echo-time values is required to be relatively large. For EPI acquisition, if we only scan one k-space frame, corresponding to one echo-time value, within one excitation, the total acquisition time will still be long. By exploiting multi-echo EPI, one can acquire multiple k-space images within one excitation to further reduce the acquisition time. The basic timing scheme of Multi-Echo EPI is shown in Figure 2.3. The phase gradient $G_y(t)$ is rewound to the original starting position after each k-space image to ensure identical k-space trajectories for all echo-images. Furthermore, the adjacent echo-time values used in one excitation should be just long enough to accommodate one k-space frame acquisition so that scanning time is not wasted between k-space frames. The time difference between adjacent echoes cannot be smaller than one k-space frame acquisition time, or the k-space frames cannot be completely collected.

To achieve this purpose, we modify the selection algorithm. Instead of removing one echo-time value at each elimination step, the modified algorithm removes multiple echo-time values simultaneously. We consider candidate echo-time values for individual k-space frames to be laid out uniformly in time as shown in Figure 2.4a. The square red dots represent the elimination pattern, while the round black dots represent other time choices to which the elimination array can be shifted. Figure 2.4b shows an example of elimination using a

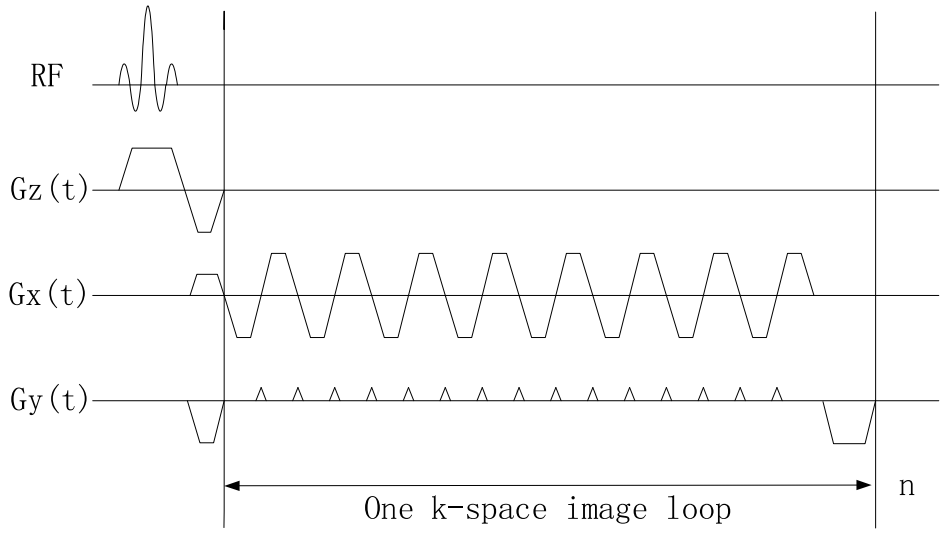

Figure 2.3: Basic multi-echo EPI sequence

periodic pattern to remove the least useful twelve echo-time points, four at a time. That is to say: the red, green and blue frames are not collected in the acquisition process; only black frames are actually acquired. In general, the selection algorithm allows the elimination pattern to be arbitrarily spaced. However, if the elimination pattern is unequally spaced, sometimes the remaining echo-time points cannot be efficiently used in multi-echo EPI. Therefore, we restrict the elimination pattern to be equally spaced and the echo interval to be a little longer than one k-space frame acquisition time. The MSE criterion for multi-echo selection can be generalized as

$$\mathrm{tr}\{(\tilde{A}^H\tilde{A})^{-1}\} = \mathrm{tr}\{(A^HA)^{-1}\} + \mathrm{tr}\{\frac{R_j(A^HA)^{-2}R_j^H}{1 - R_j(A^HA)^{-1}R_j^H}\} \tag{2.13}$$

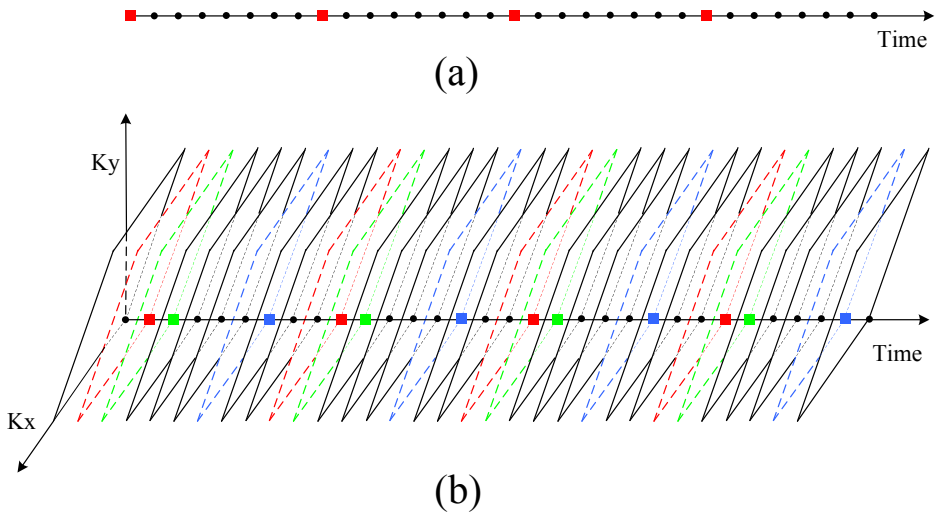

Figure 2.4: (a) Elimination pattern (b) periodic nonuniform elimination

where R_j represents the j^{th} combination of several rows in A, which corresponds to echo-time values that might be removed simultaneously in one elimination step. The combination that minimizes the term on the right is selected for elimination.

2.2 Phantom Experiment

2.2.1 Materials and Methods

Data from a ^1H phantom intended to verify the selection algorithm was acquired on a 4.7T 60cm-vertical-bore Varian primate MRI system (Varian Inc., Palo Alto, CA) at the University of Alabama at Birmingham, courtesy of Prof. Donald B. Twieg. The phantom, shown as Figure 2.5, was constructed from four cylindrical test tubes. One of them (right upper corner) held a methanol and water mixture with a 1:1 volume ratio. The other three tubes held ethanol and water mixtures with a 1:1 volume ratio. The four tubes were arranged in a rectangular configuration and placed inside a larger glass cylinder filled with water.

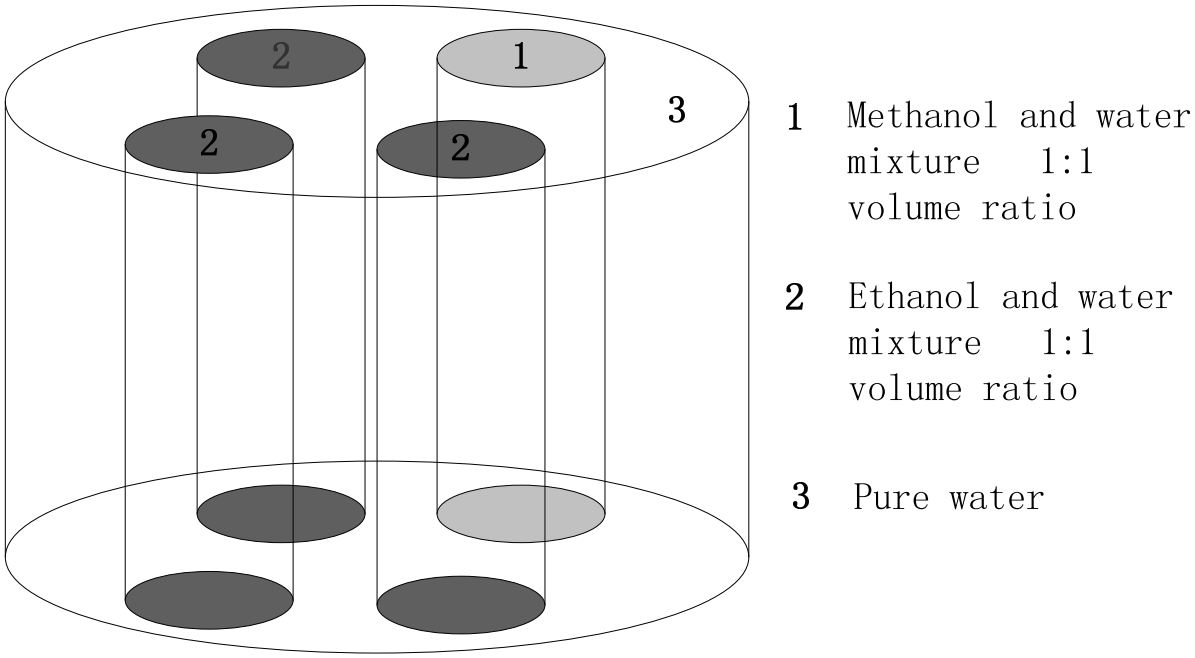

Figure 2.5: Phantom structure

Figure 2.6 shows spectra of the phantom obtained with a conventional phase-encoding technique. Chemical shifts are relative to hydroxyl at 4.7T. In the methanol-water spectrum, the methyl (CH_3) peak is 298 Hz downfield from hydroxyl (OH), while the signal contribution of $CH_3 : OH \approx 1 : 1.8$. In the ethanol-water spectrum, the ethyl (CH_2) peak is 241 Hz and the methyl peak is 728 Hz downfield from hydroxyl, while the signal contribution of $CH_2 : CH_3 : OH \approx 2 : 3 : 7.5$. These parameters are treated as prior information which is used in the selection algorithm.

3-D MRSI data were observed by echo-planar imaging with a traditional bottom-up uniform trajectory as shown in Figure 1.4b. 500 echoes separated by 0.3788ms were used in the EPI acquisition (from 17.81ms to 206.83ms). These represent the distribution of echo times available for optimal echo-time selection. Note that in practice only the optimized echo-time EPI frames would be acquired, whereas here all EPI frames were acquired so that different sampling patterns could be studied. In this work, the time required for one EPI

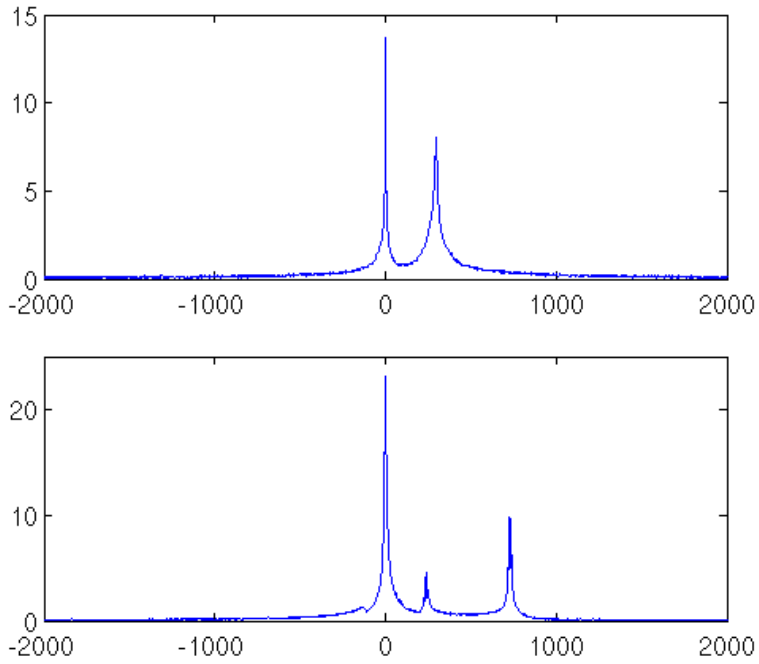

Figure 2.6: ^1H spectrum of methanol (upper plot) ^1H spectrum of ethanol (lower plot)

frame acquisition is 32.77ms. Therefore, if we want to utilize multi-echo EPI, the adjacent k-space images acquired within one excitation must have at least 32.77 ms echo-time difference. In addition, the phase gradient needs some time to rewind to the original starting position after each k-space image. Thus, we chose the elimination pattern with a 34 ms interval. The spectral bandwidth was 2640Hz, and spatial resolution was 2mm×2mm with a 64×64 matrix.

Since the EPI technique is used in this work, each k-space frame cannot be collected instantly. In other words, every k-space sample will have its own time delay even in the same frame. Therefore, we cannot simply use fast Fourier Transforms to reconstruct the images. Furthermore, an FFT cannot separate spatial information from different metabolite resonances. Therefore, we use conjugate gradients (CG) to find the best matching parameters of the images. (details are discussed in Chapter 4).

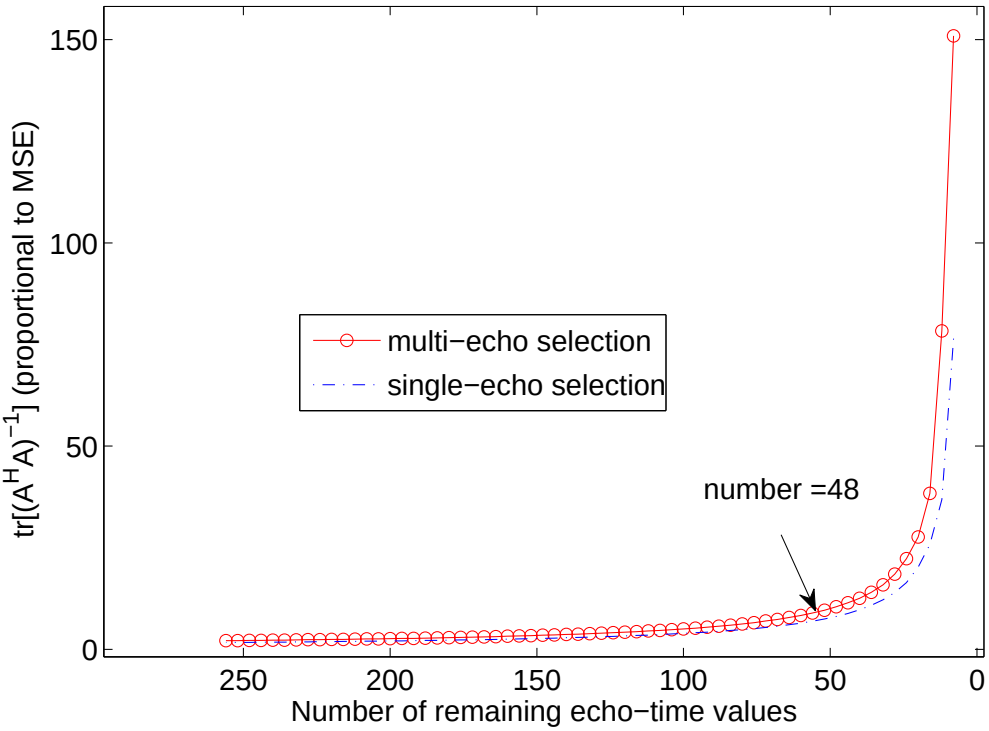

Figure 2.7: Number of remaining echo-time values vs. tr $\left\{(A^H A)^{-1}\right\}$ (which is proportional to MSE)

Here all programming used MATLAB running on a single core of a workstation equipped with 2.4 GHz AMD Opteron 880 dual-core processors (@Xi Computer Corp).

2.2.2 Results

In order to compare the speed and accuracy of single/multi-echo algorithms, we use both methods to eliminate echo-time values (from 500 available echoes). The multi-echo algorithm removes four values at a time. Figure 2.7 shows how the error criteria vary with the number of remaining echo-time values.

We observe that the single-echo selection has better MSE performance. However, the MSE performance of the multi-echo selection is almost as good. In both cases, the MSE

increases significantly when the number of remaining echo-time values is less than 48 but increases slowly when the remaining number is greater than 80. Nyquist density is not necessary for our selection technique. Because the remaining echoes are nonuniformly spaced and we have prior information about the spectral peaks, the Nyquist criterion does not apply. The selection time (average of 100 repetitions) comparison of the two selection methods is shown in Table 2.1. For the same number of remaining echoes, the multi-echo selection is much faster. In both selection processes, eliminating all but 32 echo times can be accomplished in less than 5 seconds. Even if real-time selection is necessary, the time required is feasible for clinical applications. However, sufficient prior information may be available to do the selection offline before the imaging session begins.

Table 2.1: Selection Time Comparison (s)

Number of remaining echo-time values	256	128	96	64	48	32
Single-echo selection time	3.0352	3.8885	4.0268	4.0325	4.0455	4.0657
Multi-echo selection time	0.4031	0.4990	0.5152	0.5248	0.5298	0.5354

Since MSE from the multi-echo technique is comparable to the single-echo techique and it has advantages in the acquisition process, we used the multi-echo algorithm (eliminating echo-time values four at a time) to demonstrate the value of the selection technique. Forty-eight out of five hundred echo-time values were selected for EPI acquisition, and these collected EPI data were used for image reconstruction. For comparison purposes, images reconstructed from 500 echoes were treated as ground truth. We also reconstructed images from 48 out of 500 randomly selected echoes and 48 out of 500 equally spaced echoes.

Figure 2.8 shows reconstructed spatial details at different resonant frequencies. When water mixes with ethanol or methanol, their hydroxyls exchange very quickly. Therefore, we can treat all hydroxyls in the phantom as having the same resonant frequency. Hence, the hydroxyl resonance should exist at every spatial location of the cylindrical container and four tubes (Figure 2.8, first column). Only ethanol has an ethyl part; when the spatial distribution

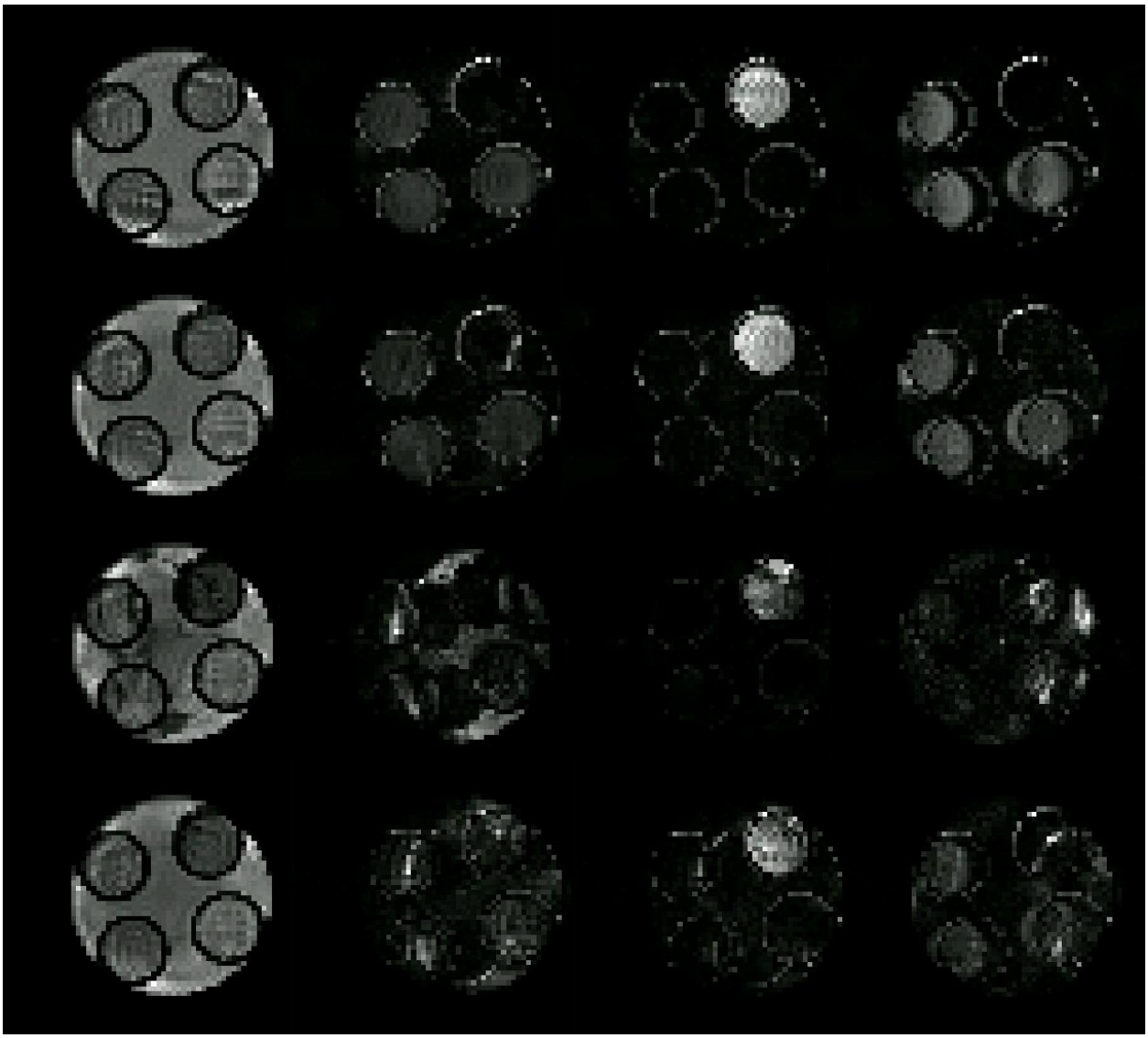

Figure 2.8: Spatial images reconstructed from 500 echo-time values (first row), 48 optimized echo-time values (second row), 48 randomly selected echo-time values (third row), 48 equally spaced echo-time values (fourth row). Each column from left to right represents spatial distributions of: hydroxyl, ethyl, methyl of methanol, methyl of ethanol.

of ethyl is shown, the resonant signals should only appear in the three ethanol tubes (Figure 2.8, second column). Both ethanol and methanol have a methyl part; however, the molecular environments around the methyl are very different from each other. Consequently, there are two resonances of methyl, one from ethanol and another one from methanol. In other words, when the spatial distribution of methyl from methanol is shown, there should be no signals in the ethanol tube (Figure 2.8, third column); when the spatial distribution of methyl from ethanol is shown, there should be no signals in the methanol tube (Figure 2.8, fourth column).

Figure 2.9 shows reconstructed spectra at different spatial locations. In the water-ethanol tube, there should be three resonant peaks from hydroxyl, ethyl and methyl (Figure 2.9, upper plot); in the water-methanol tube, there should be two resonant peaks from hydroxyl and methyl (Figure 2.9, middle plot); in the big glass cylinder filled with water, there should be only one resonant peak from hydroxyl (Figure 2.9, lower plot).

As shown in the spatial and spectal reconstruction results, both multi-echo SBS and full selection distinguished these four different resonances well. The spatial distribution and spectra display good agreement between the full data set and the optimized echo-time data set. In contrast, random selection and equally spaced selection yielded much greater reconstruction errors and artifacts, and they did not separate different resonant frequencies clearly.

2.3 Discussion

In this chapter, we presented a novel technique to accelerate the data acquisition in MRSI. An efficient SBS method was developed to optimize the echo-time selection in the context of multi-echo EPI. We analyzed the computation time and reconstruction MSE of this selection algorithm and demonstrated its feasibility in MRSI acquisition. The phantom experiments demonstrate that spatial maps of different resonances of interest can be separated with a limited number of echo-time values if those echo times are chosen properly. In

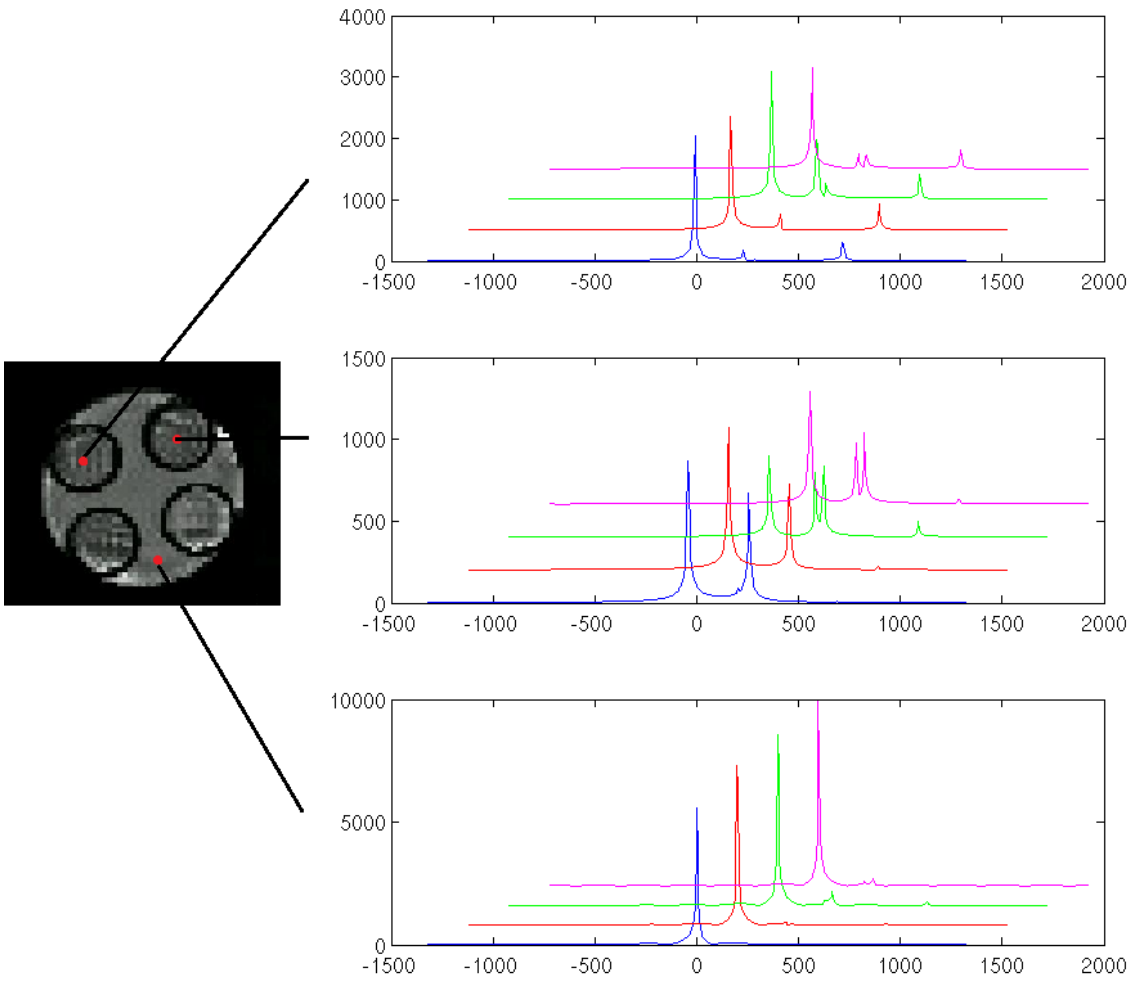

Figure 2.9: Spectra in the tube of water and ethanol mixture (upper plot), in the tube of water and methanol mixture (middle plot), in the big glass cylinder of pure water (lower plot). Each plot from lower left to upper right from: 500 echo-time values, 48 optimized echo-time values, 48 randomly selected echo-time values, and 48 equally spaced echo-time values. Plots are offset for easier viewing.

addition, spatial maps of different spectra can also be reconstructed properly with a limited number of echo-time values. In our experiments, the volume of acquired data for the optimized selection was only 9.6% that of the full echo-time set. Thus, the proposed method has great potential to reduce overall acquisition time for obtaining spatial maps of spectral peaks of interest.

As mentioned in the Materials and Methods subsection, linearization is an important step of the selection algorithm. If the prior values $a_{0i}, d_{0i}, \omega_{0i}$ have the same values as unknown signal parameters a_i, d_i, ω_i, (2.6) is equal to (2.5). Therefore, accuracy of the prior information is a factor in the selection performance. In order to understand the impact of each kind of parameter on the selection performance, we did separate tests with parameter offsets of magnitude, decay and frequency. Each study adheres to the following the experiment flow, as shown in Figure 2.10. Using original parameters instead of estimated parameters in the selection, the specific combination of selected echo-time values can be totally different. However, that does not means the echo-time selection relying on the estimated parameters is not good. A more reasonable way to evaluate the selection performance is to examine how much the MSE increases if the parameters used in the selection process vary from the true parameters. Thus, a selection is made with parameters that are perturbed from the true parameters, and the reconstruction MSE for that selection is evaluated assuming the true parameters. Meanwhile, the reference MSE for the selection from the true parameters is approximated using the linearized matrix equation around the true parameters, which is asymptotically accurate as noise variance decreases. Here we treat the parameters reconstructed from 500 echo-time values as original values.

For each kind of parameter, we tested 10 offset ranges. For each offset range, we repeated the experiment flow 1000 times with random offsets in that range to find the minimum, maximum and average MSE increases. Figure 2.11 shows how the MSE increase was affected by different parameter offsets. In Figure 2.11a, when estimated magnitudes are randomly perturbed by a maximum offset of 10% of the original magnitudes, the minimum MSE

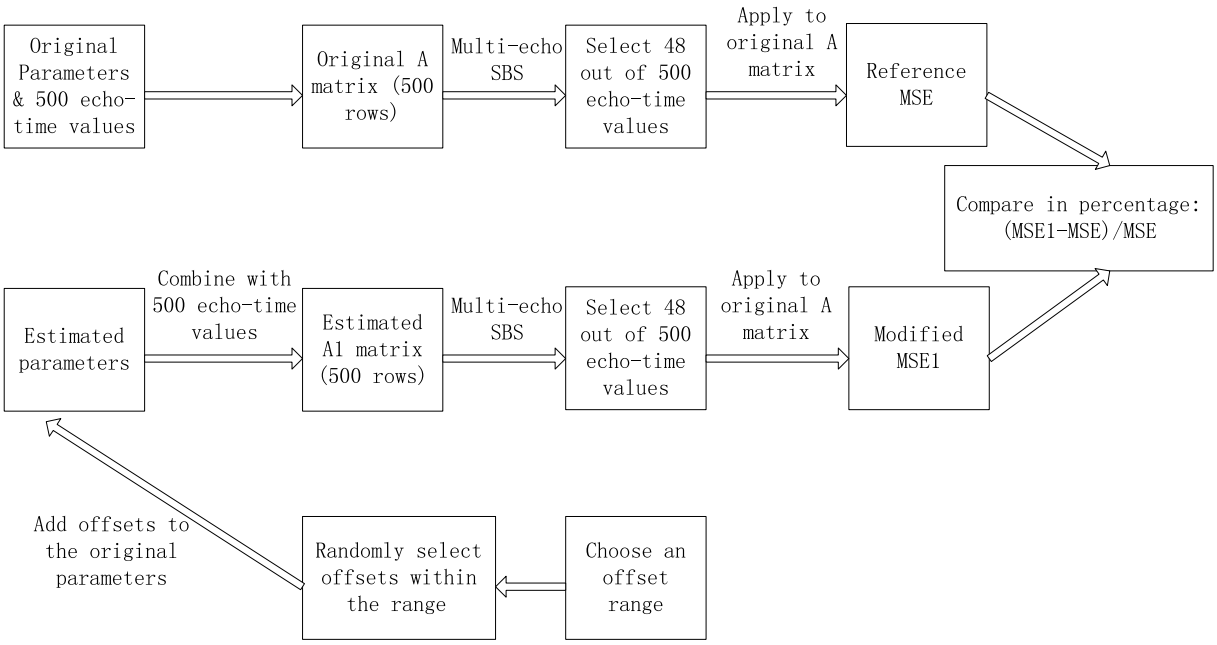

Figure 2.10: Experiment flow: Parameter offsets affect the selection performance

increase is 0%, the maximum MSE increase is 0.2% and the average MSE increase within 10% offset range is 0.01%. Similarly, when estimated magnitudes are randomly perturbed by a maximum of 15% to 50% from the original magnitudes, the maximum increase in MSE goes from 0.25% to 4.3%. The average increase in MSE goes from 0.04% to 0.37%. In Figure 2.11b, when estimated decays are randomly perturbed by a maximum of 10% to 50% from the original decays, the maximum increase in MSE goes from 0.7% to 9.3%, and the average increase in MSE goes from 0.23% to 1.6%. In Figure 2.11c, when estimated frequencies are randomly perturbed by a maximum of 1 to 10 Hz offset from the original frequencies, the maximum increase in MSE goes from 0.2% to 23%, and the average increase in MSE goes from 0.05% to 3.5%.

From these observations, errors in prior knowledge of magnitudes have the smallest effect on echo-time selection performance. If the magnitude error is limited to 50%, the MSE increase is less than 5%. Errors in prior knowledge of decay have a larger effect on

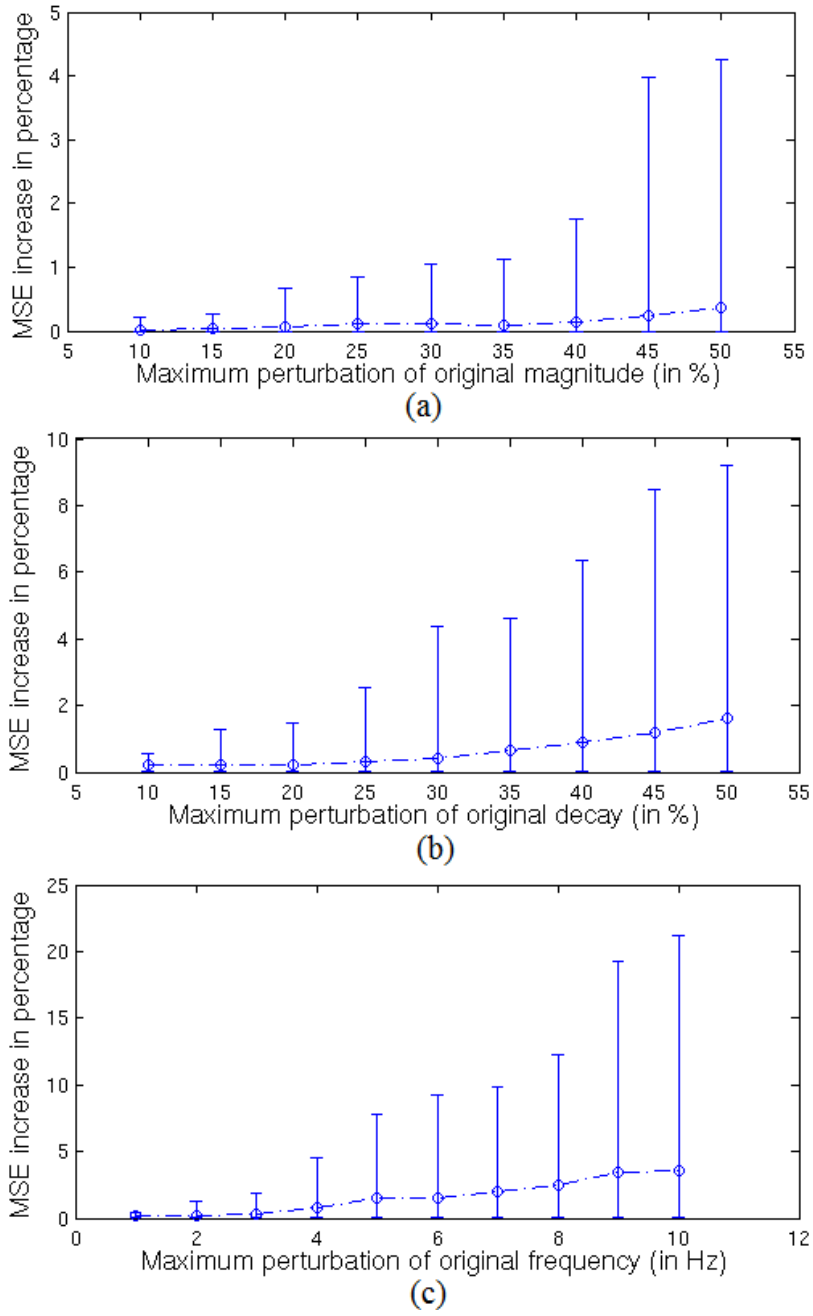

Figure 2.11: MSE increase as a function of (a) magnitude offset (b) decay offset (c) frequency offset

echo-time selection. However, if we can keep the maximum decay error within 50%, the MSE increase can be limited to 10%. Compared to the resonant frequencies themselves, the frequency offset is relatively small. But the maximum MSE amplifies rapidly with the increase of frequency offset. Therefore, frequency accuracy is the most critical factor in echo-time selection. In practice, the chemical shifts of common metabolites used in MRSI are well known. In addition, normally the local variations of the resonant frequencies change very little, while frequency global shifts have no effect on the optimality of the echo-time selection as shown in Section 2.1.2.

For the proposed method, the MSE decreases when the number of selected echoes increases (Figure 2.7), which means the reconstruction quality improves with more data acquisition. For equally spaced selection and random selection, however, this property is not true. Figure 2.13 shows the MSE variation based on the number of remaining echo-time values. All the parameters come from prior information. For these sampling methods, MSE does not decrease monotonically when the number of echoes increases. In other words, equally spaced selection and random selection cannot guarantee better reconstruction results with more acquisition data. For the equal sampling pattern, we know that the frequency bandwith is the reciprocal of time resolution [24]. When the bandwidth is larger than any of the frequency differences, which means the time resolution (the echo-time interval) is fine enough, there will be no aliasing (Figure 2.12a $\Delta\omega < bw1$). However, once the difference between two resonant frequencies is an integral multiple of the spectral bandwidth (Figure 2.12b $\Delta\omega = 2bw2$), reconstruction from equally spaced selection cannot separate resonant peaks due to aliasing.

In our phantom experiment, the time difference between adjacent echoes for equally spaced selection is 4.1668 ms and the spectral bandwidth is 239.9 Hz. The frequency difference between hydroxyl and ethyl is 241 Hz, and the frequency difference between hydroxyl and methyl from ethanol is 487 Hz. Both differences are close to an integral multiple of 239.9 Hz, hence the reconstruction from equally spaced selection cannot separate these three

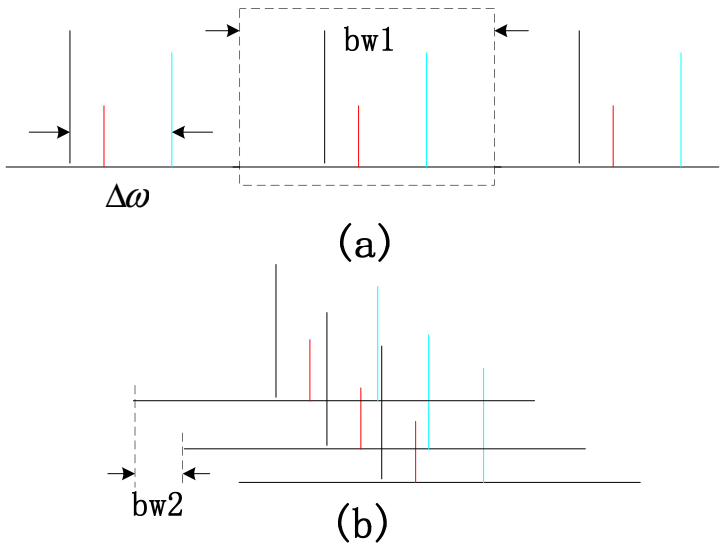

Figure 2.12: Spectrum of equally-spaced selection (a) from a small echo-time interval (b) from a large echo-time interval.

resonances properly. For random selection, the echo-time values are not optimized, and the performance is-not surprisingly-random. Thus, random selection is not reliable for data acquisition either.

In the selection procedure, a global frequency shift of resonannces has no effect on the optimality of the selection. However, in the reconstruction procedure, large global shifts must be compensated by a field map (This will be discussed in more detail in Chapter 5). Otherwise, spectral peaks may be initialized too far from the correct values, resulting in a failure to find these values due to local minima. Consequently, magnitudes and decays of metabolite resonances will also be incorrect.

In conclusion, we have developed an efficient echo-time selection technique, which can be easily implemented in MRSI acquisition. A lower-than-Nyquist density can be achieved with the proposed method. It greatly reduces the data requirements (and thus acquisition time) without sacrificing spatial and spectral accuracy in reconstruction.

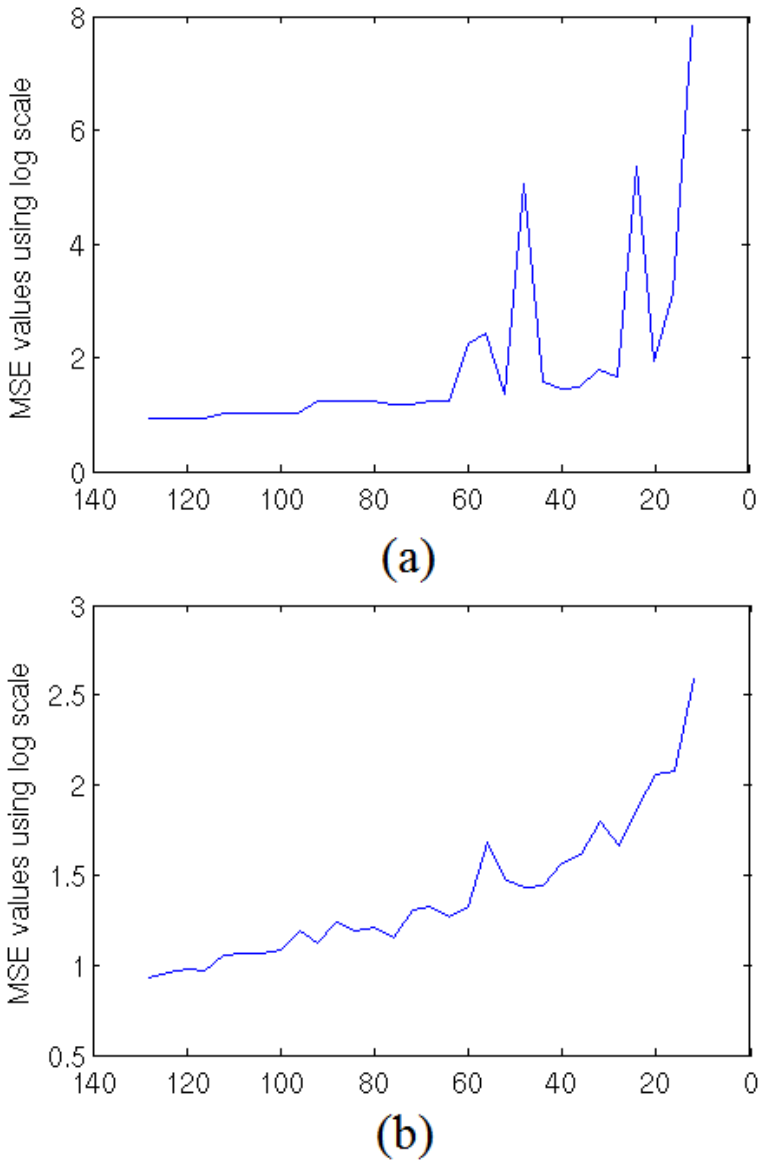

Figure 2.13: MSE as a function of the number of remaining echo-time values (a) with equally spaced selection (b) with random selection

Chapter 3

Alternative Optimal Data Acquisitions

In the previous chapter, we focused on selection techniques which choose the best echo-time values for echo-planar imaging acquisitions, while keeping high-resolution of k-space coverage. In fact, using EPI, a high-resolution k-space image cannot be acquired instantly at a single echo time; instead EPI requires a relatively long readout time. Every k-space sample has its own time delay even in the same k-space frame. Therefore, the echo-time selection might be optimal for a subset of k-space data but may not be the best choice for every k-space datum. Thus, in EPI, acquiring full coverage of k-space at each selected echo-time is somewhat imprecise. In addition, we cannot simply ignore the time required to scan each echo and use FFTs to reconstruct the images, because of this relative long acquisition time for high-resolution k-space frames.

With these issues in mind, we introduce two alternative selection strategies: one is k-t selection, which use the sequential backward selection in both k-space and time domains; another one is echo-time selection that explicitly utilizes overlapped EPI, which can reduce the acquisition time for each k-space image and allows the possibility of using FFTs to shorten the reconstruction procedure.

3.1 Optimal k-t Selection

Unlike the echo-time selection method, the k-t selection algorithm considers the k-space and time domain selection simultaneously. We try to choose the most useful k-t samples, which are then acquired for image reconstruction.

As shown in Figure 3.1a, for standard echo-planar imaging, the k-space data are distributed uniformly in the k_y direction. This is because the pulse blips in the G_y direction

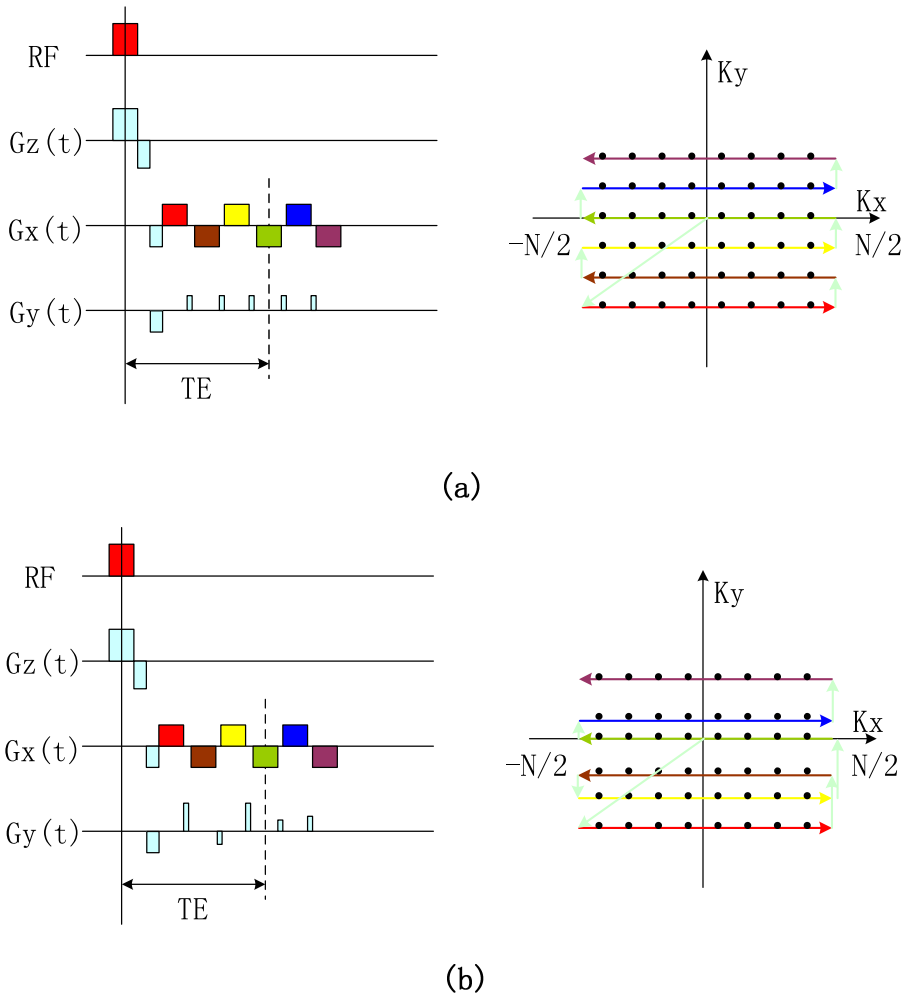

Figure 3.1: (a) Standard EPI with uniform k-space acquisition (b) Modified EPI with nonuniform k-space acquisition

have the same amplitudes and durations, leading to equal spacing. Similarly, the k-space data are also distributed uniformly in the k_x direction. The reason is the pulses in the G_x direction have the same amplitudes and durations. Here we can see that, for the same k_y value, the k_x value can vary from $-N/2$ to $N/2$, which means the data acquisition in the k_x direction is much faster than in the k_y direction. Therefore, we still maintain full coverage in the k_x direction and limit our k-t data selection only in k_y-t domain.

If we change the pulse amplitude or duration of G_y, the sample density in the k_y direction changes. Normally, there is no data collection during the k_y jump, so we keep the duration of each pulse in the G_y direction short. When the pulse amplitude increases, the trajectory will jump by a bigger step in the k_y direction. When the pulse amplitude decreases, the trajectory will shrink to a smaller jump in the k_y direction. In consequence, the nonuniform k-space frame can be acquired, as shown in Figure 3.1(b). Once the locations in the k_y domain are determined, the pulse sequence for G_y can be implemented in echo-planar imaging.

3.1.1 k-t Selection Theory

Figure 3.2 shows the main idea of k-t selection theory: all potential samples are supposed to lie on a uniform grid (black dots) in both k_y and t domains. And the red dots represent the selected k_y-t locations. As the figure shows, at some time points several k_y samples are selected, while at some time points no k_y sample is chosen. Similarly, at different k_y locations, the number of selected time samples varies. On the other hand, at each selected k_y-t location, we still fully sample the k_x dimension.

Similar to the echo-time selection, k-t selection also utilizes the sequential backward selection algorithm. Consider a linear observation model in matrix notation:

$$\rho = Aq + e \tag{3.1}$$

.

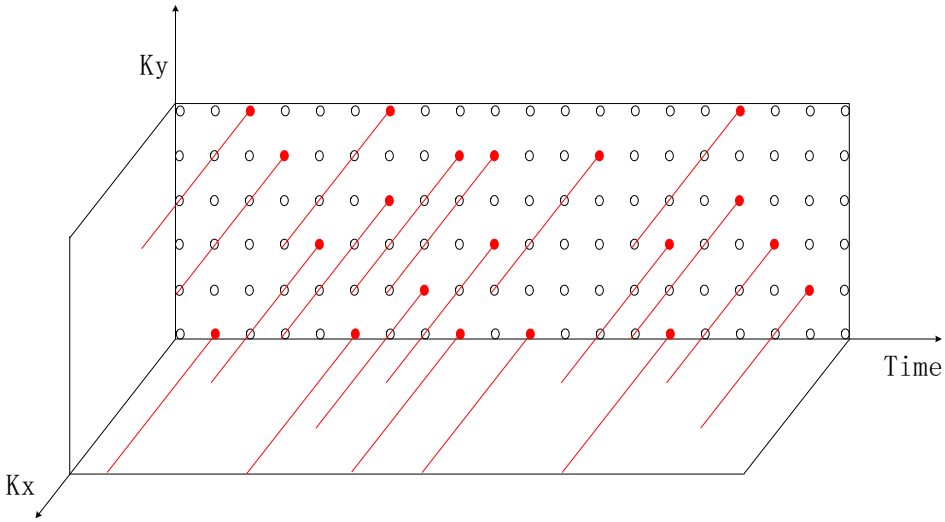

Figure 3.2: k_y-t data selection strategy

where ρ is a set of observations, q is the unknown vector of interest, A is the transformation matrix and e represents zero-mean white Gaussian noise. Then the mean squared error in the reconstruction is proportional to

$$E\left\{\|\hat{q}-q\|^2\right\} = \mathrm{tr}\left\{(A^H A)^{-1}\right\} \tag{3.2}$$

This error criterion only depends on the transformation matrix A. Once we determine the A matrix, the MSE is fixed and consequently the reconstruction quality of q is determined. Since we fully sample the k_x direction, an inverse FFT can be directly applied to the k_x direction to get x spatial information. Here we only consider k_y in k-space and y in the spatial domain. For most types of MRSI, a k_y-t acquired image model can be described as:

$$\rho(k_y,t) = \sum_{y=1}^{N}\sum_{i}^{M} a_i(y)\exp\left\{[-d_i(y)+j\omega_i(y)]t\right\}\exp\left[-j2\pi(k_y y)\right] \tag{3.3}$$

where M is the number of metabolite resonances contained in a voxel, N is the spatial coverage in the y direction, and a_i, ω_i and d_i are the complex weight, resonant frequency and decay rate of each resonance. In order to utilize the error criterion shown in (3.2), we need to modify (3.3) and make it linear in the parameters of interest. After a linearized approximation, (3.3) becomes:

$$\rho(k_y,t) = \sum_{y=1}^{N}\sum_{i=1}^{M} a_i(y)\exp\left[b_{0i}(y)t\right]\exp\left[-j2\pi(k_y y)\right] + b_i(y)ta_{0i}(y)\exp\left[b_{0i}(y)t\right]\exp\left[-j2\pi(k_y y)\right]$$
$$- b_{0i}(y)ta_{0i}(y)\exp\left[b_{0i}(y)t\right]\exp\left[-j2\pi(k_y y)\right] + e(t) \tag{3.4}$$

where $b_i = -d_i + \omega_i$. a_i and b_i are unknown signal parameters, while a_{0i} and b_{0i} are known from prior information. The noise term $e(t)$ is zero-mean, white Gaussian noise. Equation (3.4) can be rewritten in matrix format, as the unknown parameters $q = [a_1(y_1), \ldots, a_M(y_1), a_1(y_2), \ldots, a_M(y_2), \ldots, a_1(y_N),$
$\ldots, a_M(y_N), b_1(y_1), \ldots, b_M(y_1), b_1(y_2), \ldots, b_M(y_2), \ldots, b_1(y_N), \ldots, b_M(y_N)]^T$. The transformation matrix is then given by

$$A = \begin{pmatrix}
P_{1:M,y_1}(k_y(1),t(1)) & \cdots & P_{1:M,y_N}(k_y(1),t(1)) & Q_{1:M,y_1}(k_y(1),t(1)) & \cdots & Q_{1:M,y_N}(k_y(1),t(1)) \\
P_{1:M,y_1}(k_y(2),t(1)) & \cdots & P_{1:M,y_N}(k_y(2),t(1)) & Q_{1:M,y_1}(k_y(2),t(1)) & \cdots & Q_{1:M,y_N}(k_y(2),t(1)) \\
\vdots & \vdots & \vdots & \vdots & \vdots & \vdots \\
P_{1:M,y_1}(k_y(N),t(1)) & \cdots & P_{1:M,y_N}(k_y(N),t(1)) & Q_{1:M,y_1}(k_y(N),t(1)) & \cdots & Q_{1:M,y_N}(k_y(N),t(1)) \\
\vdots & \vdots & \vdots & \vdots & \vdots & \vdots \\
\vdots & \vdots & \vdots & \vdots & \vdots & \vdots \\
P_{1:M,y_1}(k_y(N),t(n)) & \cdots & P_{1:M,y_N}(k_y(N),t(n)) & Q_{1:M,y_1}(k_y(N),t(n)) & \cdots & Q_{1:M,Ny_N}(k_y(N),t(n))
\end{pmatrix} \tag{3.5}$$

where

$$P_{1:M,y_l}(k_y(j),t(h)) = [e^{b_{01}t(h)}e^{-j2\pi k_y(j)\times l},\cdots,e^{b_{0M}t(h)}e^{-j2\pi k_y(j)\times l}]$$
$$Q_{1:M,y_l}(k_y(j),t(h)) = [t(h)a_{01}e^{b_{01}t(h)}e^{-j2\pi k_y(j)\times l},\cdots,t(h)a_{0M}e^{b_{0M}t(h)}e^{-j2\pi k_y(j)\times l}]$$

At this point, A has two sets of variables, the choice of k_y and t. Each row of A corresponds to a specific (k_y, t) sample. Hence, optimizing the combination of rows in A means selecting the optimal combination of (k_y, t) samples which determines the quality of the reconstructed images. The MSE value is not merely a function of the number of rows remaining in A. The specific choice of (k_y, t) samples is more important than the number of samples that are selected. Compared to individual echo-time selection, the transformation matrix is much bigger in (k_y, t) data selection. Thus, even using the sequential technique, the k-t selection requires longer computation time. The good thing is, in many clinical applications, sufficient prior information may be available to do the selection offline before the imaging session begins.

In the selection procedure, we begin with all possible (k_y, t) samples and evaluate all possible choices of eliminating a single row from the current A, which corresponds to a specific (k_y, t) sample. Then the least important row, which causes the smallest MSE increase, will be removed from A. This process is repeated until the desired number of (k_y, t) samples remain. Experiments shows that if there is no constraint in k-t selection procedure, the remaining (k_y, t) samples scatter in a seemingly random pattern.

3.1.2 k-t Selection with Constraint

As we mentioned at the beginning of this chapter, using EPI, the entire k-space cannot be acquired instantly at a single echo time; every k-space sample has its own time delay even in the same k-space frame. Therefore, we can modify our echo-time selection into the k_y-t domain in a more accurate way, as shown in Figure 3.3a. If time points 1, 9, 17 and 25

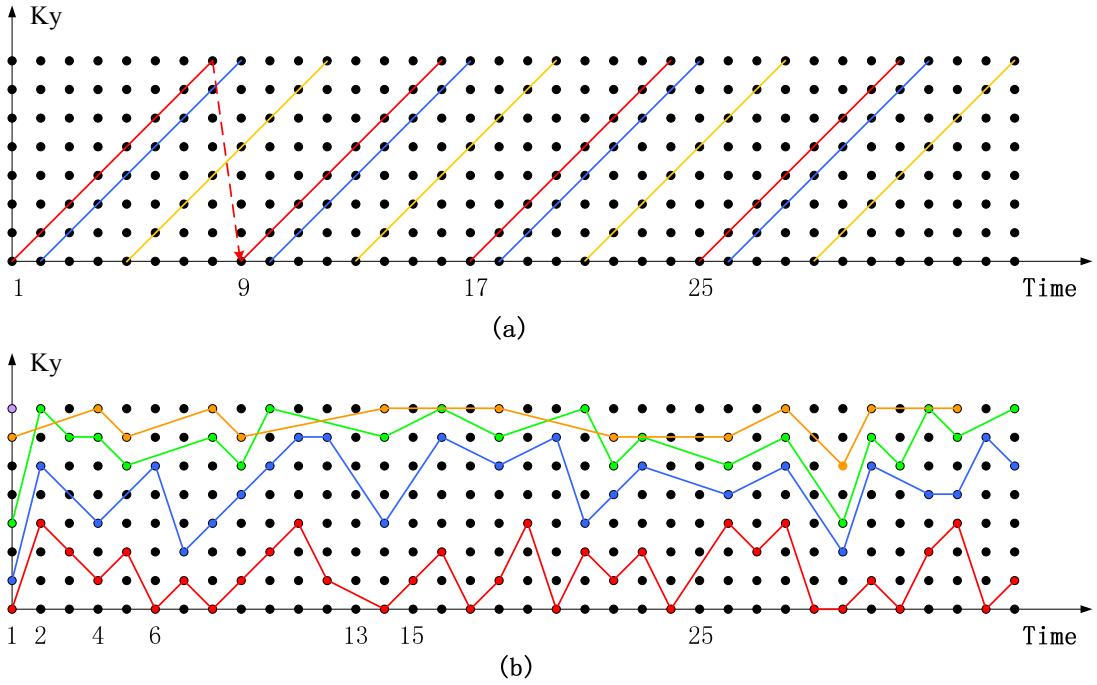

Figure 3.3: Trajectory of (a) multi-echo EPI selection (b) k-t selection without constraint

are selected in echo-time selection, this implies that all samples along the four red lines are chosen in k-t selection.

In Figure 3.3, we have 8×36 potential (k_y, t) samples in total (black dots), and our goal is to select the optimal 96 of them. Utilizing muti-echo time selection (acquiring 4 k-space images in one shot), only three excitations are needed to acquire the 96 (k_y, t) samples. If non-constrained k-t selection is used, the acquired k_y-t samples have no specific pattern as shown in Figure 3.3b. At time point 1, five k_y samples are selected (red dot, blue dot, green dot, yellow dot and purple dot); at time point 2, three k_y samples are selected; at time point 4, four k_y samples are selected; at time point 6, two k_y samples are selected; at time point 13, no k_y sample is selected; and at time point 15, only one k_y sample is selected. For one excitation, we can only pick one k_y sample at one time point. Therefore, we need at least five excitations (shown as five color trajectories) to acquire 96 (k_y, t) data. None of these trajectories can collect a selected point at every available sample time, so the overall scheme

is inefficient. For example, the red trjactory misses k_y samples at time point 13 and point 25. Other color trajectories miss more k_y samples during one excitation. Consequently, even though this k-t selection can achieve smaller MSE with the same amount of data (details in Experiment section) than echo-time selection, it still somewhat wastes acquisition time.

In order to avoid wasting acquisition time, we update the k-t selection technique with a constraint. Assume the the potential range of the k_y-t domain is $m \times n$ and the total number of desired (k_y, t) samples is N. In order to get fully efficient acquisition in one excitation, at each time point one k_y sample must be selected. Then $q = N/n$ excitations are needed to acquire the total N samples. Figure 3.4 shows an overview of the updated method: (1) create an accumulator for each time point and set the initial value to zero; (2) use the SBS technique to eleminate the least useful (k_y, t) sample, which make the smallest increment of MSE; (3) determine the time point (i) of the selected sample and increment the i_{th} accumulator by one; (4) compare the value of accumulator to $(m - q)$, if it is smaller than $(m - q)$; then repeat Step 2 and 3; if it is larger than $(m - q)$, shrink the potential k-t selection range to exclude all samples at time point i; (5) repeat Steps 2, 3 and 4 until the desired number of (k_y, t) samples remain. Of course, the k-t selection with constraint has less freedom in selection, but it greatly enhance the acquisition efficiency compared to the original k-t selection method. More comparison details are shown in the experiment section.

3.2 Echo-Time Selection with Overlapped EPI

For the k-t selection with or without constraint, the pulse sequence design would be a challenge, because it requires different k-space trajectories for each excitation. Hence, we introduce another selection method: echo-time selection with overlapped EPI, which is still a form of time domain selection and much easier in the pulse sequence design.

In EPI, every k-space sample has its own time delay within the same k-space frame. A high-resolution k-space image (including many k-space samples) requires long scanning time. Therefore, the original echo-time selection technique is somewhat imprecise because it

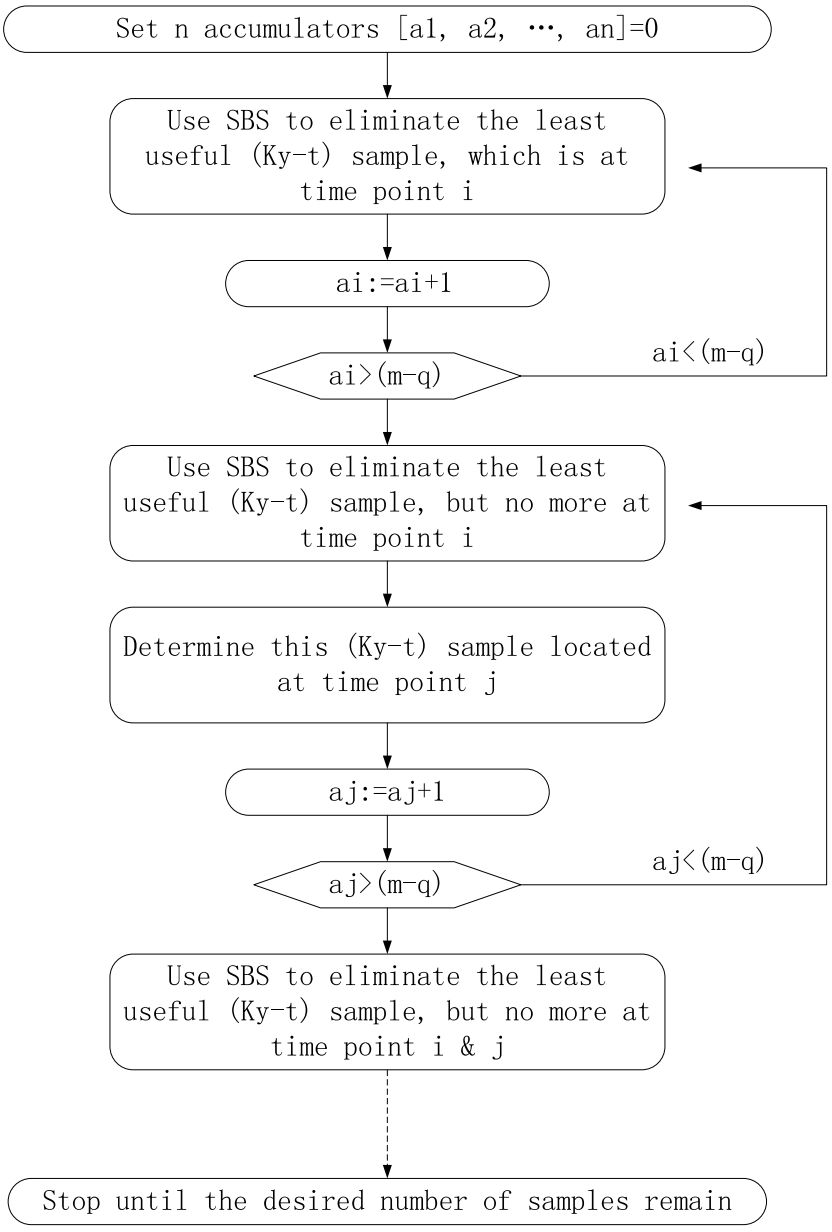

Figure 3.4: Flow of the updated method

assumes full coverage of k-space at each selected echo-time. However, if we can acquire the entire k-space in a negligible period, then the echo-time values we choose would be optimal for more samples of the selected k-space frame.

For traditional echo-planar imaging, the observed data are distributed uniformly in the whole k-space domain as shown in Figure 3.5a. TR1 is the total readout time for a whole k-space image. If we want to decrease the readout time, we can simply reduce the resolution either in the k_x domain, k_y domain or both. Since for the same k_y value, the k_x value varies (data acquisition in the k_x direction is much faster than in the k_y direction), we here only consider reducing the resolution in the k_y direction.

When we double the pulse amplitude in the G_y direction shown in Figure 3.5b , the jump size in the k_y direction also doubles and the sample density in the k_y direction becomes half of the original one. Scanning the same k-space range, the total number of k-space samples in this frame will be halved and the readout time, TR2, is consequently half of TR1. On the other hand, in some clinical applications, especially in locating abnormal biochemistry in specific tissues, high-resolution in k-space is very important. We want to shrink the readout time but without sacrificing the spatial resolution. Hence, in the next excitation, another half-resolution k-space image is acquired at the same echo-time as shown in 3.5c. The only thing different between these two low-resolution k-space frames is the initial setup of G_y: ΔG_{Y1} is larger than ΔG_{Y2}, so there is an offset in the k_y direction between the blue trajectory and red trajectory. In consequence, we can combine these two images into one with full k-space coverage, and the image readout time shrinks to half.

For one full-coverage k-space image, the orignal EPI requires one excitation and there is one echo-time value to represent the whole k-space image with TR_1 readout time; while the overlapped EPI requires two excitations and also only one echo-time value to represent this k-space image with smaller ($TR2$) readout time. That is, the original EPI is more efficient in data acquisition, while the overlapped EPI is more accurate in echo selection.

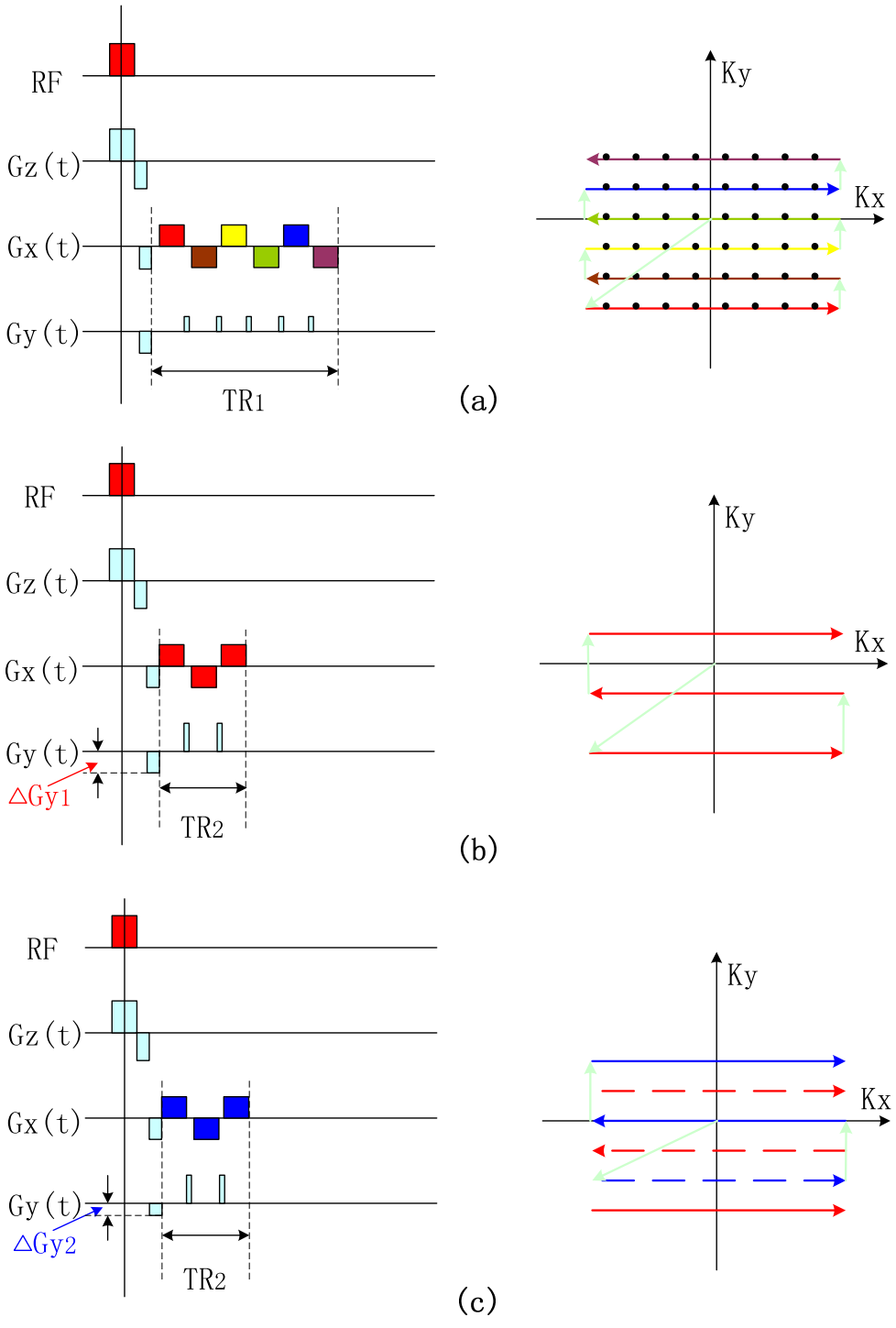

Figure 3.5: (a) Standard EPI with uniform k-space acquisition (b,c) Modified EPI with coarse k_y resolution

In order to increase the efficiency of overlapped EPI acquisition, we try to observe more echoes during one excitation than in original EPI. For regular multi-echo EPI, as shown in 3.6a, four full-coverage k-space frames (four different echoes) are acquired in one excitation. These four images are distributed equally in the time domain ($= TR_1$) for high efficiency of data acquisition. So we choose these four echoes as a set in the echo-time selection process. During the next excitation, another set (four full-coverage) of k-space frames are acquired with an optimal time shift, which is calculated in SBS echo-time selection. For overlapped multi-echo EPI, as shown in 3.6b, eight half-coverage k-space frames (eight different echoes) are acquired in one excitation. The time interval of these echoes is TR_2 for data acquisition efficiency. Here we choose these eight echoes as a set in the echo-time selection process. During the next excitation, another eight half-coverage k-space frames are acquired using the same echo time values.

For one excitation process, both selection methods acquire the same amount of k-space data. For the same acqusition efficiency, regular EPI has more flexibility in choosing echo-time values, while echo time values selected for the overlapped EPI are more accurate in representing one k-space image. Because the k-space images acquired in overlapped EPI have a shorter readout time, FFTs may be sufficient for reconstructing spatial information. Similarly, if we want to reduce the readout time further for one k-space image, we can reduce the resolution of k_y more but with even less flexibility in echo-time selection.

3.3 Experiments and Comparisons

3.3.1 Materials and Methods

To compare the performance of different selection methods, 3-D MRSI data were observed by conventional phase-encoding imaging. During one excitation, data is acquired uniformly along the time domain at one k-space location at the red-dot line shown in Figure 3.7. For the next excitation, the pulse sequence changes the k-space location and rewinds to the original time point to start acquiring data at the blue-dot line shown in Figure 3.7.

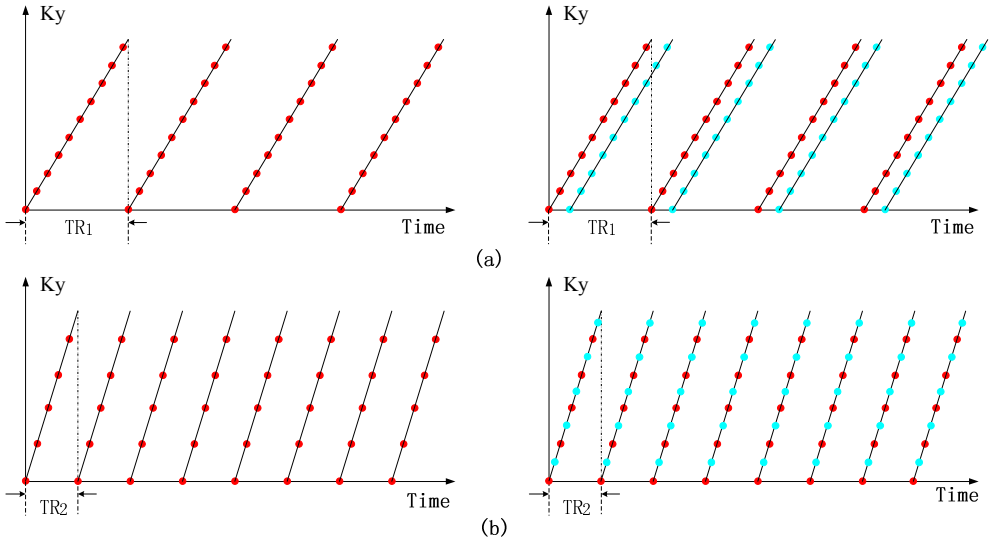

Figure 3.6: (a) Traditional multi-echo EPI with uniform k-space acquisition for two excitation (b) Modified multi-echo EPI with coarse k_y resolutions for two excitation

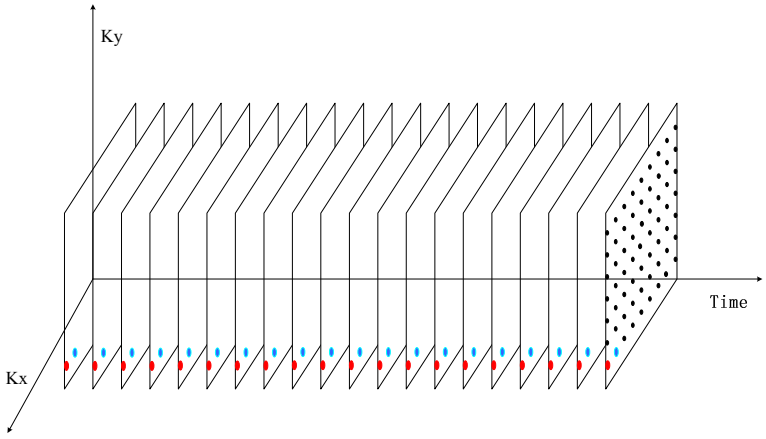

Figure 3.7: Data distribution of conventional phase-encoding imaging

Consequently, after a number of excitations, at each time point, we can get a full k-space image, in which the k-space date is distributed uniformly.

In our experiment, 1024 time points separated by 0.5ms and 64 uniformly located k_y samples acquired. These represent the distribution of (k_y, t) samples available for optimal selection. Note that the phase-encoding imaging utilized, which has uniform distribution in k_y and time domain, was used here for acquisition so that different sampling patterns could be studied under the same experiment conditions. In practice echo planar imaging would be used in the acquisition for all of these selection methods.

The ^1H phantom was acquired in a 4.7T 60cm-vertical-bore Varian primate MRI system (Varian Inc., Palo Alto, CA) at the University of Alabama at Birmingham. The phantom, shown in Figure 3.8, was constructed from four cylindrical tubes. Three of them held methanol and water mixture with a 1:4 volume ratio, while the other tube (left lower corner) and the large glass cylinder were filled with pure water. Chemical shifts are relative to hydroxyl at 4.7T. In the methanol-water spectrum, the methyl (CH_3) peak is 298Hz downfield from hydroxyl (OH), while the signal contribution of $CH_3 : OH \approx 1 : 6.2$. These parameters are treated as prior information, which is used in the selection algorithms. The spectral bandwidth was 2000Hz, and spatial resolution was 2mm×2mm with a 64×64 matrix.

3.3.2 Results

Table 3.1: Selection Time(s) and MSE Comparison

	Selection time	MSE
k-t selection with constraint (3072 remaining (k_y, t) samples out of 65,536)	7,565.4	8.8634
k-t selection without constraint (3072 remaining (k_y, t) samples out of 65,536)	13,565.4	8.2845
Regular multi-echo time selection (48 remaining t samples out of 1024, eliminate 4 at a time)	4.413	11.3561
Overlapped multi-echo time selection (eight frames in one excitation) (48 remaining t samples out of 1024, eliminate 8 at a time)	1.096	12.6538

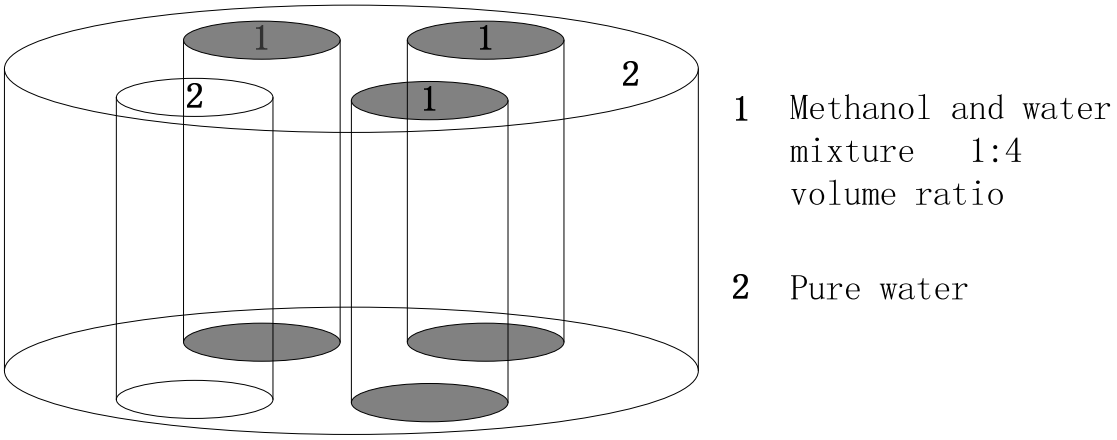

Figure 3.8: Phantom structure

Table 3.1 shows the comparisons of the selection time and mean-square errors of four selection methods mentioned in this chapter: k-t selection with constraint, k-t selection without constraint, regular muti-echo time selection (eliminate four least informative echoes at a time and at each of the remaining echoes, one full coverage k-space image is acquired) and overlapped multi-echo time selection (eliminate eight least informative echoes at a time and at each of the remaining echoes, two half coverage k-space image are acquired). The two k-t selection methods retained 3072 (k_y, t) samples out of 65,536, while the two echo-time selections retained 48 time samples out of 1024.

As discussed in Section 3.1.2, to compare these selection methods in a more resonable way, we should transfer the selection results from both echo-time selections to the k-t domain as shown in Figure 3.3a. For instance, if 48 echo-time values remain in echo-time selection, there should be $48 \times N$ (N is the resolution in k_y domain, in this experiment N=64) samples left after k-t selection. Therefore, 48 echo-time values and 3072 (k_y, t) samples represent the same amount of remaining k-space data.

Two echo-time selection methods have a much faster selection process than the two k-t selection methods. This is because when we use the SBS algorithm to eliminate samples in these methods, the transformation matrix A (see (2.7) and (3.5)) has very different sizes.

Therefore, when we eliminate samples by calculating the MSE using $\mathrm{tr}\left\{(A^H A)\right\}$, the processing time will be much different. The k-t selection without constraint has an even slower selection process than the k-t selection with constraint. The reason is, for the k-t selection with constraint, once all the desired number of samples have been eliminated at one time point t_i, we shrink the potential k-t selection range. This eliminates all samples at time point i, which reduces the size of transformation matrix A faster.

The two k-t selection techinques have better MSE performance than the two echo-time selections. The MSE of the two k-t selection methods are comparable and so is the MSE of the two echo-time selection techniques. Nyquist density is not necessary for our selection techniques. Because the remaining samples from these selection methods are all nonuniformly spaced and we have prior information about the spectral peaks, the Nyquist criterion does not apply.

Since MSE from k-t selection with constraint is comparable to k-t selection without constraint and the constrained version has higher scanning efficiency in the acquisition process, we used the k-t selection with constraint to demonstrate the value of the k-t selection technique. 3072 out of 65,536 (k_y, t) samples were selected for modified EPI acquisition, and these collected EPI data were used for image reconstruction later. For regular muti-echo selection, 48 out of 1024 echo-time values were selected for regular EPI acquisition (eliminating echo-time values four at a time); for overlapped muti-echo selection, 48 out of 1024 echo-time values were selected for overlapped EPI acquisition (eliminating echo-time values eight at a time). Of course, when the remaining echo-time values are determined, we also need to transfer these echo-time values to (k_y, t) samples to make the comparison fair. For comparison purposes, images reconstructed from full k-space data were treated as ground truth. We also reconstructed images from 48 out of 1024 equally spaced echoes.

Figure 3.9 shows reconstructed spatial details at different resonant frequencies using different selection techniques. When water mixes with methanol, their hydroxyls exchange very quickly. Therefore, we can treat all hydroxyls in the phantom as having the same

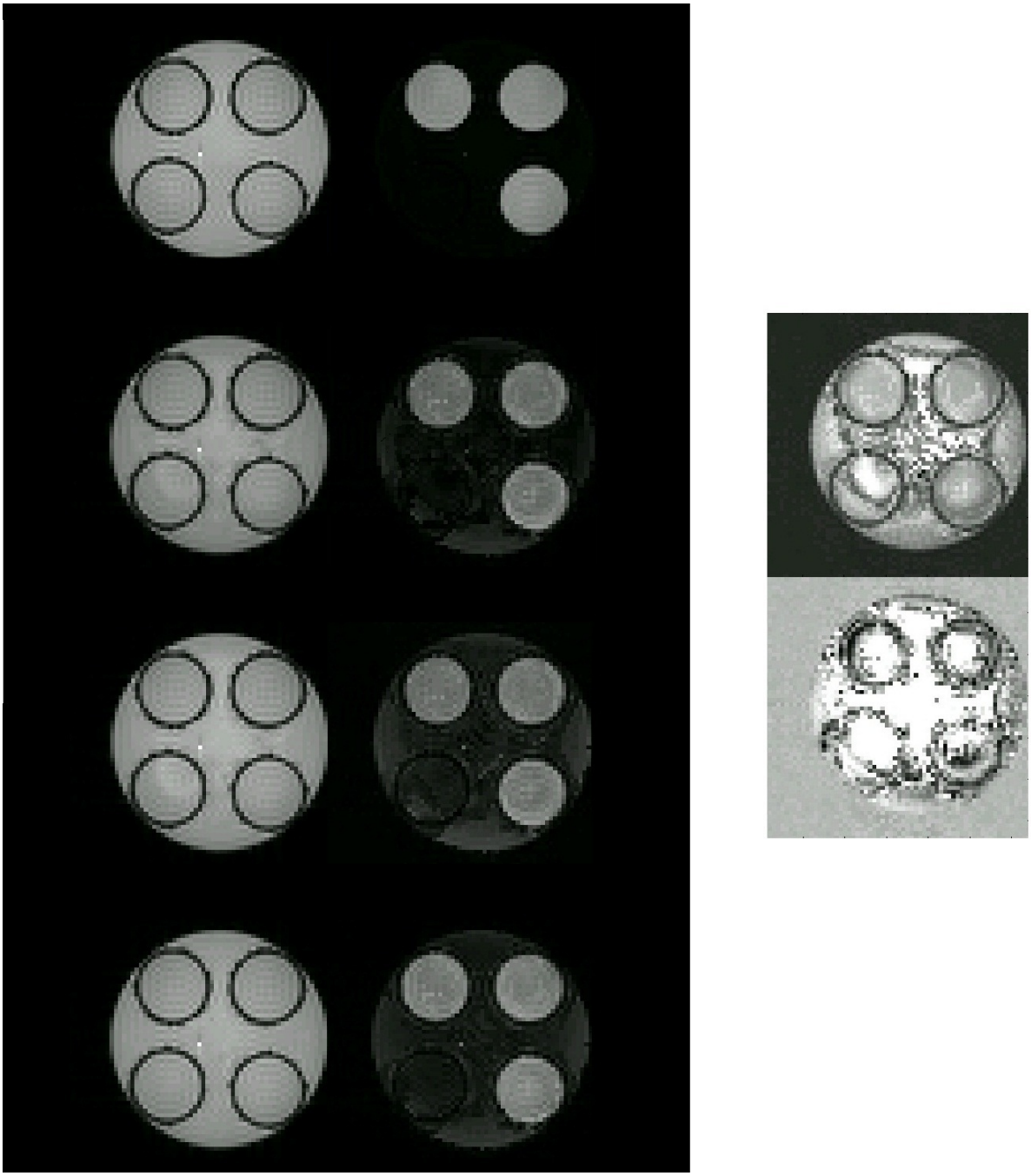

Figure 3.9: Spatial images on the left picture are reconstructed from full k-space data (first row), 3072 optimized (k_y, t) samples out of 65,536 (second row), 48 optimized echo-time values using regular echo-time selection (third row), 48 optimized echo-time values using overlapped echo-time selection (fourth row). The first column represents spatial distributions of hydroxyl; the second column represents spatial distributions of methyl. Spatial images on the right picture are reconstructed from 48 equally spaced echo-time values. The upper image represents spatial distribution of hydroxyl and the lower image represents spatial distribution of methyl.

resonant frequency. Hence, a hydroxyl resonance should exist at every spatial location of the cylindrical container and four tubes (Figure 3.9, first column of the left picture and the upper image of the right picture). Besides the hydroxyl part, methanol also has a methyl part. When the spatial distribution of methyl is shown, the resonant signals should only appear in the three methanol tubes: upper two tubes and right lower one (Figure 3.9, second column of the left picture and the lower image of the right picture). We observed that the images reconstructed from both full selection data and k-t selection data can distinguish these two resonances very well. Both echo-time selection methods have good reconstruction performance in hydroxyl images, although there are some small artifacts in the reconstructed methyl images. In contrast, equally spaced selection yielded much greater reconstruction errors and artifacts and it did not separate different resonant frequencies clearly.

Figure 3.10 shows reconstructed spectra at different spatial locations. In the big glass cylinder and left lower tube filled with water, there should be only one resonant peak from hydroxyl (Figure 3.10, left plot). However, the reconstructed spectra from the two echo-time selection methods also have tiny spikes at methyl resonant frequency, which should not appear. Clearly the spectra reconstructed from k-t selection displays better agreement with the full data set than other selection methods. In the other three water-methanol tubes, there should be two resonant peaks from hydroxyl and methyl (Figure 3.10, right plot). All selection techniques except equally spaced echoes show good reconstruction results.

3.3.3 Conclusion

This chapter introduces two new data selection methods. Compared to the original echo-time selection technique, each of them has advantages and limitations. k-t selection expands the selection range from only the time domain to both k-space and time domains. It makes the selection process more accurate, and the reconstructed images from selected samples have better quality. However, the k-t selection technique has more demanding requirements in pulse sequence design and requires longer computation time to select the most informative

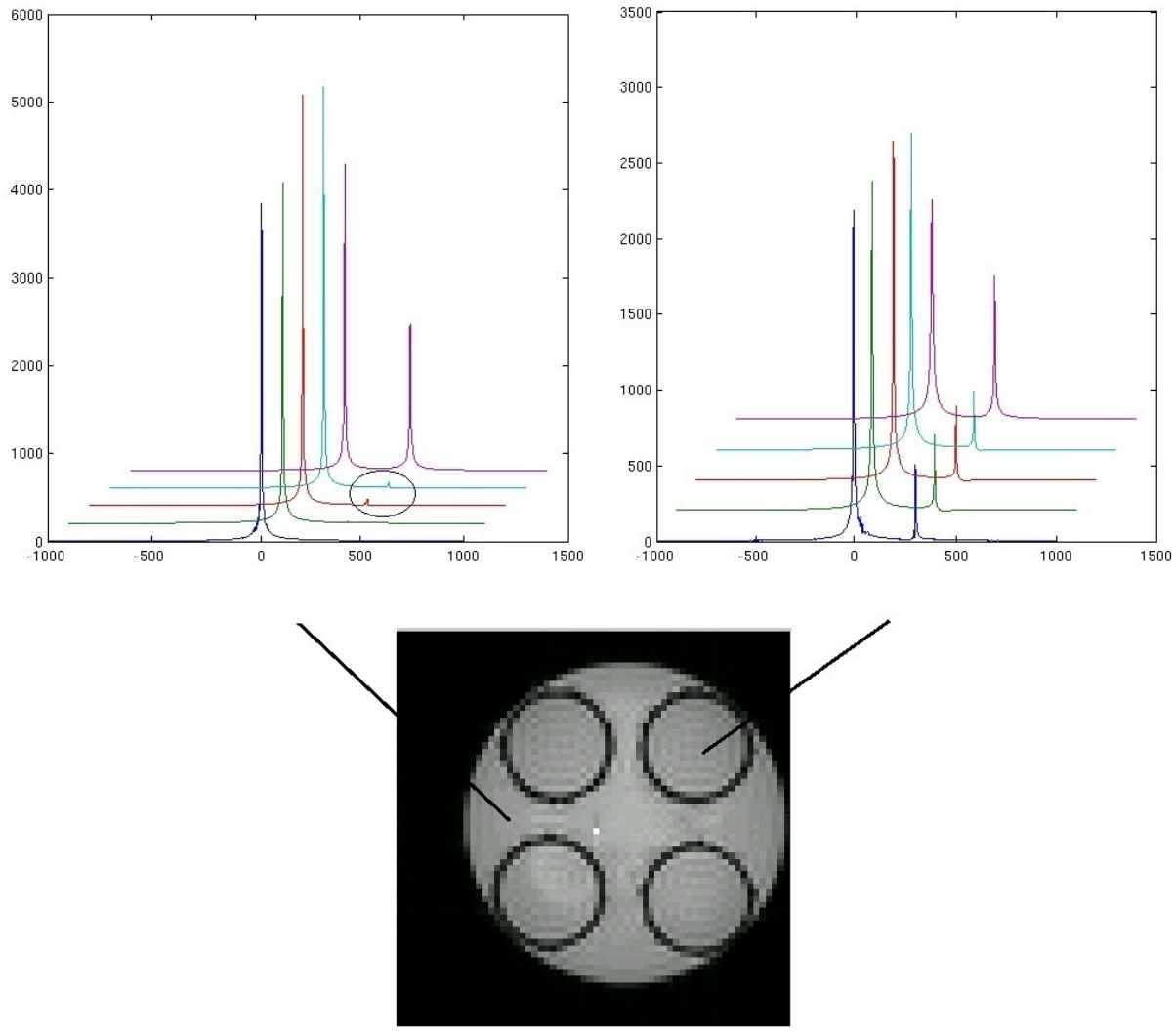

Figure 3.10: Spectra in the big glass cylinder and lower left tube full of pure water (left plot), in the tubes of water and methanol mixture (right plot). Each plot from lower left to upper right from: full data set, 3072 optimized (k_y, t) samples out of 65,536, 48 optimized echo-time values using regular echo-time selection, 48 optimized echo-time values using overlapped echo-time selection, and 48 equally spaced echo-time values. Plots are offset for easier viewing.

(k, t) samples. On the other hand, the echo-time selection using overlapped EPI can be easily implemented in MSRI acquisition. The selection process can be done in seconds, so even if real-time selection is necessary, the selection time is feasible for many applications. Another advantage of overlapped echo-time selection is that the acquired k-space images has relative short readout time. In this case, FFTs might be good for spatial reconstruction, which leads to a much faster reconstruction procedure. From our experimental data, we can also observe that the reconstruction quality is comparable to the original echo-time selection but is not as good as the k-t selection method.

In summary, choosing the selection methods depends on the application demands. If the application requires real-time selection, either the original echo-time selection or echo-time selection with overlapped EPI would be good. In addition, if a fast reconstruction process is desired, echo-time selection with overlapped EPI might be the best choice. In another aspect, if sufficient prior information is available and selection offline before the imaging session is acceptable, the k-t selection method would be preferred because it yields smaller reconstruction errors and artifacts.

Chapter 4

Fast Reconstruction for Nonlinear Model

In our research work, echo-planar imaging is used for image acquisition, which allows us to obtain single/multiple k-space image(s) with one excitation. EPI models each datum as a sample in the (k, t) domains rather than a non-time-varying k-space image. In other words, every k-space datum has its own time delay (leading to local decay and phase variations) even in the same frame. Therefore, fast Fourier Transforms (FFTs) directly used in k-space can cause artifacts in the reconstruction. Additionally, for our proposed acquisition methods, the observed k-space data are selected based on sequential backward selection algorithm and normally are sampled nonuniformly in the time domain. Therefore, an FFT is not appropriate to separate spectrum information from different metabolite resonances either. In this chapter, we present a fast iterative reconstruction method by applying polynomial approximations to the exponential time functionand and then utilizing FFTs to find the best matching parameters of the images. Simulation and phantom experiments demonstrate that our approach achieves satisfactory reconstruction quality while largely reducing computation time.

4.1 Introduction to Iterative Reconstruction Method

As mentioned in Chapter 2, the observations of MRSI from echo-planar imaging can be represented as

$$s(t) = \int\int \rho(x, y, t) \exp\left\{-j2\pi[k_x(t)x + k_y(t)y]\right\} dxdy \tag{4.1}$$

and the discrete version of (4.1) is given by

$$s(t_n) = \sum_x \sum_y \rho(x, y, t_n) \exp\{-j2\pi[k_x(t_n)x + k_y(t_n)y]\} \tag{4.2}$$

in which the time-dependent spatial distribution $\rho(x, y, t_n)$ is

$$\rho(x, y, t_n) = \sum_{i=1}^{M} a_i(x, y) \exp\{[-d_i(x, y) + j\omega_i(x, y)]t_n\} \tag{4.3}$$

where M is the number of metabolite resonances contained in a voxel, $a_i(x, y)$, $d_i(x, y)$ and $\omega_i(x, y)$ are signal parameters we want to estimate from the observed signal $s(t_n)$ by solving (4.2) and t_n is the time point where we observe k-space data. From (4.2) and (4.3), one can understand EPI observation in another way: Fourier Transforms are taken at each time point t_n for $\rho(x, y, t_n)$, and only one sample at $[k_x(t_n), k_x(t_n)]$ in each k-space frame is selected instead of the whole k-space image. Therefore, if the image size is $N \times N$, for traditional MRI, we only need to perform one FFT to get one k-space image, while in EPI we need N^2 FFTs to get one k-space image.

For conventional phase-encoding MRSI, the spatial information $\rho(x, y, t_n)$ at each specific t_n can be reconstructed by taking the inverse Fourier Transform of k-space at t_n, because the trajectory within one k-space frame observes a single static image at the same time. The trajectory of EPI, however, samples the k-space of different spatial images that vary by an exponential time function $\exp(-d + j\omega)t_n$. Because the observation model is nonlinear in the parameters of interest and does not have the direct structure of an FFT, an iterative method is needed to reconstruct the spatial information.

Besides the spatial details, the spectral information is also important in spectroscopic imaging. For conventional phase-encoding MRSI, after taking the inverse Fourier transform of k-space at each t_n, one can do another direct FFT at every (x,y) location along the time domain to get the spectral information at each voxel. But for EPI acquisition with our proposed acquisition methods, the observed data normally are sampled nonuniformly in the

time domain and the average density is much lower that the Nyquist density. Therefore, one also needs to use an iterative method to reconstruct the spectral information.

The most common way to solve this problem is to use an iterative technique to reconstruct the image parameters (the spatial distribution $\boldsymbol{a}$, the decay rate $\boldsymbol{d}$ and the resonant frequency $\boldsymbol{\omega}$) instead of reconstructing spatial images and spectra. We propose to use an iterative conjugate-gradients (GC) algorithm to minimize the cost function:

$$C(\boldsymbol{p}) = \sum_{t_n} |s_{t_n} - \hat{s}_{t_n}(\boldsymbol{p})|^2 \tag{4.4}$$

with respect to $\boldsymbol{p}$, where $\boldsymbol{p}$ represents the image parameters: $\boldsymbol{a}$, $\boldsymbol{d}$ and $\boldsymbol{\omega}$. Here s_{t_n} is the observed data and $\hat{s}_{t_n}$ is the estimated data from (4.2).

The regular conjugate gradient algorithm used to reconstruct $\boldsymbol{p}$ is processed as follows [12]:

1. Initialize $\boldsymbol{p} = \boldsymbol{p}_0$
2. Calculate the gradients of parameters $\boldsymbol{g}_0 = -\nabla_{\boldsymbol{p}} C(\boldsymbol{p}_0)$. If $\boldsymbol{g}_0 = 0$, stop, else set $\Lambda \boldsymbol{p}_0 = -\boldsymbol{g}_0$
3. Line search $\alpha_k = \arg\min_{\alpha \geq 0} C(\boldsymbol{p}_k + \alpha_k \Lambda \boldsymbol{p}_k)$. Find the optimal α_k to minimize the cost function with updated parameters $(\boldsymbol{p}_k + \alpha_k \Lambda \boldsymbol{p}_k)$
4. Let $\boldsymbol{p}_{k+1} = \boldsymbol{p}_k + \alpha_k \Lambda \boldsymbol{p}_k$
5. Calculate the gradients of parameters $\boldsymbol{g}_{k+1} = -\nabla_{\boldsymbol{p}} C(\boldsymbol{p}_{k+1})$. If $\boldsymbol{g}_{k+1} = 0$, stop
6. $\beta_k = \frac{(\boldsymbol{g}_{k+1})^T \boldsymbol{g}_{k+1}}{(\boldsymbol{g}_k)^T \boldsymbol{g}_k}$
7. Set $\Lambda \boldsymbol{p}_{k+1} = -\boldsymbol{g}_{k+1} + \beta_k \Lambda \boldsymbol{p}_k$
8. Let $k = k + 1$; repeat from Step 3 to Step 8

In this procedure, Step 3 to Step 8 need to repeat as many times to achieve the optimal results. The line search calculation in Step 3 and gradients calculation in Step 5 are the two main computational parts of the operation.

4.1.1 Parameter Gradient

The computation of parameter gradients $\nabla_{\boldsymbol{p}} C$ includes three parts: $\partial C/\partial \boldsymbol{a}$, $\partial C/\partial \boldsymbol{d}$ and $\partial C/\partial \boldsymbol{\omega}$.

$$\begin{aligned} C(\boldsymbol{p}) &= \sum_{t_n} |s_{t_n} - \hat{s}_{t_n}(\boldsymbol{p})|^2 \\ &= \sum_{t_n} [\hat{s}_{t_n}(\boldsymbol{p}) - s_{t_n}][\hat{s}_{t_n}(\boldsymbol{p}) - s_{t_n}]^* \\ \frac{\partial C}{\partial \boldsymbol{a}} &= \sum_{t_n} \frac{\partial \hat{s}_{t_n}}{\partial \boldsymbol{a}} [\hat{s}_{t_n}(\boldsymbol{p}) - s_{t_n}]^* + [\hat{s}_{t_n}(\boldsymbol{p}) - s_{t_n}] \frac{\partial (\hat{s}_{t_n})^*}{\partial \boldsymbol{a}} \end{aligned} \tag{4.5}$$

Let $f_{t_n} = [\hat{s}_{t_n}(\boldsymbol{p}) - s_{t_n}]^*$. Combine with (4.2) plus (4.3), (4.5) can be modified as

$$\begin{aligned} \frac{\partial C}{\partial \boldsymbol{a}} &= \sum_{t_n} [\frac{\partial \hat{s}_{t_n}}{\partial \boldsymbol{a}} f_{t_n} + f_{t_n}^* \frac{\partial (\hat{s}_{t_n})^*}{\partial \boldsymbol{a}}] \\ &= 2\mathrm{Re}\{\sum_{t_n} \frac{\partial \hat{s}_{t_n}}{\partial \boldsymbol{a}} f_{t_n}\} \\ &= 2\mathrm{Re}\left\{\sum_{t_n} e^{(-\boldsymbol{d}+j\boldsymbol{\omega})t_n} e^{-j2\pi[k_x(t_n)x + k_y(t_n)y]} f_{t_n}\right\} \end{aligned} \tag{4.6}$$

Similarly, the other two types of gradients can be represented as

$$\begin{aligned}\frac{\partial C}{\partial \boldsymbol{d}} &= 2\mathrm{Re}\{\sum_{t_n}\frac{\partial \hat{s}_{t_n}}{\partial \boldsymbol{d}} f_{t_n}\} \\ &= 2\mathrm{Re}\left\{\sum_{t_n}\boldsymbol{a}e^{(-\boldsymbol{d}+j\boldsymbol{\omega})t_n}\times(-t_n)\times e^{-j2\pi[k_x(t_n)x+k_y(t_n)y]}f_{t_n}\right\} \qquad (4.7)\\ \frac{\partial C}{\partial \boldsymbol{\omega}} &= 2\mathrm{Re}\{\sum_{t_n}\frac{\partial \hat{s}_{t_n}}{\partial \boldsymbol{\omega}} f_{t_n}\} \\ &= 2\mathrm{Re}\left\{\sum_{t_n}\boldsymbol{a}e^{(-\boldsymbol{d}+j\boldsymbol{\omega})t_n}\times(jt_n)\times e^{-j2\pi[k_x(t_n)x+k_y(t_n)y]}f_{t_n}\right\} \qquad (4.8)\end{aligned}$$

For i^{th} resonance at (x,y) spatial location, these parameter gradients are described as

$$\frac{\partial C}{\partial a_i(x,y)} = 2\mathrm{Re}\left\{\sum_{t_n} e^{[-d_i(x,y)+j\omega_i(x,y)]t_n}e^{-j2\pi[k_x(t_n)x+k_y(t_n)y]}f_{t_n}\right\} \qquad (4.9)$$

$$\frac{\partial C}{\partial d_i(x,y)} = 2\mathrm{Re}\left\{\sum_{t_n} a_i(x,y)e^{[-d_i(x,y)+j\omega_i(x,y)]t_n}\times(-t_n)\times e^{-j2\pi[k_x(t_n)x+k_y(t_n)y]}f_{t_n}\right\} \qquad (4.10)$$

$$\frac{\partial C}{\partial \omega_i(x,y)} = 2\mathrm{Re}\left\{\sum_{t_n} a_i(x,y)e^{[-d_i(x,y)+j\omega_i(x,y)]t_n}\times(jt_n)\times e^{-j2\pi[k_x(t_n)x+k_y(t_n)y]}f_{t_n}\right\} \qquad (4.11)$$

4.1.2 Line Search

Line search is another critical step in the conjugate gradient method. After we calculate the gradients of parameters $\boldsymbol{g}$ and determine the directions of parameter optimization $\Lambda\boldsymbol{p}$, we need to figure out how large the adjustable step size α should be to minimize the error cost (4.4) at the current iteration. Exhaustive search for the optimal α is inefficient because we may need to try a large number of different α values and for each α value we try, we need to update the parameters and reevaluate (4.4), which is computationally intensive. Therefore, we desire to restrict the number of α values that we evaluate to minimize the cost function C. We numerically analyzed the function of $C(\alpha)$ and found that the cost function along α is a quadratic-like shape and the quadratic approximation can be used to reduce the computational complexity of the line search.

An overview of the quadratic approximation is described as follows (here "$C0$" represents the value of the cost function when $\alpha = 0$):

1. Initialize $\alpha = \alpha_1$ and update parameters as $\boldsymbol{p}_1 = \boldsymbol{p} + \alpha_1 \Lambda \boldsymbol{p}$.

2. Evaluate the cost function $C1$ as shown in (4.4) with the updated parameters $\boldsymbol{p}_1$.

3. Update parameters as $\boldsymbol{p}_2 = \boldsymbol{p} + 2\alpha_1 \Lambda \boldsymbol{p}$, and evaluate the cost function $C2$ based on updated parameters $\boldsymbol{p}_2$.

4. If $C0 \geq C1$ and $C2 > C1$, go to Step 7; else continue to the next step.

5. If $C0 \leq C1$, set $\alpha = 0.5\alpha_1$ and $C2 = C1$; update $\boldsymbol{p}_1 = \boldsymbol{p} + 0.5\alpha_1 \Lambda \boldsymbol{p}$; evaluate the cost function $C1$ with the updated parameters $\boldsymbol{p}_1$; and then go back to Step 4. Otherwise continue to the next step.

6. If $C0 > C1$ and $C1 > C2$, set $\alpha = 2\alpha_1$ and $C1 = C2$; update $\boldsymbol{p}_2 = \boldsymbol{p} + 2 \times 2\alpha_1 \Lambda \boldsymbol{p}$; evaluate the cost function $C2$ with the updated parameters $\boldsymbol{p}_2$; and then go back to Step 4. Otherwise stop with an error sign.

7. Approximate the cost function C as a quadratic function as $C(\alpha) = h\alpha^2 + k\alpha + l$.

8. Utilize $C(0) = C0$, $C(\alpha) = C1$ and $C(2\alpha) = C2$ to find the values of h, k and l.

9. Calculate $\alpha_{min} = -k/2h$.

Figure 4.1 shows the cost function varying with different α values. We can see the original line search is very close to a quadratic approximation over the range of interest. At A ($\alpha = 0$), B($\alpha = 4 \times 10^{-7}$) and C($\alpha = 8 \times 10^{-7}$) points, the two cost lines have intersections and these three points are used to create the quadratic shape and determine the α_{min} used in the current iteration. In theory, any three points on the $C(\alpha)$ function can determine a quadratic waveform shape. However, different points chosen from $C(\alpha)$ function will lead to a different quadratic approximation. Based on our numerical analysis,

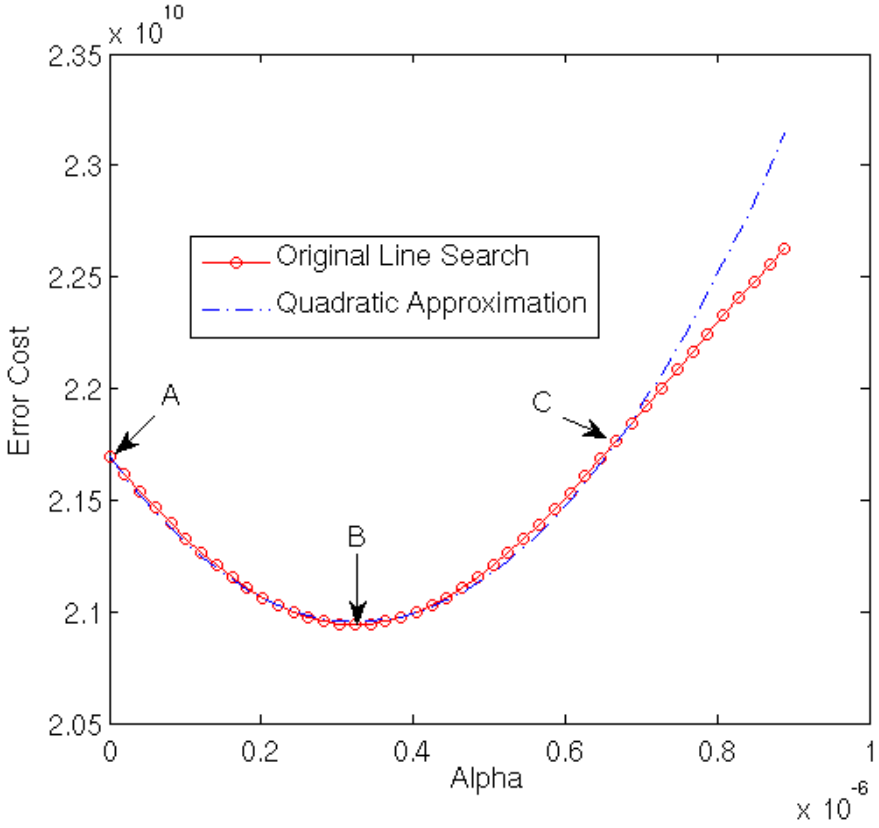

Figure 4.1: Original vs. quadratic approximation of line search

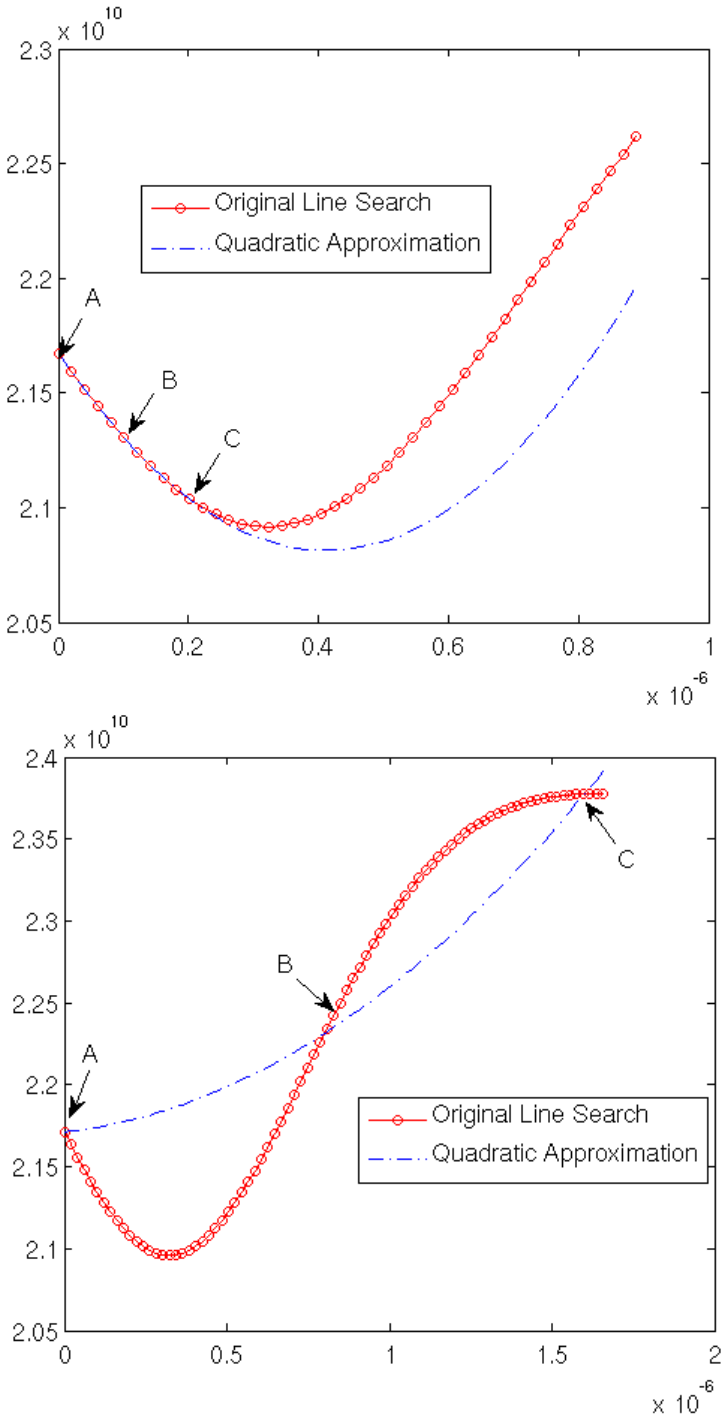

Figure 4.2: Quadratic approximation of line search based on different intersections

we notice that if C point is lower than B point and B point is lower than A point (Figure 4.2, upper plot), or if C point is higher than B point and B point is higher than A point (Figure 4.2, lower plot), the quadratic approximation is not that close to the original line search. Therefore, in our line search process, we change the α values to make A and C points higher than B point (try to make the B point close to the bottom of the original line search function) and then use the quadratic approximation to find the α_{min}. Furthermore, in order to make this procedure more reliable, the value of $C(\boldsymbol{p}+\alpha_{min}\Lambda\boldsymbol{p})$ will be compared to $C(\boldsymbol{p})$. If $C(\boldsymbol{p}+\alpha_{min}\Lambda\boldsymbol{p}) > C(\boldsymbol{p})$, it means the cost function along α is not quadratic-like in the current α searching range, and we need a full line search to be performed to find the minimizer.

In Chapter 2 and Chapter 3, we used the conjugate gradients algorithm as described above to reconstruct parameters from EPI acquisitions, and we found some drawbacks with this technique:

- Directly evaluating $C(\boldsymbol{p})$ in the line search is computationally intensive.
- Directly evaluating $\nabla_{\boldsymbol{p}} C(\boldsymbol{p})$ is computationally intensive.
- The speed of convergence to optimal parameters is relatively slow.

All of these problems lead to long reconstruction time. Therefore, we propose to develop an efficient parameter-fitting algorithm that approximates the exponential time function as a polynomial model and utilizes FFTs to accelerate the reconstruction procedure.

4.2 Fast Reconstruction Algorithm

Examining (4.2), (4.4), (4.6), (4.7) and (4.8), we notice that both data evaluations in the line search and gradient calculations include a $\exp[-2\pi(k_x x + k_y y)]$ term, which is very similar to the form of a Fourier Transform. The reason we can not directly use FFTs in these equations is the exponential time function $\exp(-\boldsymbol{d} + j\boldsymbol{\omega})t_n$. Unlike conventional MRI, which samples the k-space of a static image, EPI samples the k-space of different images that are

related by this exponential time function. Therefore, if we can utilize some approximations in the reconstruction model and replace the direct calculation of $\exp[-2\pi(k_x x + k_y y)]$ by FFTs, the iteration process should accelerate.

4.2.1 Reconstruction Model Directly Utilizing FFTs

In the previous chapters, we presented several acquisition methods for MRSI. All of them utilized EPI to shorten the acquisition duration. Echo-time selection methods use standard EPI, and the observed data is uniformly sampled in k-space while nonuniformly in the time domain. For k-t selection, a modified EPI technique is used and the observed data is only uniformly sampled in k_x direction while nonuniformly sampled in the (k_y, t) domain. In addition, no matter which EPI techniques we use, the data acquisition in the k_x direction is very fast. For instance, in the phantom experiment of Chapter 2, the time needed to acquire a single k_x line is only 0.5 ms. Therefore, in order to speed up the reconstruction process, we can ignore the time difference among the data in the same k_x line and use FFTs directly in the k_x direction.

The standard discrete observation model of MRSI from echo-planar imaging can be represented as

$$s(t_n) = \sum_x \sum_y \sum_{i=1}^{M} a_i(x,y) \exp\{[-d_i(x,y) + j\omega_i(x,y)]t_n\} \exp\{-j2\pi[k_x(t_n)x + k_y(t_n)y]\} \tag{4.12}$$

After FFTs in the k_x direction, the data used for reconstruction is given by

$$s(x_k, t_n) = \sum_y \sum_{i=1}^{M} a_i(x_k,y) \exp\{[-d_i(x_k,y) + j\omega_i(x_k,y)]t_n\} \exp[-j2\pi k_y(t_n)y] \tag{4.13}$$

In consequence, when we use the same iterative conjugate-gradient idea mentioned in the first section, the parameter gradients (4.5), (4.5) and (4.8) can be updated as

$$\frac{\partial C}{\partial \boldsymbol{a}} = 2\mathrm{Re}\left\{\sum_{t_n} e^{(-\boldsymbol{d}+j\boldsymbol{\omega})t_n} e^{-j2\pi k_y(t_n)y} f_{t_n}\right\} \tag{4.14}$$

$$\frac{\partial C}{\partial \boldsymbol{d}} = 2\mathrm{Re}\left\{\sum_{t_n} \boldsymbol{a} e^{(-\boldsymbol{d}+j\boldsymbol{\omega})t_n} \times (-t_n) \times e^{-j2\pi k_y(t_n)y} f_{t_n}\right\} \tag{4.15}$$

$$\frac{\partial C}{\partial \boldsymbol{\omega}} = 2\mathrm{Re}\left\{\sum_{t_n} \boldsymbol{a} e^{(-\boldsymbol{d}+j\boldsymbol{\omega})t_n} \times (jt_n) \times e^{-j2\pi k_y(t_n)y} f_{t_n}\right\} \tag{4.16}$$

Notice here, the reconstruction problem becomes parameter fitting at one x location (x_k), which means we need to repeat this iterative process at every x location. The parameters $\boldsymbol{a}$, $\boldsymbol{b}$ and $\boldsymbol{\omega}$ have no information in the x direction; they only vary with y location and different resonance i. After the whole iterative process, we combine the parameter set for each x location to get the full parameter package. Even though we need to repeat the iterative process at each (x) location, the calculation time still decreases significantly. This is because, during each iteration, the sizes of calculation matrices in (4.13), (4.14), (4.15) and (4.16) shrink considerably, which is the main factor contributing to computational complexity.

Recall that echo-time selection used overlapped EPI, the data acquisition for one k-space is relative fast and the k-space data is observed uniformly. So we may further accelerate the reconstruction process by using FFTs in both k_x and k_y domains. Consequently, the reconstruction problem becomes parameter fitting at each (x, y) location. The parameter gradients (4.5), (4.5) and (4.8) can be updated as

$$\frac{\partial C}{\partial \boldsymbol{a}} = 2\mathrm{Re}\left\{\sum_{t_n} e^{(-\boldsymbol{d}+j\boldsymbol{\omega})t_n} f_{t_n}\right\} \tag{4.17}$$

$$\frac{\partial C}{\partial \boldsymbol{d}} = 2\mathrm{Re}\left\{\sum_{t_n} \boldsymbol{a} e^{(-\boldsymbol{d}+j\boldsymbol{\omega})t_n} \times (-t_n) \times f_{t_n}\right\} \tag{4.18}$$

$$\frac{\partial C}{\partial \boldsymbol{\omega}} = 2\mathrm{Re}\left\{\sum_{t_n} \boldsymbol{a} e^{(-\boldsymbol{d}+j\boldsymbol{\omega})t_n} \times (jt_n) \times f_{t_n}\right\} \tag{4.19}$$

and $s(t_n) = \sum_{i=1}^{M} a_i \exp\{[-d_i + j\omega_i]t_n\}$ used in line search calculations. The parameters $\boldsymbol{a}$, $\boldsymbol{b}$ and $\boldsymbol{\omega}$ have no information in the (x, y) direction; they only vary with different resonance i. To get the full parameter package, we need to repeat the iterative process at every (x, y) location.

Sometimes, because the values of resonant frequency and decay rate are very large, even if the time difference are very small, the local decay and phase difference are still big. Therefore, ignoring the time differences in k-space may not be accurate enough, and we need to find a more accurate way to approximate the reconstruction model.

4.2.2 Reconstruction model based on polynomial approximations

As we discussed in the previous sections, because of the exponential time function $\exp(-\boldsymbol{d} + j\boldsymbol{\omega})t_n$, directly using FFTs in the gradient calculation and data evaluation in line search is sometimes not accurate enough. If we can separate the time variable t_n from decay rate $\boldsymbol{d}$ and resonant frequency $\boldsymbol{\omega}$, then a combination of FFTs can be used to speed up the reconstruction process.

Tang and Reeves [25] proposed a polynomial approximation to separate desired image parameters and time in the exponential function. However, this method is limited to functional MRI with the SS-PARSE technique (Single-shot parameter assessment by retrieval from signal encoding). Unlike MRSI, functional MRI only includes one k-space image and only cares about one resonant frequency from water. Therefore, based on their methods, we develop a more general approximation algorithm for MRSI, which can accommodate more k-space images and more resonances.

The common polynomial approximation of the exponential function is a Taylor series as shown below:

$$e^{pt} = \sum_{n=0}^{\infty} \frac{(pt)^n}{n!} \tag{4.20}$$

However, in order to get an acceptable approximation result, the number of the polynomial terms must be very large. Although we can separate the p and t, we still need to calculate FFTs many times, which means the Taylor approximation does not solve the problem of computational complexity.

In the EPI technique, the acquisition time needed for one k-space image is relatively short (dozens of microseconds level). It is reasonable to assume that the $\exp[(-\boldsymbol{d} + j\boldsymbol{\omega})t]$ term is bounded within a limited small range. Here t represents the time points within one k-space frame. Based on this assumption, one can approximate the exponential function with limited polynomials and find the coefficients in a least squares sense. Equation (4.20) can be updated as

$$e^{pt} = c_L p^L t^L + c_{L-1} p^{L-1} t^{L-1} + \ldots + c_1 pt + c_0 \tag{4.21}$$

where c_i is the polynomial coefficient for ascending powers and these coefficients are fixed through the whole reconstruction process, not varying with time. The coefficients we look for need to provide a good approximation for a range of pt values, not just a single pt value. In other words, within a bounded range, no matter how p or t changes, each $\exp(pt)$ must be expressed with the same set of polynomial coefficients. The coefficient estimation process can be written in matrix form, if the length of vector $\boldsymbol{pt}$ is N

$$argmin_{\boldsymbol{c}} \left\| e^{\boldsymbol{pt}} - \boldsymbol{PT}\boldsymbol{c} \right\|^2 \tag{4.22}$$

where

$$\boldsymbol{PT} = \begin{pmatrix} (pt_1)^0 & (pt_1)^1 & (pt_1)^2 & \cdots & (pt_1)^L \\ (pt_2)^0 & (pt_2)^1 & (pt_2)^2 & \cdots & (pt_2)^L \\ \vdots & \vdots & \vdots & \vdots & \vdots \\ (pt_N)^0 & (pt_N)^1 & (pt_N)^2 & \cdots & (pt_N)^L \end{pmatrix} \tag{4.23}$$

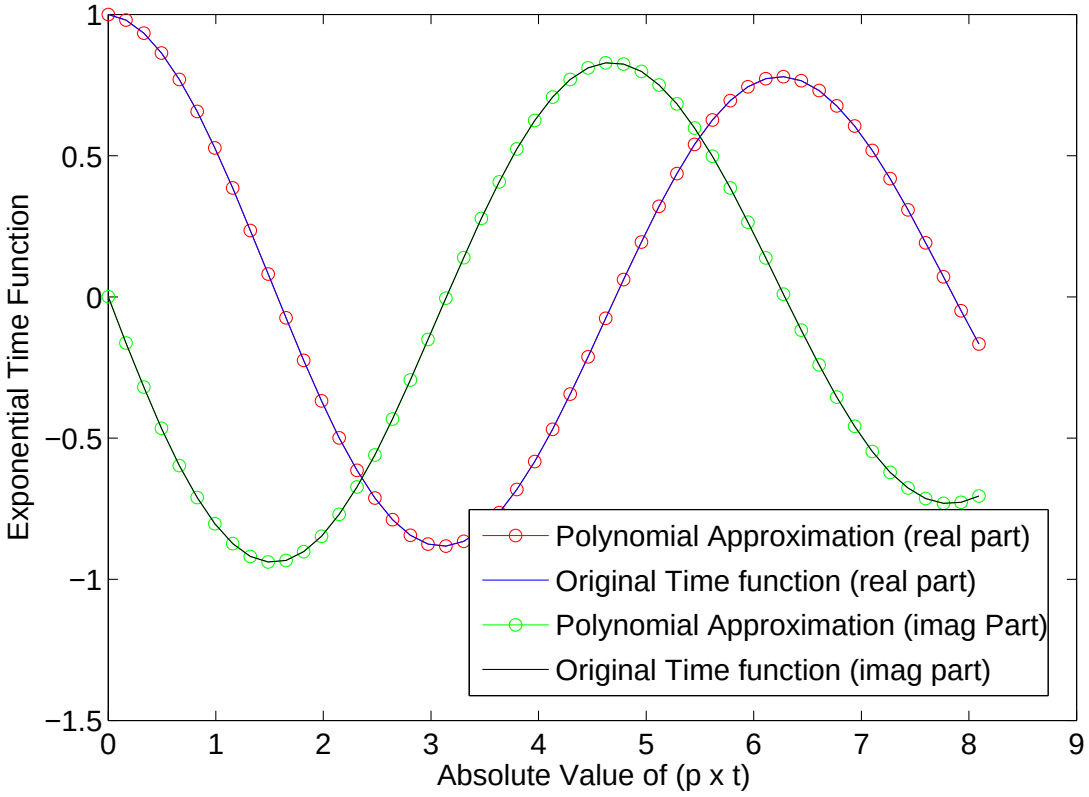

Figure 4.3: Original exponential function vs. polynomial approximation

Figure 4.3 shows the precision of the polynomial approximation (order 17) for the exponential time function $\exp(pt)$, where $\mathrm{Re}(p)$ varies within $[-10, 0]$, $\mathrm{Im}(p)$ varies within $[-80\pi, 0]$ and t varies within $[0, 0.033]$.

Figure 4.4 shows the mean squared error (MSE) between the original exponential function (e^{pt}, where $p = -10 + j80\pi$ and $t \in [0.0.033]$) and the polynomial approximation varying with the polynomial orders.

$$MSE_L = \sum_t \left| e^{pt} - \sum_{l=0}^{L} c_l p^l t^l \right|^2$$

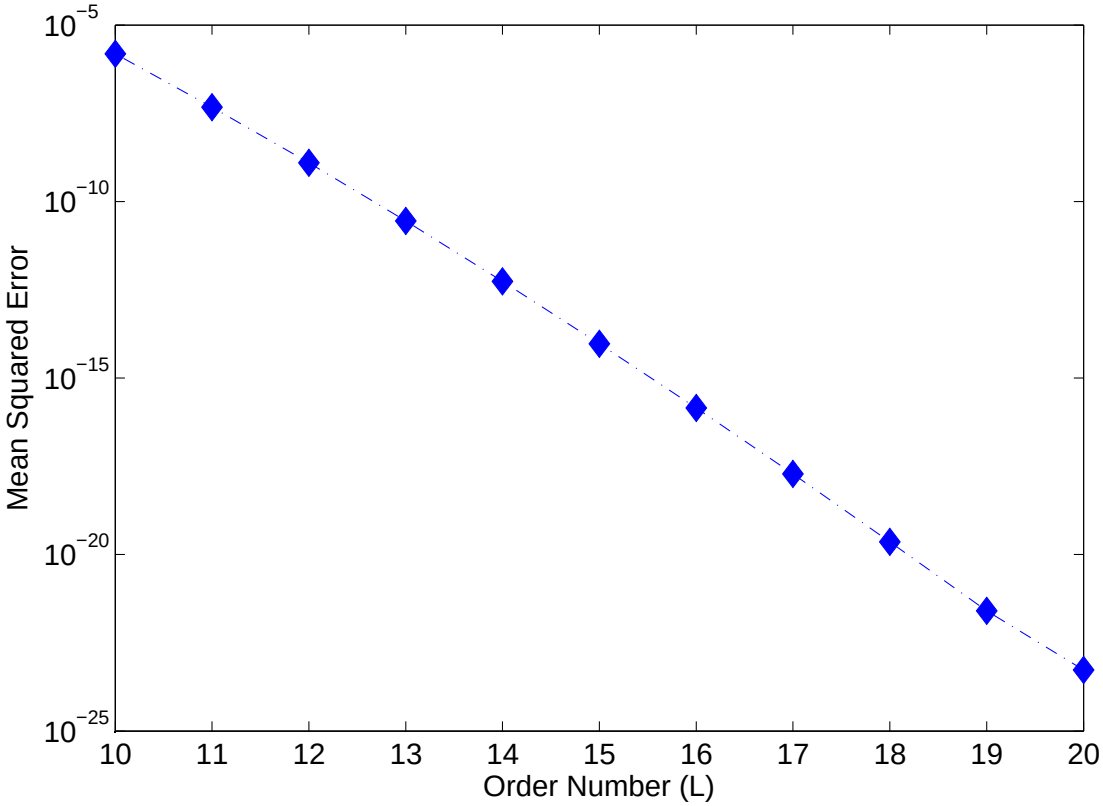

Figure 4.4: Absolute error varies with polynomial order

Apply the polynomial approximation to our exponential term $\exp[(-d(x,y)+j\omega(x,y))t_n]$

$$\begin{aligned} e^{[-d(x,y)+j\omega(x,y)]t_n} &= e^{[-d(x,y)+j\omega_0+j\omega_1(x,y)]t_n} \\ &= e^{j\omega_0 t_n} e^{[-d(x,y)+j\omega_1(x,y)]t_n} \\ &= e^{j\omega_0 t_n} e^{[-d(x,y)+j\omega_1(x,y)]TE_m} e^{[-d(x,y)+j\omega_1(x,y)](t_n-TE_m)} \\ &= e^{j\omega_0 t_n} e^{[-d(x,y)+j\omega_1(x,y)]TE_m} \sum_l c_l[-d(x,y)+j\omega_1(x,y)]^l (t_n-TE_m)^l \quad (4.24) \end{aligned}$$

where TE_m is the echo-time (the time center) of the m_{th} EPI frame. In this approximation, we make $\omega(x,y) = \omega_0 + \omega_1(x,y)$ and ω_0 does not vary with spatial location (x,y). In our research, we assume that we know what kinds of resonances exist in our subject, so we can start our evaluation with the ideal resonant frequency of that resonance. For example, if we know the resonance is water, ω_0 here is equal to 0 Hz. Even if some spatial have no water resonance, we still let $\omega_0 = 0$ everywhere while the magnitude of water resonance at these locations is 0. The term $\omega_1(x,y)$, which is caused by field inhomogeneity and noise, can vary at different spatial locations. If there is more than one resonance in one voxel, there is a different ideal resonant frequency ω_{0i} for each resonance. And let $p_i(x,y) = -d_i(x,y) + j\omega_{1i}(x,y)$ for each resonance, the observed MRSI data (4.12) can be represented as

$$\begin{aligned} s(t_m) &= \sum_x \sum_y \sum_i a_i(x,y) e^{jw_{0i}t_m} e^{p_i(x,y)t_m} e^{-j2\pi[k_x(t_m)x+k_y(t_m)y]} \\ &= \sum_x \sum_y \sum_i a_i(x,y) e^{jw_{0i}t_m} e^{p_i(x,y)TE_m} e^{p_i(x,y)(t_m-TE_m)} e^{-j2\pi[k_x(t_m)x+k_y(t_m)y]} \\ &= \sum_x \sum_y \sum_i a_i(x,y) e^{jw_{0i}t_m} e^{p_i(x,y)TE_m} \sum_l c_l p_i^l(x,y)(t_m-TE_m)^l e^{-j2\pi[k_x(t_m)x+k_y(t_m)y]} \end{aligned} \quad (4.25)$$

$$= \sum_i e^{jw_{0i}t_m} \sum_l c_l (t_m-TE_m)^l \sum_x \sum_y a_i(x,y) e^{p_i(x,y)TE_m} p_i^l(x,y) e^{-j2\pi[k_x(t_m)x+k_y(t_m)y]} \quad (4.26)$$

where t_m presents the time point in the m^{th} k-space frame. If one wants to approximate the observed data in the $(m+1)^{th}$ k-space image, echo-time value TE needs to be changed to TE_{m+1}. On the other hand, for observed data at different k-space frames, we still only need to do a polynomial approximation once to get a set of c_l. This is because for different m values, the time variance $(t_m - TE_m)$ is bounded within the same small range (as in Chapter 2 phantom experiment, this time range is [-16ms 16ms]). In consequence, $\exp[p_i(x,y)(t_m - TE_m]$ can be approximated by the same set of c_l. Similarly, for observed data of different resonance i, the same set of c_l are used. The reason is the value of $(t_m - TE_m)$ is very small (dozens of microseconds level), even though the $p_i(x,y)$ varies with i ($p_i(x,y) = -d_i(x,y) + j\omega_{1i}(x,y)$ and nomally $d_i(x,y)$ is no larger than 50 and $|\omega_{1i}(x,y)|$ is no larger than 150π), the multiplication of $[p_i(x,y) \times (t_m - TE_m)]$ is still bounded within a limited small range.

Let $B_{il-m}(x,y) = a_i(x,y)e^{p_i(x,y)TE_m}p_i^l(x,y)$. Then (4.26) can be simplified as

$$s(t_m) = \sum_i e^{jw_{0i}t_m} \sum_l c_l(t_m - TE_m)^l \sum_x \sum_y B_{il-m}(x,y)e^{-j2\pi[k_x(t_m)x + k_y(t_m)y]} \tag{4.27}$$

We can calculate the inside term $\sum_x \sum_y B_{il-m}(x,y)e^{j[k_x(t_m)x+k_y(t_m)y]}$ of (4.27) with a 2D FFT, and the observed data $s(t_m)$ can be approximated with a linear combination of a relatively small number of FFTs.

$$s(t_m) = \sum_i e^{jw_{0i}t_m} \sum_l c_l(t_m - TE_m)^l \tilde{B}_{il-m}[\underline{\mathbf{k}}(t_m)] \tag{4.28}$$

where $\tilde{B}_{il-m}[\underline{\mathbf{k}}(t_m)]$ is the Fourier transforms of $B_{il-m}(x,y)$. Similarly, for the gradient calculation (4.9), (4.10) and (4.11) can be approximated as

$$\begin{aligned}\frac{\partial C}{\partial a_i(x,y)} &= 2\mathrm{Re}\left\{\sum_t e^{[-d_i(x,y)+j\omega_i(x,y)]t}e^{-j2\pi[k_x(t)x+k_y(t)y]}f_t\right\} \\ &= 2\mathrm{Re}\left\{\sum_m \sum_{t_m} e^{j\omega_{0i}t_m}e^{p_i(x,y)t_m}e^{-j2\pi[k_x(t_m)x+k_y(t_m)y]}f_{t_m}\right\}\end{aligned}$$

Here $\sum_{t_m}$ represents adding all observed time points in the m^{th} k-space frame, while $\sum_m$ represents adding all observed k-space frames.

$$\begin{aligned}
&\frac{\partial C}{\partial a_i(x,y)} \\
&= 2\mathrm{Re}\left\{\sum_m\sum_{t_m} e^{j\omega_{0i}t_m}e^{p_i(x,y)TE_m}e^{p_i(x,y)(t_m-TE_m)}e^{-j2\pi[k_x(t_m)x+k_y(t_m)y]}f_{t_m}\right\} \\
&= 2\mathrm{Re}\left\{\sum_m\sum_{t_m} e^{j\omega_{0i}t_m}e^{p_i(x,y)TE_m}\sum_l c_l p_i(x,y)^l(t_m-TE_m)^l e^{-j2\pi[k_x(t_m)x+k_y(t_m)y]}f_{t_m}\right\} \\
&= 2\mathrm{Re}\left\{\sum_l c_l p_i(x,y)^l\sum_m e^{p_i(x,y)TE_m}\sum_{t_m} e^{j\omega_{0i}t_m}(t_m-TE_m)^l e^{-j2\pi[k_x(t_m)x+k_y(t_m)y]}f_{t_m}\right\}
\end{aligned} \tag{4.29}$$

$$\begin{aligned}
&\frac{\partial C}{\partial d_i(x,y)} \\
&= 2\mathrm{Re}\left\{a_i(x,y)\sum_l c_l p_i(x,y)^l\sum_m e^{p_i(x,y)TE_m}\sum_{t_m} e^{j\omega_{0i}t_m}(t_m-TE_m)^l e^{-j2\pi[k_x(t_m)x+k_y(t_m)y]}(-t_m)f_{t_m}\right\}
\end{aligned} \tag{4.30}$$

$$\begin{aligned}
&\frac{\partial C}{\partial \omega_i(x,y)} \\
&= 2\mathrm{Re}\left\{a_i(x,y)\sum_l c_l p_i(x,y)^l\sum_m e^{p_i(x,y)TE_m}\sum_{t_m} e^{j\omega_{0i}t_m}(t_m-TE_m)^l e^{-j2\pi[k_x(t_m)x+k_y(t_m)y]}(jt_m)f_{t_m}\right\}
\end{aligned} \tag{4.31}$$

The inside summations $\sum_{t_m}$ of (4.29), (4.30) and (4.31) can also be evaluated by FFTs. Therefore, the gradient calculations can be approximated with a linear combination of a relatively small number of FFTs. One thing we need to pay attention to: when FFTs are utilized, uniformly sampling in k-space is required. Therefore, *k-t* selection samples may not compatible with this polynomial approximation.

In this reconstruction protocol, even though an extra polynomial approximation step is added to the reconstruction process, the utilization of the FFTs and the reduction of the matrix size in the calculations give this algorithm high potential to accelerate the reconstruction speed.

4.3 Experiment

Simulation and phantom experiments are presented in this section to validate the polynomial approximations used in the reconstruction process. Both simulation data and phantom data were acquired by the EPI technique. 500 echoes separated by 0.3788 ms were used in the EPI acquisition (from 17.81ms to 206.83ms). Utilizing SBS selection method, 48 out of 500 echo-time values were selected (48 k-space images) for the reconstruction procedure. For comparison, we used regular conjugate gradients, modified conjugate gradients (direct FFTs in k_x direction) and polynomial approximation (order number=17) to reconstruct the spatial information. There are four different resonances: hydroxyl, ethyl, methyl from methanol and methyl from ethanol. The spectral bandwidth was 2640 Hz, and spatial resolution was 2 mm$\times$2 mm with a 64$\times$ 64 matrix.

4.3.1 Simulation experiment

We evaluated the performance of different reconstruction techniques with a set of noisy simulation data. The first column of Figure 4.5 shows the true spatial distributions at different resonant frequencies (0Hz-hydroxyl, 241Hz-ethyl, 298Hz-methyl from methanol and 728Hz-methyl from ethanol). This information is used to synthesize the decaying k-space images. We added 20 dB SNR white Gaussian noise to the synthesized k-space data and reconstructed the spatial information from these noisy data. The estimated parameters ($\boldsymbol{a}$, $\boldsymbol{d}$) we started with had 30% offset from the original ones and the estimated resonant frequencies started with $\pm$5 Hz offset.

Figure 4.5 shows reconstructed spatial details at different resonant frequencies. The reconstruction results from both regular conjugate gradient methods and polynomial approximation display good agreement with the original spatial distributions.

The MSE$_{PCT}$s (mean squared errors in %) of the reconstructed parameters are listed in Table 4.1, 4.2 and 4.3.

$$MSE_{PCT} = \frac{\sum_{x,y} |p(x,y) - \hat{p}(x,y)|^2}{\sum_{x,y} |p(x,y)|^2} \times 100\%$$

Table 4.1: MSE$_{PCT}$ of reconstructed magnitude (%)

	hydroxyl	ethyl	methyl of methanol	methyl of ethanol
ordinary CG	3.72	13.73	15.90	7.56
polynomial approx	4.09	14.35	17.08	8.23
modified CG	5.36	18.89	22.49	10.25

Table 4.2: MSE$_{PCT}$ of reconstructed decay (%)

	hydroxyl	ethyl	methyl of methanol	methyl of ethanol
ordinary CG	0.86	14.90	11.63	3.48
modified CG	0.93	15.44	12.34	3.75
polynomial approx	0.98	21.57	15.45	5.63

Table 4.3: MSE$_{PCT}$ of reconstructed frequnecy (%)

	hydroxyl	ethyl	methyl of methanol	methyl of ethanol
ordinary CG	5.3957e-02	7.8051e-03	5.5608e-03	6.6698e-04
modified CG	5.5441e-02	7.8223e-03	5.7638e-03	6.6895e-04
polynomial approx	5.7344e-02	8.9078e-03	6.4547e-03	8.4903e-04

All of the reconstructions were implemented in MATLAB running on a single core of a workstation equipped with 2.4 GHz AMD Opteron 880 dual-core processors (@Xi Computer Corp). We compared their computation time for 100 iterations, shown in Table 4.4. One can see that using polynomial approximation in the reconstruction procedure, we can greatly shortens the calculation time without sacrificing the reconstruction quality. For the modified

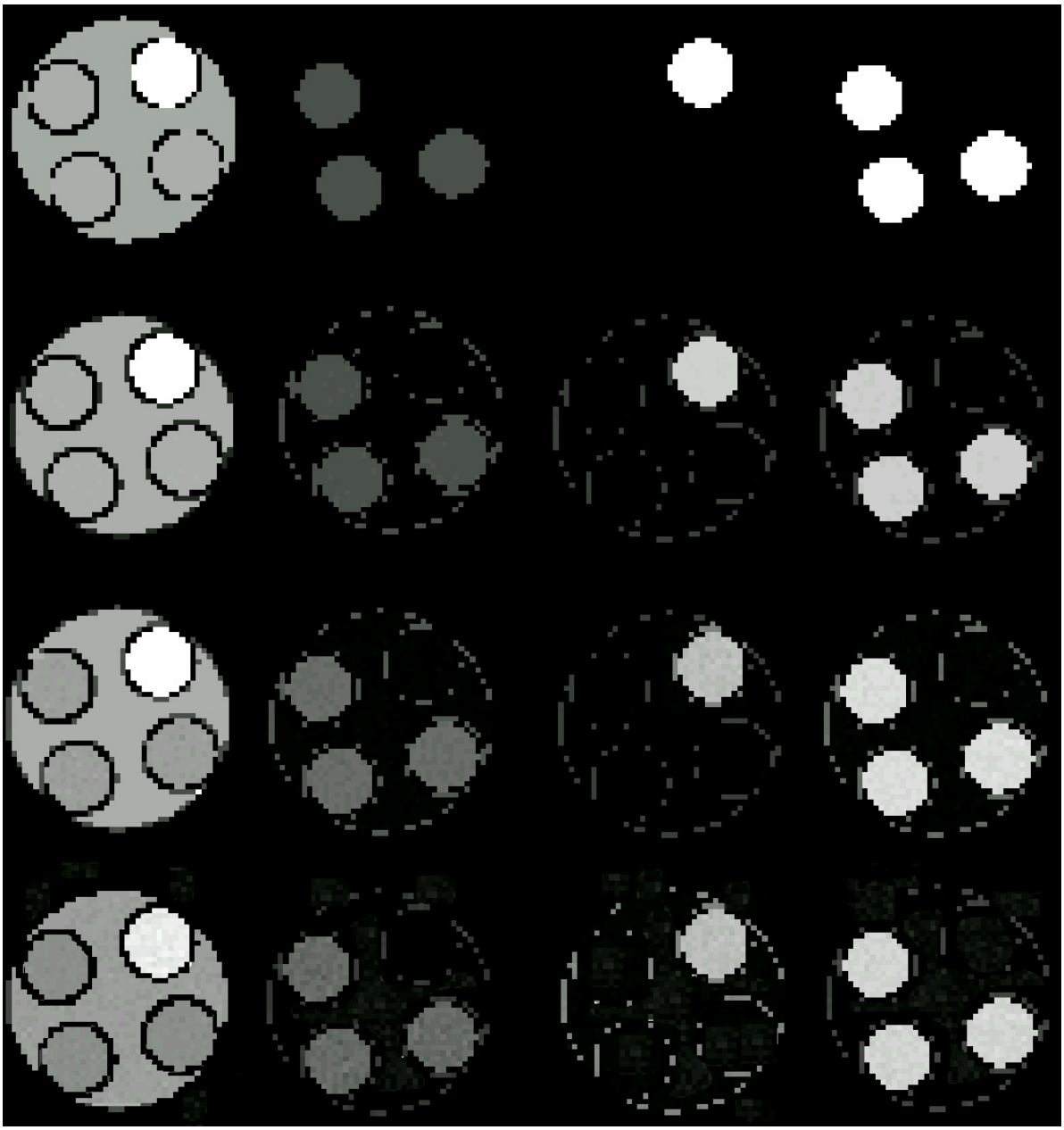

Figure 4.5: Original simulated spatial images (first row), spatial images reconstructed from 48 optimized echo-time values with regular conjugate gradient method (second row), spatial images reconstructed from 48 optimized echo-time values with polynomial approximation method (third row), spatial images reconstructed from 48 optimized echo-time values with modified conjugate gradient method (fourth row). Each column from left to right represents spatial distributions of: hydroxyl, ethyl, methyl of methanol, methyl of ethanol.

conjugate gradient method (direct FFTs in k_x direction), the reconstruction can also be accelerated and the reconstruction results are also acceptable, though not as good as the regular conjugate gradient method or polynomial approximation technique.

Table 4.4: Comparison of reconstruction time for 100 iterations (s)

ordinary CG	modified CG	polynomial approx
189.62k	16.23k	3.87k

4.3.2 Phantom Experiment

The phantom data we used to demonstrate the value of the reconstruction techniques is the same set used in Chapter 2 phantom experiment. For comparison purposes, images reconstructed from 500 echoes with the regular conjugate gradient method were treated as ground truth.

The reconstructed spatial results of the phantom experiment are compared in Figure 4.6. We observed that the images reconstructed from 48 optimized echo-time values with both the regular conjugate gradient method and polynomial approximation can distinguish different resonances very well. The reconstructed spatial distributions from these two methods yield good agreement with the ground truth. In contrast, the modified conjugate gradient method (direct FFTs in k_x direction) also held acceptable reconstruction performance but there were some small artifacts, especially in the x direction.

4.3.3 Conclusion

In this chapter, we focus on how to reduce the computational complexity to accelerate the reconstruction procedure of MRSI using the EPI technique. Sometimes, FFTs can be directly used in the reconstruction. In our case, we applied FFTs directly in the k_x domain to obtain x direction information because the acquisition time in the k_x direction is short enough to ignore. However, in many practical situations, this kind of approach may not be

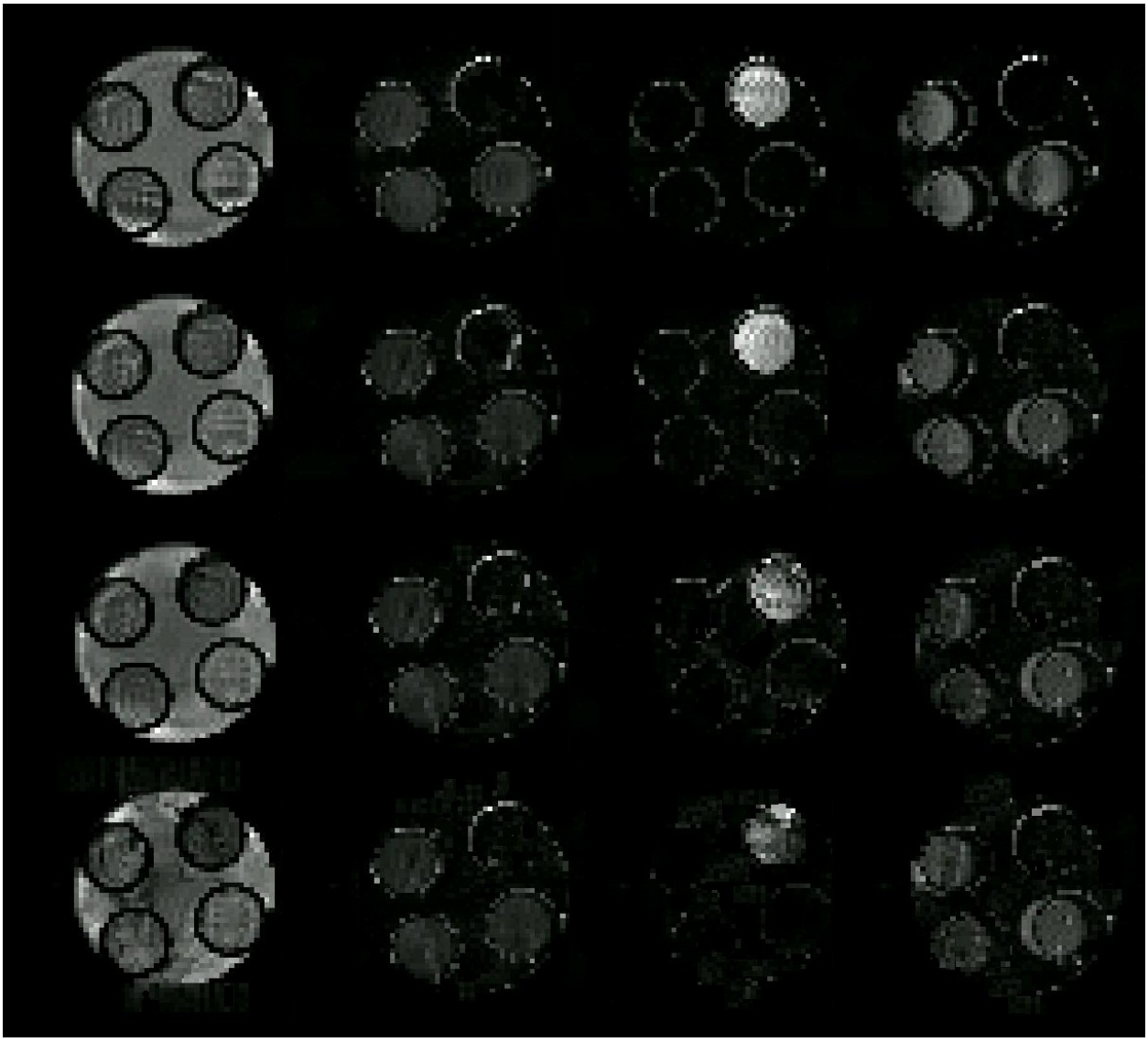

Figure 4.6: Spatial images reconstructed from full k-space data with regular conjugate gradient method (first row), spatial images reconstructed from 48 optimized echo-time values with regular conjugate gradient method (second row), spatial images reconstructed from 48 optimized echo-time values with polynomial approximation method (third row), spatial images reconstructed from 48 optimized echo-time values with modified conjugate gradient method (fourth row). Each column from left to right represents spatial distributions of: hydroxyl, ethyl, methyl of methanol, methyl of ethanol.

accurate enough and the reconstruction time is still relatively long. We present a polynomial approximation used for the time exponential function in the observed MRSI model. In this case a linear combination of FFTs can be applied to reduce the computational complexity. Simulation and phantom experiments show that this method can greatly reduce the reconstruction time, and there is no significant difference in reconstructed results compared to the regular conjugate gradient reconstruction method. However, this polynomial approximation requires the observed data to be distributed uniformly in k-space; therefore, if the data is acquired by the $k - t$ selection method, we cannot use the polynomial approach to accelerate the reconstruction process. For future work, we intend to develop a more flexible reconstruction algorithm that can accommodate more acquisition strategies and handle more parameter offsets.

Chapter 5

Optimization Techniques to Attenuate Frequency Local Minima Effect

In MRSI, many reconstruction problems can be posed as image parameter estimation from a sequence of discrete, finite measurements. Unfortunately, frequency local minima are a common practical problem when signal model-fitting procedures are implemented. Conventional, gradient-based optimization methods such as steepest descent, Newton's method and conjugate gradients are subject to frequency local minima. As a result, convergence to the global minimum is not guaranteed. What is worse, if the estimated frequency is not correct, the estimated signal amplitude and decay rate will be inaccurate.

5.1 Origins of Local Minima

Many signals used in MRSI are decaying sinusoids (cosines). Thus we only consider an exponential signal model defined by amplitude, decay rate and frequency in our work:

$$x(t) = ae^{(-d+j\omega)t} + \epsilon(t) \tag{5.1}$$

where $x(t)$ is the observed signal; a, d and ω are unknown signal parameters which need to be estimated; and $\epsilon(t)$ represents zero-mean, independent, identically distributed Gaussian noise. To understand the cause of local minima in the parameter fitting procedure, consider a simple cost function with one resonant peak in 1-D:

$$\int_0^T \left| ae^{(-d+j\omega)t} - a_0 e^{(-d_0+j\omega_0)t} \right|^2 dt \tag{5.2}$$

Here a_0, d_0 and ω_0 are original signal parameters; and T is the observed signal length. Let $\tilde{\omega} = \omega - \omega_0$ and utilize $e^{j\phi} = \cos(\phi) + j\sin(\phi)$, $\cos(\phi) = \frac{(e^{j\phi}+e^{-j\phi})}{2}$ and $\left|e^{j\phi}\right| = 1$. Then (5.2) can be updated as

$$
\begin{aligned}
&\int_0^T \left|e^{j\omega_0 t}\right| \left|ae^{-dt}e^{j\tilde{\omega}t} - a_0 e^{-d_0 t}\right|^2 dt \\
&= \int_0^T \left|ae^{-dt}(\cos\tilde{\omega}t + j\sin\tilde{\omega}t) - a_0 e^{-d_0 t}\right|^2 dt \\
&= \int_0^T \left|(ae^{-dt}\cos\tilde{\omega}t - a_0 e^{-d_0 t}) + jae^{-dt}\sin\tilde{\omega}t\right|^2 dt \\
&= \int_0^T (a^2 e^{-2dt} + a_0^2 e^{-2d_0 t})dt - \int_0^T 2aa_0 e^{-(d+d_0)t} cos\tilde{\omega}t dt \qquad (5.3) \\
&= \int_0^T (a^2 e^{-2dt} + a_0^2 e^{-2d_0 t})dt - aa_0 \int_0^T e^{-(d+d_0)t}e^{-j\tilde{\omega}t}dt - aa_0 \int_0^T e^{-(d+d_0)t}e^{j\tilde{\omega}t}dt \qquad (5.4)
\end{aligned}
$$

We notice that the second and third terms of (5.4) are very similar to the form of a Fourier transform. However, in practice, T must be a finite value (none of the observed signals could be infinite length). In order to take advantage of the Fourier transform relationship, we extend the range of integration from $(0, T)$ to $(-\infty, \infty)$ while adding a window function to the original expression. Therefore, (5.4) is modified as

$$
\begin{aligned}
&\frac{{a_0}^2}{-2d_0}(e^{-2d_0 T} - 1) + \frac{a^2}{-2d}(e^{-2dT} - 1) - aa_0 \int_{-\infty}^{\infty} e^{-(d+d_0)t}u(t)[u(t) - u(t-T)]e^{-j\tilde{\omega}t}dt \\
&- aa_0 \int_{-\infty}^{\infty} e^{-(d+d_0)t}u(t)[u(t) - u(t-T)]e^{j\tilde{\omega}t}dt \qquad (5.5)
\end{aligned}
$$

Now, the third term of (5.5) is the Fourier transform of $e^{-(d+d_0)t}u(t)[u(t) - u(t-T)]$, and the fourth term of (5.5) can be treated as a conjugate component of the third term. Now we use the fact that if two functions multiply in the time domain, their Fourier transform functions will convolve in the frequency domain. The extra $u(t)$ here is used for easy Fourier transform

of the exponential term $e^{-(d+d_0)t}$, which does not change the value of this expression. Let

$$G(\tilde{\omega}) = \mathcal{F}\{[e^{-(d+d_0)t}u(t)]\} = \frac{1}{(d_0+d)+j\tilde{\omega}}$$
$$H(\tilde{\omega}) = \mathcal{F}\{[u(t)-u(t-T)]\} = T\text{sinc}(\frac{\tilde{\omega}T}{2}) \times e^{\frac{-j\tilde{\omega}T}{2}}$$

Then (5.5) will become

$$\begin{aligned}
&\frac{{a_0}^2}{-2d_0}(e^{-2d_0T}-1) + \frac{a^2}{-2d}(e^{-2dT}-1) - aa_0 \times \{G(\tilde{\omega}) * H(\tilde{\omega}) + [G(\tilde{\omega}) * H(\tilde{\omega})]^*\} \\
=&\frac{{a_0}^2}{-2d_0}(e^{-2d_0T}-1) + \frac{a^2}{-2d}(e^{-2dT}-1) - 2aa_0 \times \Re[G(\tilde{\omega}) * H(\tilde{\omega})] \\
=&\frac{{a_0}^2}{-2d_0}(e^{-2d_0T}-1) + \frac{a^2}{-2d}(e^{-2dT}-1) - 2aa_0 \times \Re\left\{[T\text{sinc}(\frac{\tilde{\omega}T}{2}) \times e^{\frac{-j\tilde{\omega}T}{2}}] * \frac{1}{(d_0+d)+j\tilde{\omega}}\right\}
\end{aligned} \tag{5.6}$$

Examining (5.6), the first term is a fixed value based on the original signal parameters; the second term varies with estimated magnitude and decay does not oscillate; and the third term including $\text{sinc}(\frac{\tilde{\omega}T}{2})$ has obvious local minima. Since the $\text{sinc}(\frac{\tilde{\omega}T}{2})$ shape originates from the window function, the reason for local minima is the finite signal observations. Figure 5.1 shows the cost function as it varies with different parameter offsets.

If there are only magnitude offset and decay offset, the cost function is non-oscillatory (Figure 5.1, lower plot). If frequency offset presents, local minima appear in the cost function (Figure 5.1, upper and middle plots). In practice, many signals in MRSI have more than one resonant peaks. In these cases, the general cost function is a combination of several oscillating functions and local minima still exist. For instance, if there are two resonant peaks, the cost function becomes

$$\int_0^T \left| \sum_{i=1,2} a_i e^{(-d_i+j\omega_i)t} - \sum_{i=1,2} a_{0i} e^{(-d_{0i}+j\omega_{0i})t} \right|^2 dt \tag{5.7}$$

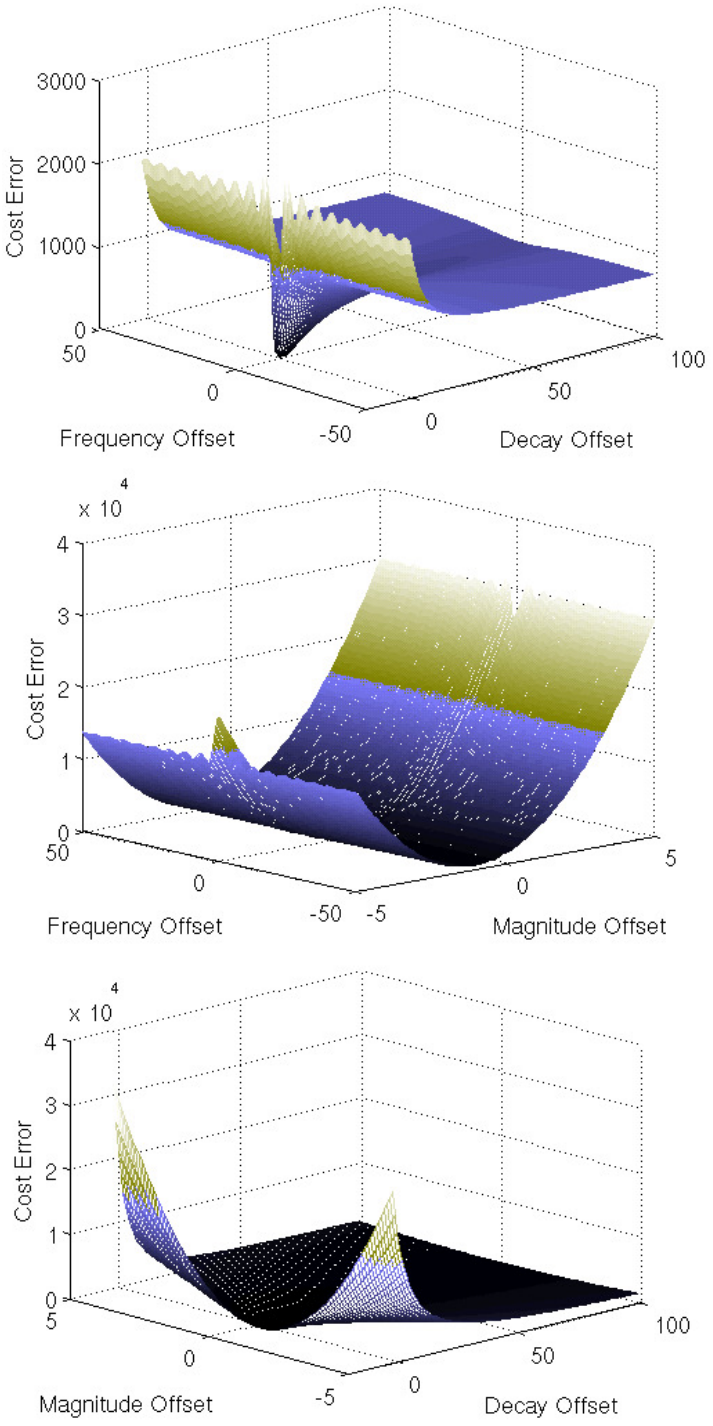

Figure 5.1: Cost function varying with frequency and decay offsets (upper plot) frequency and magnitude offsets (middle plot) magnitude and decay offsets (lower plot)

After expansion, (5.7) updates as

$$
\begin{aligned}
&\int_0^T \left|a_1 e^{-d_1 t}\cos\omega_1 t + a_2 e^{-d_2 t}\cos\omega_2 t - a_{01} e^{-d_{01} t}\cos\omega_{01} t - a_{02} e^{-d_{02} t}\cos\omega_{02} t\right|^2 dt \\
&+ \int_0^T \left|a_1 e^{-d_1 t}\sin\omega_1 t + a_2 e^{-d_2 t}\sin\omega_2 t - a_{01} e^{-d_{01} t}\sin\omega_{01} t - a_{02} e^{-d_{02} t}\sin\omega_{02} t\right|^2 dt \\
&= \int_0^T ({a_1}^2 e^{-2d_1 t} + {a_2}^2 e^{-2d_2 t} + {a_{01}}^2 e^{-2d_{01} t} + {a_{02}}^2 e^{-2d_{02} t}) dt \\
&+ 2a_1 a_2 \int_0^T e^{(-d_1 - d_2)t}(\cos\omega_1 t\cos\omega_2 t + \sin\omega_1 t\sin\omega_2 t) dt \\
&+ 2a_{01} a_{02} \int_0^T e^{(-d_{01} - d_{02})t}(\cos\omega_{01} t\cos\omega_{02} t + \sin\omega_{01} t\sin\omega_{02} t) dt \\
&- 2a_1 a_{01} \int_0^T e^{(-d_1 - d_{01})t}(\cos\omega_1 t\cos\omega_{01} t + \sin\omega_1 t\sin\omega_{01} t) dt \\
&- 2a_1 a_{02} \int_0^T e^{(-d_1 - d_{02})t}(\cos\omega_1 t\cos\omega_{02} t + \sin\omega_1 t\sin\omega_{02} t) dt \\
&- 2a_2 a_{01} \int_0^T e^{(-d_2 - d_{01})t}(\cos\omega_2 t\cos\omega_{01} t + \sin\omega_2 t\sin\omega_{01} t) dt \\
&- 2a_2 a_{02} \int_0^T e^{(-d_2 - d_{02})t}(\cos\omega_2 t\cos\omega_{02} t + \sin\omega_2 t\sin\omega_{02} t) dt
\end{aligned} \tag{5.8}
$$

Utilizing the sum and difference formulas of sin / cos

$$\cos\omega_1 t\cos\omega_2 t + \sin\omega_1 t\sin\omega_2 t = \cos(\omega_1 - \omega_2)t$$

(5.8) becomes as

$$
\begin{aligned}
&\int_0^T ({a_1}^2 e^{-2d_1 t} + {a_2}^2 e^{-2d_2 t} + {a_{01}}^2 e^{-2d_{01} t} + {a_{02}}^2 e^{-2d_{02} t}) dt \\
&+ \int_0^T [2a_1 a_2 e^{(-d_1 - d_2)t}\cos(\omega_1 - \omega_2)t + 2a_{01} a_{02} e^{(-d_{01} - d_{02})t}\cos(\omega_{01} - \omega_{02})t] dt \\
&- \int_0^T [2a_1 a_{01} e^{(-d_1 - d_{01})t}\cos(\omega_1 - \omega_{01})t + 2a_1 a_{02} e^{(-d_1 - d_{02})t}\cos(\omega_1 - \omega_{02})t] dt \\
&- \int_0^T [2a_2 a_{01} e^{(-d_2 - d_{01})t}\cos(\omega_2 - \omega_{01})t + 2a_2 a_{02} e^{(-d_2 - d_{02})t}\cos(\omega_2 - \omega_{02})t] dt
\end{aligned} \tag{5.9}
$$

Normally, multi-resonant peaks in one MRSI signal have almost the same frequency offset, which means $\omega_1 - \omega_{01} = \omega_2 - \omega_{02} = \tilde{\omega}$, and $\omega_{01} - \omega_{02} = \omega$ is known before observation. Therefore, (5.9) can be simplified as

$$\begin{aligned}
&\int_0^T ({a_1}^2 e^{-2d_1 t} + {a_2}^2 e^{-2d_2 t} + {a_{01}}^2 e^{-2d_{01} t} + {a_{02}}^2 e^{-2d_{02} t}) dt \\
&+ \int_0^T [2a_1 a_2 e^{(-d_1 - d_2)t} + 2a_{01} a_{02} e^{(-d_{01} - d_{02})t}] \cos(\omega) t dt \\
&- \int_0^T [2a_1 a_{01} e^{(-d_1 - d_{01})t} + 2a_2 a_{02} e^{(-d_2 - d_{02})t}] \cos(\tilde{\omega}) t dt \\
&- \int_0^T 2A_1 A_{02} e^{(-d_2 - d_{01})t} \cos(\tilde{\omega} + \omega) t dt - \int_0^T 2A_2 A_{01} e^{(-d_2 - d_{01})t} \cos(\tilde{\omega} - \omega) t dt
\end{aligned} \tag{5.10}$$

Comparing (5.3) and (5.10), one can see that only the last three items including frequency offset($\cos\tilde{\omega}t$, $\cos(\tilde{\omega} + \omega)t$ and $\cos(\tilde{\omega} - \omega)t$) are the reasons for the oscillatory shape of the cost function. And the oscillating frequencies are all related to $\tilde{\omega}$, $\tilde{\omega} + \omega$ and $\tilde{\omega} - \omega$.

5.2 Optimization Protocol with Varying Decay

In the previous section, we know that local minima come from the finite signal observations (here, we focus on the case of one resonant peak), which is represented as the third term of (5.6). The estimated magnitude a is just a scalar in the third term of (5.6); it will not increase or decrease the number of local minima. Therefore, if we can decrease the oscillation from $\left\{[T\text{sinc}(\frac{\tilde{\omega}T}{2}) \times e^{\frac{-j\tilde{\omega}T}{2}}] * \frac{1}{(d_0+d)+j\tilde{\omega}}\right\}$, the local minima effect can be attenuated.

5.2.1 Theory

Considering the various sectional views of Figure 5.1a and b, we can see that increasing the estimated a value does not change the shape of the cost function (Figure 5.2a), while increasing the estimated d value can spread out the main lobe of the cost function, and the local minima fade away. In the middle plot of Figure 5.2b, even though there are some local minima remaining, the main lobe that includes the global minimum is expanded. That

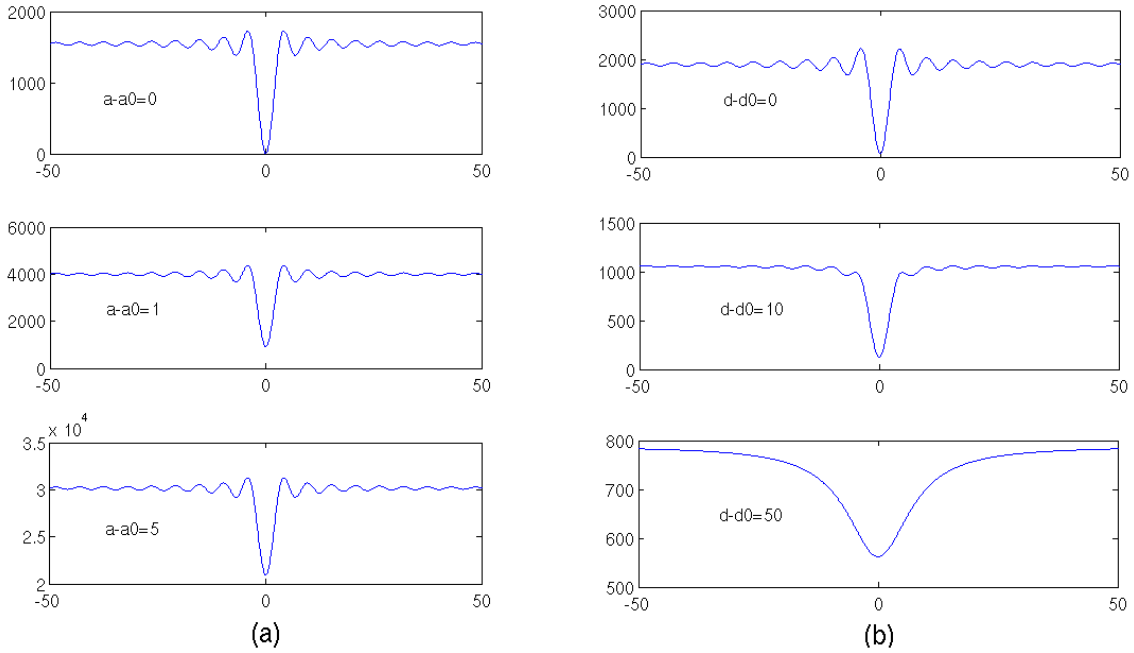

Figure 5.2: Cost function varying with frequency at (a) different magnitude offsets (b) different decay offsets

means the potential of finding the global minimum is enhanced. On the other hand, when the decay rate decreases, the gradient of the main lobe becomes sharper, yielding faster convergence and more accurate estimates [12].

As a result, in order to converge to the global optimum accurately and efficiently, the following procedure is used. The initial estimated decay d is set large to widen the main lobe to ensure that the frequency offset value is inside the main lobe. Then conjugate gradient (GC) is used to modify the frequency parameters. Next, we decrease the decay value and repeat CG. The procedure becomes a narrower search, so that the global optimum is estimated more accurately. In addition, decreasing the decay value through iterations will also accelerate the convergence speed. In consequence, an accurate global optimum can be detected within a limited number of iterations. Here we need to be alert that in each

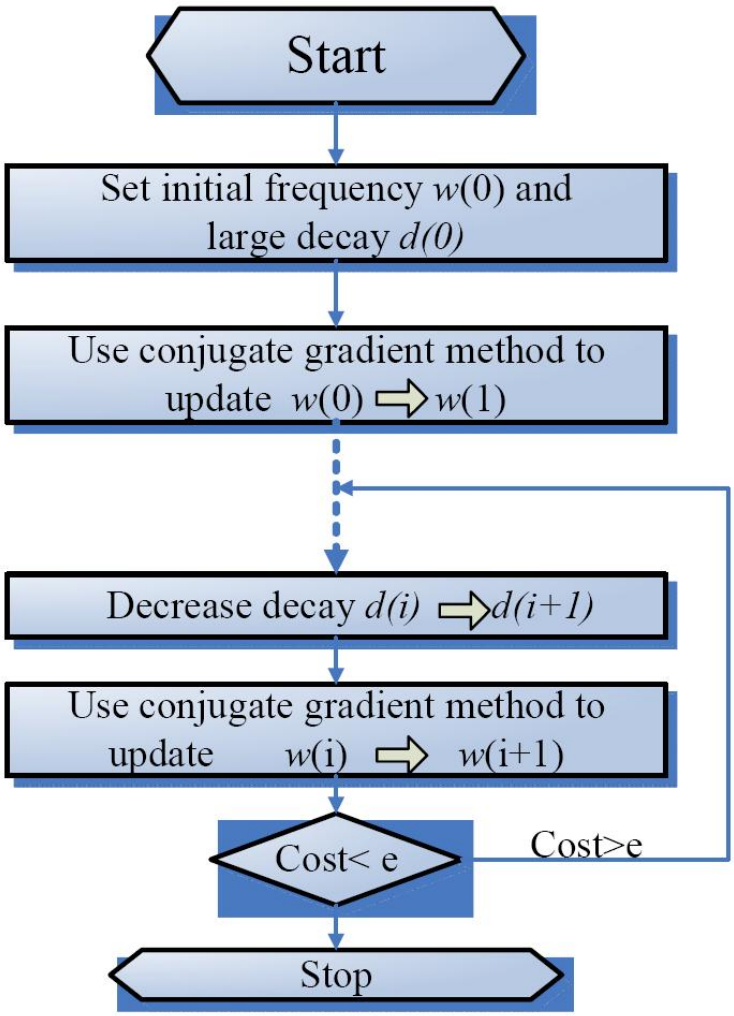

Figure 5.3: Overview of the proposed method

iteration step, the frequency offset is always required to be inside the main lobe. Figure 5.3 shows an overview of the proposed method.

5.2.2 Experiments and Results

To investigate the validity of the proposed method, three simulation experiments are presented. To focus on frequency local minima, we assume the signal magnitudes in the following experiments are one.

- Experiment 1: single resonant peak with uniform samples

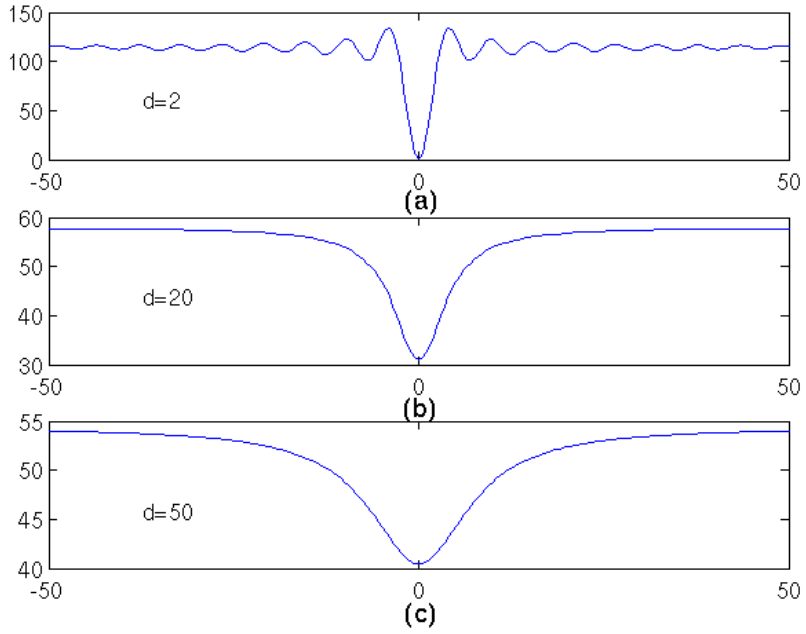

Figure 5.4: Cost function with (a) decay=-2 (b) decay=-20 (c) decay=-50

$$x(t) = e^{(-1.3+j535\pi)t} \qquad t \in (0 : 0.18) \tag{5.11}$$

The cost function is

$$C = \int_0^{0.18} \left| e^{(-d+j\omega)t} - x(t) \right|^2 \tag{5.12}$$

The observed $x(t)$ has 64 uniform samples, d is the estimated decay and ω is the estimated frequency. We explore the frequency offsets ($\frac{\omega-535}{2\pi}$) from -50 Hz to 50 Hz. Figure 5.4 compares different estimated decays applied to the cost function: $d = 2$ (upper plot), $d = 20$ (middle plot) and $d = 50$ (bottom plot).

If we initialize the estimated frequency 30 Hz away from the original: for the cost function of Figure 5.4a, the reconstructed frequency is 28.5 Hz away from the original (converging to the nearest local minimum); while for the cost function of Figure 5.4b and 5.4c, the reconstructed frequency will be almost the same as the original (achieving the global minimum).

Table 5.1 shows the acceptable frequency offset range for cost functions with different decays and compares the number of iterations required for minimum convergence. Here acceptable frequency offset range indicates the region within which there are no frequency local minima, and the number of iterations indicates the convergence speed.

Table 5.1: Comparison of offset range (Hz)and number of iterations

	Acceptable frequency offset range	Number of iterations for converging from ±30 Hz offset to a minimum
Cost function as Figure 5.4a	-4 ↔ 4	7 (Local minimum)
Cost function as Figure 5.4b	-45 ↔ 45	113 (Global minimum)
Cost function as Figure 5.4c	-45 ↔ 45	252 (Global minimum)
Varying cost function as proposed method	-45 ↔ 45	78 (Global minimum)

- Experiment 2: two resonant peaks with uniform samples

$$x(t) = e^{(-1.3+j535\pi)t} + e^{(-3+j580\pi)t} \quad t \in (0 : 0.18) \tag{5.13}$$

The observed $x(t)$ has 64 uniform samples, d_i is the estimated deacy and ω_i is the estimated frequency. We explore the frequency offsets from -50 Hz to 50 Hz. Figure 5.5 compares different estimated decays applied to the cost function: $d = 2$ (upper plot), $d = 20$ (middle plot) and $d = 50$ (bottom plot). Table 5.2 shows the acceptable frequency offset range for cost functions with different decays and compares the number of iterations required for minimum convergence.

- Experiment 3: one resonant peak with nonuniform samples

Uniformly sampled signals were investigated in the previous two experiments, now we execute another experiment using the following signal, and the measured signal is selected

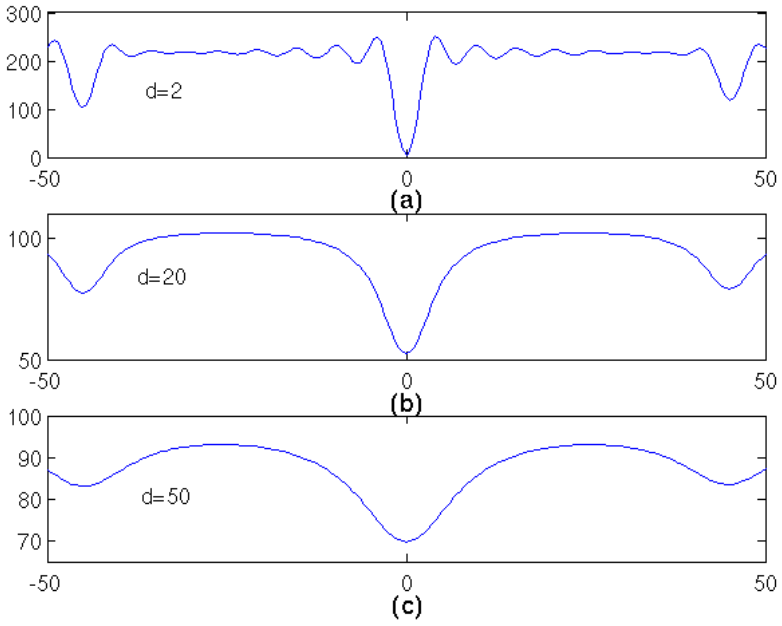

Figure 5.5: Cost function with (a) decay=-2 (b) decay=-20 (c) decay=-50

nonuniformly (64 samples) within $(0, 0.18)$:

$$x(t) = e^{(-1.3+j535\pi)t} \tag{5.14}$$

We explore the frequency offsets from -50Hz to 50Hz. Figure 5.6 compares different estimated decays applied to the cost function: $d_i = 2$ (upper plot), $d_i = 20$ (middle plot), $d_i = 50$ (bottom plot). Table 5.3 shows the acceptable frequency offset range for cost functions with different decays and compares the number of iterations required for minimum convergence.

Comparing Experiment 1 and Experiment 3 (with the same signal parameters), one can see that the acceptable frequency offset range is different. Revising (5.4),

$$\int_0^T (ae^{-2dt} + a_0 e^{-2d_0 t})dt - aa_0 \int_0^T e^{-(d+d_0)t} e^{-j\tilde{\omega}t} dt - aa_0 \int_0^T e^{-(d+d_0)t} e^{j\tilde{\omega}t} dt$$

Table 5.2: Comparison of offset range (Hz) and number of iterations

	Acceptable frequency offset range	Number of iterations for converging from ±25 Hz offset to a minimum
Cost function as Figure 5.5a	-4 ↔ 4	7 (Local minimum)
Cost function as Figure 5.5b	-26.5 ↔ 26.5	132 (Global minimum)
Cost function as Figure 5.5c	-27 ↔ 27	308 (Global minimum)
Varying cost function as proposed method	-27 ↔ 27	83 (Global minimum)

Table 5.3: Comparison of offset range (Hz) and number of iterations

	Acceptable frequency offset range	Number of iterations for converging from ±15 Hz offset to a minimum
Cost function as Figure 5.6a	-3.5 ↔ 3.5	5 (Local minimum)
Cost function as Figure 5.6b	-15.5 ↔ 15.5	104 (Global minimum)
Cost function as Figure 5.6c	-16 ↔ 16	216 (Global minimum)
Varying cost function as proposed method	-16 ↔ 16	67 (Global minimum)

if t is not sampled uniformly, we can not extended the range of integration from $(0, T)$ to $(-\infty, \infty)$ by just adding a window function to the original expression. Besides the window function, there must be another sampling function to represent the sampling pattern. Now (5.4) can be modified as

$$\int_0^T (ae^{-2dt} + a_0 e^{-2d_0 t})dt - 2aa_0 \Re\left\{\int_{-\infty}^{\infty} e^{-(d+d_0)t} u(t)p(t)[u(t) - u(t-T)]e^{-j\tilde{\omega}t}dt\right\} \quad (5.15)$$

where $p(t)$ is the nonuniform sampling pattern. The second term of (5.15) becomes the Fourier transform of $e^{-(d+d_0)t}u(t)p(t)[u(t)-u(t-T)]$, which is the convolution of $\mathcal{F}[e^{-(d+d_0)t}u(t)]$, $\mathcal{F}[u(t) - u(t-T)]$ and $\mathcal{F}[p(t)]$. Normally, increasing the decay values to avoid local minima has better performance in the uniformly sampled case than in the nonuniformly sampled case.

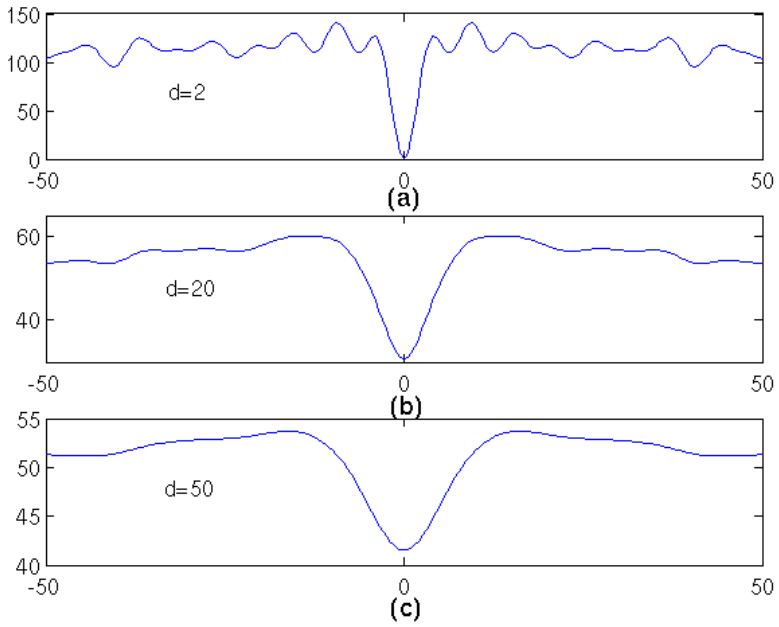

Figure 5.6: Cost function with estimated (a) decay=-2 (b) decay=-20 (c)decay=-50

From these experiments, one can see that enlarging the estimated decay value is an easy way to extend the acceptable frequency offset range within which the global minimum can be detected by gradient methods. However, when we keep increasing the decay values (in these experiments, from -20 to -50), the acceptable frequency offset ranges rarely change. In other words, if the estimated decay exceeds some values, enlarging decay will not further help in solving local minimum problems. In addition, a cost function with large estimated decays converges slowly (needs more iterations). Therefore, we need to select the estimated decays very carefully so that we can fully utilize the acceptable frequency offset range while keeping a relatively sharp gradient of the cost function.

5.3 Optimization Protocol with Weighted Scalars

Examing Figure 5.4, Figure 5.5 and Figure 5.6, we notice that when the estimated decays increase, the dynamic range of the cost function shrinks significantly. Especially

at the edge of the acceptable frequency offset range, the gradient of cost function is very small. In gradient-based method, if the gradient is very small, it will affect the optimization performance and speed [12, 26]. Moreover, when we use varying estimated decays to extend the acceptable frequency offset range, there is no easy way to decide what is the estimated decay value to start with: if the estimated decay is not big enough, we may not find the largest acceptable frequency offset range; but if the estimated decay is too big, it will sacrifice optimization speed and accurancy. Therefore, in this section, we introduce a new method: applying a sequence of weighted scalars to the signal, which could get the cost function having a better acceptable frequency offset range than the varying decay method, while avoiding these issues mentioned above.

5.3.1 Theory

Figure 5.7 shows a typical cost function. Normally, it is reasonable to assume that the cost function $C(\tilde{\omega})$ is symmetrical from $\tilde{\omega} = 0$, so here we focus on the positive side of the cost function. The solid waveform is the original shape of the cost function, the first gradient of $C(\tilde{\omega})$ in $(0, \tilde{\omega}_p)$ is always $C'(\tilde{\omega}) \geq 0$. Our goal is to change the shape of the cost function and let $C'(\tilde{\omega}) \geq 0$ in $(0, \tilde{\omega}_{p1})$ as dashed line shown.

In our case, the cost function is continuous, so is the gradient of the cost function. As shown in Figure 5.7, when the frequency offset $= \tilde{\omega}_p$, then $C'(\tilde{\omega}_p) = 0$. In order to extend the acceptable frequency offset range to $\tilde{\omega}_{p1}$, we need to make $C'(\tilde{\omega}_p) > 0$. In consequence, we utilize the following criterion:

$$min \sum_{0}^{\tilde{\omega}_p} \phi[C'(\tilde{\omega})] \tag{5.16}$$

where

$$\phi[C'(\tilde{\omega})] = \begin{cases} \frac{1}{C'(\tilde{\omega})+\Delta}, & \text{if } C'(\tilde{\omega}) \geq 0. \\ \frac{1}{\Delta} - C'(\tilde{\omega}), & \text{if } C'(\tilde{\omega}) < 0. \end{cases}$$

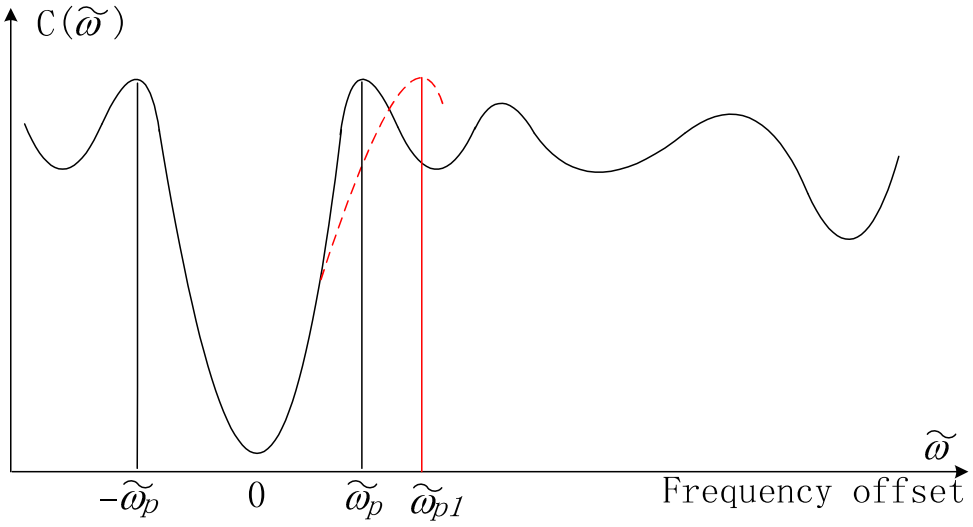

Figure 5.7: Typical cost function

and Δ is a very small positive number, which makes $C'(\tilde{\omega}) + \Delta$ not equal to zero. During each iteration step to minimize $\sum_0^{\tilde{\omega}_p} \phi[C'(\tilde{\omega})]$, we need to update the cost function $C(\tilde{\omega})$ and the first gradient of the cost function $C'(\tilde{\omega})$ with the varying weighted scalars.

$$\begin{aligned} C(\tilde{\omega}) &= \int_0^T W(t) \left| ae^{(-d+j\omega)t} - a_0 e^{(-d_0+j\omega_0)t} \right|^2 dt \\ &= \int_0^T W(t)(ae^{-2dt} + a_0 e^{-2d_0 t})dt - \int_0^T W(t) 2aa_0 e^{-(d+d_0)t} cos\tilde{\omega}t dt \qquad (5.17) \\ C'(\tilde{\omega}) &= \int_0^T W(t) 2aa_0 e^{-(d+d_0)t} t sin\tilde{\omega}t dt \qquad (5.18) \end{aligned}$$

Here $W(t)$ is a function defined by scalar weights that control the value of the function where the signal samples are observed. The following procedure is used to implement the proposed method:

1. Find first positive $\tilde{\omega} = \tilde{\omega}_p$, which makes $C'(\tilde{\omega}_p) = 0$. Hence, we can define the summation range of criterion (5.16).

2. Update the cost function and the first gradient of the cost function using (5.17) and (5.18) and the initial $W(t) = 1$.

3. Vary the values of $W(t)$ to minimize $\sum \phi[C'(\tilde{\omega})]$ in the range $(0, \tilde{\omega}_p)$, where $\tilde{\omega}_p$ is defined in step 1.

4. Repeat step 1, 2 and 3 until the new $\tilde{\omega}_p$ changes only slightly from the previous one.

5.3.2 Experiments and Results

In order to compare the performance between the weighted scalar method and varying decay method, three simulation experiments using the same orginal signal, are presented.

- Experiment 1: single resonant peak with uniform samples

$$x(t) = e^{(-1.3+j535\pi)t} \qquad t \in (0 : 0.18) \tag{5.19}$$

The observed $x(t)$ has 64 uniform samples. Exploring the frequency offsets from -50Hz to 50Hz, Figure 5.8 compares cost functions: without weighted scalars (upper plot), and with weighted scalars (bottom plot). Table 5.4 shows comparisons among the original cost function, the cost function applying varying decays and the cost function applying weighted scalars.

Table 5.4: Comparison of offset range (Hz) and number of iterations

	Acceptable frequency offset range	Number of iterations for converging from ±30 Hz offset to a minimum
Original cost function	-4 ↔ 4	7 (Local minimum)
Cost function applied varing decays	-45 ↔ 45	78 (Global minimum)
Cost function applied weighted scalars	-50 ↔ 50	42 (Global minimum)

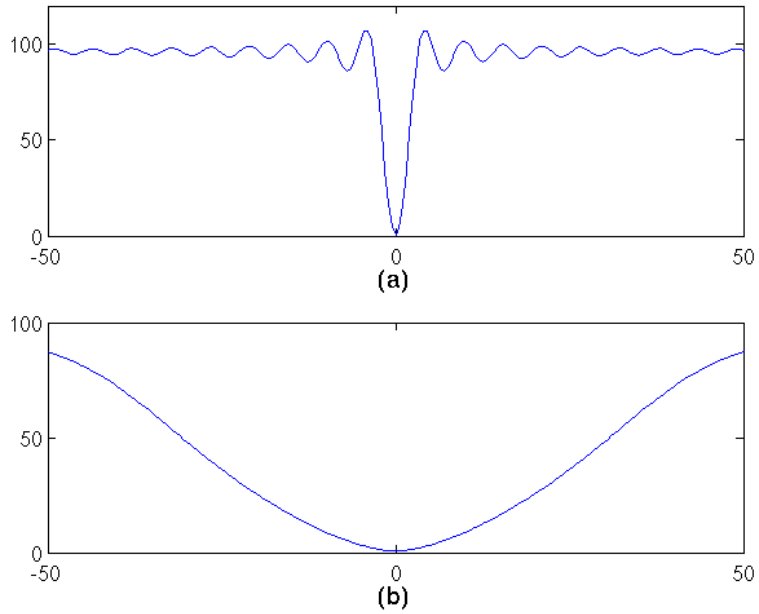

Figure 5.8: Cost function using estimated decay =-2 (a) without weighted scalars (b) with weighted scalars

- Experiment 2: two resonant peaks with uniform samples

$$x(t) = e^{(-1.3+j535\pi)t} + e^{(-3+j580\pi)t} \qquad t \in (0 : 0.18) \tag{5.20}$$

The observed $x(t)$ has 64 uniform samples. We explore the frequency offsets from -50Hz to 50Hz. Figure 5.9 compares the cost functions with or without weighted scalars. Table 5.5 shows the acceptable frequency offset ranges and the number of iterations required for different cost functions.

- Experiment 3: one resonant peak with nonuniform samples

$$x(t) = e^{(-1.3+j535\pi)t} \tag{5.21}$$

The observed signal is selected nonuniformly (64 samples) within $(0, 0.18)$. Figure 5.10 compares the cost functions with or without weighted scalars for the frequency offsets from

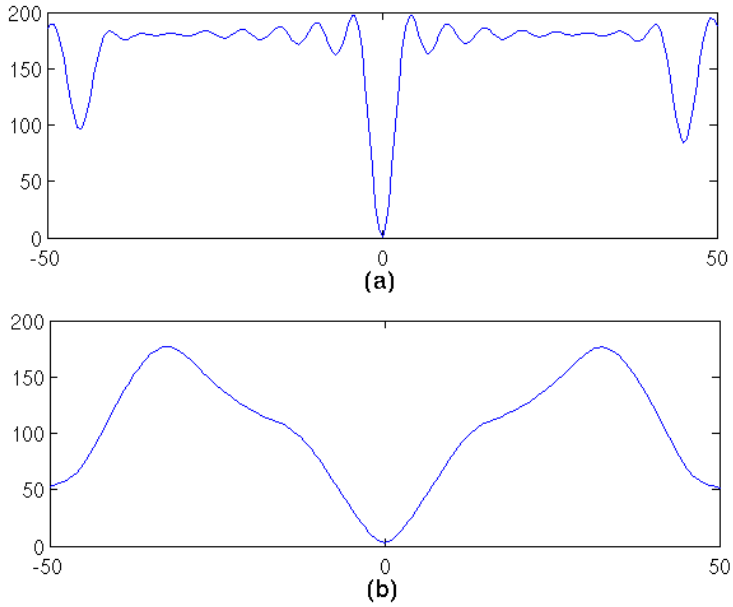

Figure 5.9: Cost function using estimated decay =-2 (a) without weighted function (b) with weighted function

-50Hz to 50Hz. Table 5.6 shows the acceptable frequency offset ranges and the number of iterations required for different cost functions.

5.4 Conclusion and Future Work

In this chapter, we introduced two methods to alleviate local minima effects. One is varying estimated decay during the reconstruction process; the other is optimizing a weighted function applied to the observed and estimated signal. Both methods intend to change the shape of the cost function and make the global minimum located in a wider main lobe.

Based on the above experiments, one can see that enlarging the estimated decay value is an easy way to extend the acceptable frequency offset range. However, since it will significantly decrease the gradient of the cost function, the reconstruction might be not accurate and is relatively slow. On the other hand, applying the weighted scalars to the

Table 5.5: Comparison of offset range (Hz) and number of iterations

	Acceptable frequency offset range	Number of iterations for converging from ±25 Hz offset to a minimum
Original cost function	-4 ↔ 4	7 (Local minimum)
Cost function applied varing decays	-27 ↔ 27	83 (Global minimum)
Cost function applied weighted scalars	-33 ↔ 33	37 (Global minimum)

Table 5.6: Comparison of offset range (Hz) and number of iterations

	Acceptable frequency offset range	Number of iterations for converging from ±15 Hz offset to a minimum
Original cost function	-3.5 ↔ 3.5	5(Local minimum)
Cost function applied varing decays	-16 ↔ 16	67 (Global minimum)
Cost function applied weighted scalars	-25 ↔ 25	26 (Global minimum)

signal can also extend the acceptable frequency offset range, while avoiding problems with reconstruction speed and accuracy.

In the reconstruction procedure, large global shifts due to field inhomogeneity must be compensated by a field map. Otherwise, spectral peaks may be initialized too far from the correct values, resulting in a failure to find these values due to local minima.

Future research will focus on making these methods are more robust to nonuniform measurements and accelerate the process of convergence.

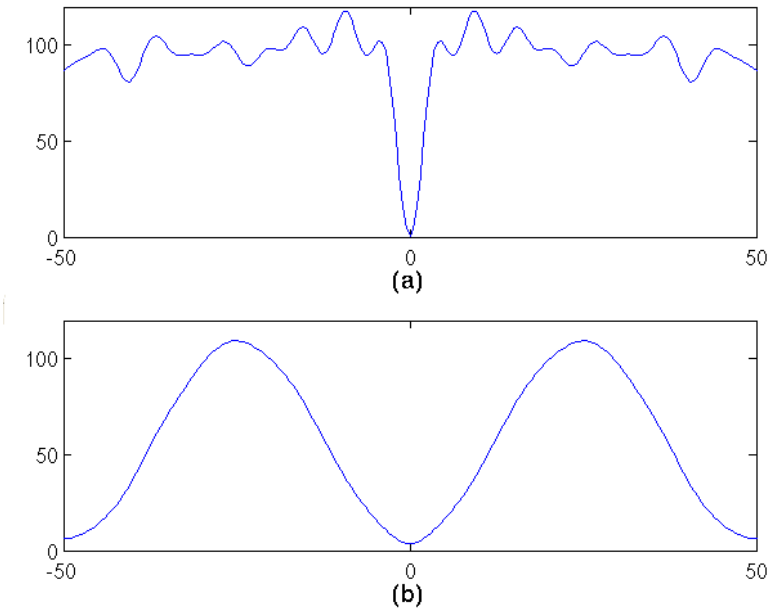

Figure 5.10: Cost function using estimated decay =-2 (a) without weighted function (b) with weighted function

Chapter 6

Conclusion

6.1 Summary of the Contributions of This Dissertation

In this dissertation, we studied several problems related to data acquisition and reconstruction in magnetic resonance spectroscopic imaging.

To accelerate the acquisition time, we first proposed an efficient acquisition scheme with echo-time selection. A criterion to estimate the mean square error in reconstruction was derived. Both single-echo SBS and multi-echo SBS were used to select a limited set of the most important echo-time values which were then applied to EPI acquisition. A lower-than-Nyquist density can be achieved with the proposed method. ^1H phantom experiments demonstrate that our approach achieves similar results to standard MRSI while only using 9.6% as much acquired data.

Due to the limitations of echo-time selection in data acquisition, two alternative data selection strategies were studied in Chapter 3. One is k-t selection, which extends the data selection in both k-space and time domains. Another one uses echo-time selection but with overlapped EPI, which can reduce the acquisition time for each k-space image. From the phantom experiment, we observe that k-t selection makes the selection process more accurate while requiring longer computation time to select the most informative data. In contrast, the selection process of echo-time selection using overlapped EPI can be done in seconds, but the reconstruction quality is not as good as k-t selection. Therefore, choosing which selection methods to use for acquisition depends on the application demands.

In Chapter 4, fast reconstruction methods for the nonlinear imaging model were investigated. We proposed to apply a polynomial approximation to the time exponential function

in the observed MRSI model and utilize a linear combination of FFTs to reduce the computational complexity in reconstruction. Simulation and phantom experiments show that this technique can largely accelerate the reconstruction process without sacrificing reconstruction accuracy.

The last part of this dissertation described two methods to alleviate frequency local minima effects. One is varying estimated decay during the reconstruction process, which can be easily implemented but does not achieve very good performance in reconstruction efficiency and accuracy. Another advanced technique we developed is optimizing a weighted function applied to the observed and estimated signal. The experimental results show that the weighted function method can efficiently attenuate frequency local minima effects, while avoiding the reconstruction speed and accuracy problems.

6.2 Future Works

For the acquisition part, the future research will focus on how to simplify the selection process in the k-t domain while still keeping the selection accuracy. Since our proposed methods are validated by simulation and phantom experiments, if it is possible, we also plan to apply our optimized selection strategies to in vivo experiments.

For the reconstruction part, we intend to develop a fast and more flexible reconstruction algorithm, which can accommodate more acquisition strategies and handle more parameter offsets.

Bibliography

[1] E. M. Haacke, R. W. Brown, and R. Venkatesan, *Magnetic Resonance Imaging: Physical Principles and Sequence Design*. Wiley-Liss, 1999.

[2] S. J. Nelson, D. B. Vigneron, and W. P. Dillon, "Serial evaluation of patients with brain tumors using volume MRI and 3D ^1H mrsi," *NMR in Biomedicine*, vol. 12, pp. 123–138, 1999.

[3] J. Kurhanewicz, D. Vigneron, and S. Nelson, "Three-dimensional magnetic resonance spectroscopic imaging of brain and prostate cancer," *Neoplasia*, vol. 2, pp. 166–189, 2000.

[4] N. Schuff, F. Ezekiel, and etc., "Region and tissue differences of metabolites in normally aged brain using multislice ^1H magnetic resonance spectroscopic imaging," *Magnetic Resonance in Medicine*, vol. 45, pp. 899–907, 2001.

[5] X. Wang, B. Wang, Z. Gao, J. Liu, and etc., "^1H-MRSI of prostate cancer: The relationship between metabolite ratio and tumor proliferation," *European Journal of Radiology*, vol. 73, no. 2, pp. 345 – 351, 2010.

[6] M. Fulham, A. Bizzi, M. Dietz, H. Shih, and etc., "Mapping of brain tumor metabolites with proton MR spectroscopic imaging: clinical relevance," *Radiology*, vol. 185, pp. 675–686, 1992.

[7] M. Jacobs, P. B. DPhil, and etc., "Proton magnetic resonance spectroscopic imaging of human breast cancer: A preliminary study," *Journal of Magnetic Resonance Imaging*, vol. 19, pp. 68–75, 2003.

[8] K. Zakian, K. Sircar, H. Hricak, and etc., "Correlation of proton MR spectroscopic imaging with gleason score based on step-section pathologic analysis after radical prostatectomy," *Radiology*, vol. 234, no. 3, pp. 804–814, 2005.

[9] S. Hu, M. Lustigc, A. Chen, and etc., "Compressed sensing for resolution enhancement of hyperpolarized ^{13}C flyback 3D-MRSI," *Journal of Magnetic Resonance*, vol. 192, pp. 258–264, 2008.

[10] S. J. Reeves and Z. Zhe, "Sequential algorithms for observation selection," *IEEE Transactions Signal Processing*, vol. 47, no. 1, pp. 123–132, 1999.

[11] R. Pohmann, M. von Kienlin, and A. Haase, "Theoretical evaluation and comparison of fast chemical shift imaging methods," *Journal of Magnetic Resonance*, vol. 129, pp. 145–160, 1997.

[12] E. K. P. Chong and S. H. Zak, *An Introduction to Optimization (Second Edition)*. Wiley-Interscience, 2001.

[13] J. Hugg, K. Laxer, G. Matson, A. Maudsley, and etc., "Lateralization of human focal epilepsy by 31P magnetic resonance spectroscopic imaging," *Neurology*, vol. 42, pp. 2011–2018, 1992.

[14] J. Hugg, G. Matson, D. Twieg, and etc., "Phosphorus-31 MR spectroscopic imaging (MRSI) of normal and pathological human brains," *Magnetic Resonance Imaging*, vol. 10, pp. 227–243, 1992.

[15] M. Swanson, D. Vigneron, and etc., "Proton HR-MAS spectroscopy and quantitative pathologic analysis of MRI/3D-MRSI-targeted postsurgical prostate tissues," *Magnetic Resonance in Medicine*, vol. 50, no. 5, pp. 944–954, 2003.

[16] D. Shaw, *Fourier Transform NMR Spectroscopy*. New York: Elsevier Scientific, 1971.

[17] Z. H. Cho, J. P. Jones, and M. Singh, *Foundations of Medical Imaging*. Wiley, 1993.

[18] F.-H. Lin, S.-Y. Tsai, R. Otazo, and etc., "Sensitivity-encoded (sense) proton echo-planar spectroscopic imaging (pepsi) in the human brain," *Magnetic Resonance in Medicine*, vol. 57, no. 2, pp. 249–257, 2007.

[19] A. Chen, C. Cunningham, and etc., "High-speed 3T MR spectroscopic imaging of prostate with flyback echo-planar encoding," *Magnetic Resonance Imaging*, vol. 25, pp. 1288–1292, 2007.

[20] Y. Gao and S. J. Reeves, "Optimal k-space sampling in MRSI for images with a limited region of support," *IEEE Transactions Medical Imaging*, vol. 19, no. 12, pp. 1168–1178, 2000.

[21] Y. Gao and S. J. Reeves, "Fast k-space sample selection in MRSI with a limited region of support," *IEEE Transactions Medical Imaging*, vol. 20, no. 9, pp. 868–876, 2001.

[22] S. K. Plevritis and A. Macovski, "MRS imaging using anatomically based k-space sampling and extrapolation," *Magnetic Resonance in Medicine*, vol. 34, pp. 686–693, 1995.

[23] S. Reeder, J. Brittain, T. Grist, and Y.-F. Yen, "Least-squares chemical shift separation for 13C metabolic imaging," *Journal of Magnetic Resonance Imaging*, vol. 26, no. 4, pp. 1145–1152, 2007.

[24] S. J. Orfanidis, *Introduction to Signal Processing*. Pearson Education, Inc, 2009.

[25] W. Tang, S. Reeves, and D. Twieg, "Fast joint estimation of local magnitude, decay, and frequency from single-shot mri," *Proceedings of SPIE*, vol. 6498, p. 649818, 2007.

[26] C.T.Kelley, *Iterative Methods for Optimization*. SIAM, 1999.